Development of Photocured Liquid-Crystalline Electrolytes with Ion-Transport Pathways and their Application to Electroactive Actuators

（イオン輸送パスを有する光硬化液晶電解質の開発と電気活性アクチュエータへの応用）

Che-Hao WU

Graduate School of Chemical Sciences and Engineering
Hokkaido University

September 2023

Development of Photocured Liquid-Crystalline Electrolytes with Ion-Transport Pathways and their Application to Electroactive Actuators

イオン輸送パスを有する光硬化液晶電解質の開発と電気活性アクチュエータへの応用

Che-Hao WU

Doctor of Philosophy in Science

Graduate School of Chemical Sciences and Engineering, Hokkaido University

Doctoral Supervisor: Dr. Masafumi YOSHIO, Professor

Abstract

The self-assembly of ionic molecules into hierarchically ordered structures is a promising route for the development of new solid electrolytes that enhance ion transport. This thesis focuses on presenting a series of ionic liquid-crystalline (LC) membrane electrolytes with commercial poly(3,4–ethylene dioxythiophene) polystyrene sulfonate (PEDOT:PSS) electrodes to create a novel class of ionic electroactive polymer (iEAP) actuators. Generally, iEAP actuators have the capability to produce bending deformation and deliver stable force output at low voltages (< 4 V), making them promising candidates for the next generation of soft robots and haptic sensors. However, conventional iEAP actuators, which rely on amorphous ion gels and hydrated ionic polymer films, suffer from limitations such as low force generation and poor durability during long-term actuation in the open air. These limitations mainly arise from the lack of mechanical robustness and electrolyte leakage. Therefore, the author's objective is to address these issues by utilizing the self-assembly of polymerizable LC molecules to design lightweight and robust LC polymer electrolytes specifically tailored for deformable actuators. The dimensionality of the ion diffusion pathways within the nanostructured electrolyte plays a crucial role in facilitating fast ion migration and reducing the energy barrier. With this in mind, the author conducts a comprehensive investigation into the relationship between LC nanostructures and actuation performance by exploring diverse designs of the LC molecules.

Chapter 1 provides a general introduction to iEAP actuators, including their working mechanism, the materials currently used in actuators, and the potential applications of ionic LC membranes.

Chapter 2 primarily focuses on an iEAP actuator based on the integration of ionic liquid (IL) into a one-dimensional (1D) ion-conductive free-standing LC polymer film. This film is formed through the columnar LC self-assembly and subsequent polymerization of polymerizable fan-shaped imidazolium LC molecules and ILs. The presence of inner ionophilic channels within this columnar LC structure enables fast ion migration compared to an amorphous structure. The correlation between the nanostructures and actuation performances is revealed through measurements of ionic conductivity as well as displacement and force of the actuators. The resulting columnar LC film actuator exhibits a bending strain of 0.2 % (at 2 V and 0.01 Hz) and generates a force of 0.3 mN, surpassing the performance of the corresponding amorphous film. This enhancement can be attributed to the efficient ion transport and the mechanical robustness of the ordered columnar structure. The concept of nanosegregation, characterized by the coexistence of liquid and anisotropic rigid domains, opens up a promising pathway for the design of electroactive actuators.

Achieving macroscopic alignment of the 1D ion-pathways that bridge between electrodes is a crucial technology for enhancing mass transport and electromechanical actuation. However, columnar LC materials often exhibit polydomain formation, posing a challenge to achieve vertical alignment of cylinders over large areas. In **Chapter 3**, the author presents a study on the self-assembly of a new environmentally benign biomolecular itaconate ionic amphiphile and a non-volatile IL, resulting in layer, bicontinuous cubic, and columnar LC structures. Through *in-situ* photopolymerization of these mixtures with a cross-linker, mechanically tough polymer electrolytes with layered ion transport pathways are obtained. The shear-aligned layered structure demonstrates enhanced ion transport and Young's modulus, making these robust ionic LC electrolytes suitable for application in soft actuators. The results indicate that the aligned layer electrolyte enhances the bending strain (0.29 % at 2 V, 0.1 Hz) and generation force (0.7 mN at 2 V, 0.1 Hz) of the actuators. Moreover, the photocured itaconate ionic amphiphile can be used to fabricate actuators with specific shape using printing technology. Finally,

the biodegradability of the itaconate LC polymer film has been confirmed through soil burial experiments. This materials design concept contributes to the development of sustainable soft electronics.

Moving beyond the construction of effective ion channels with 1D or 2D connectivity within the electrolytes, an intriguing design is to extend this concept to create alignment-free 3D ion transport pathways. In **Chapter 4**, the author introduces novel nanostructured polymer membrane electrolytes that contain 3D interconnected ion transport pathways. These lightweight and mechanically tough polymer films are obtained through a supramolecular columnar LC self-assembly of tapered ionic amphiphiles and a low content of IL (5.6 wt%), followed by photopolymerization. Leveraging the efficient and fast ion migration through the 3D ionic pathways in the solid matrix, nanostructured polymer actuators with flexible PEDOT:PSS electrodes exhibit excellent actuation performance (0.35 % at 2 V, 0.1 Hz) under low input voltages. The author demonstrates that this new type of actuator holds promise for applications in tactile sensor arrays, artificial muscles, and soft robots.

In order to further expand the design concept of 3D ionic pathways in electrolytes, the utilization of periodically ordered cubic structures proves to be an attractive option due to their interconnected ionic network and high viscoelastic characteristics. In **Chapter 5**, a micellar cubic electrolyte membrane with continuous ion pathways is introduced. This cubic electrolyte empowers the iEAP actuator to achieve both high bending strain (0.63 %) and high blocking force (2.7 mN) under low input voltage (2 V, 0.1 Hz). To construct this electrolyte membrane, the ionophilic domain within the inverse columnar structure, composed by wedge-shaped ionic LC molecules is further expanded to an inverse spherical symmetrical structure through the addition of an IL. The micellar cubic structure exhibits higher dynamic modulus, viscosity, and Young's modulus, both in its monomer state and as a polymer film. The author successfully demonstrates that the iEAP actuator based on the cubic LC membrane combines high-power output with large strain motion, enabling it to carry objects up to 40 times its own weight.

In **Chapter 6**, the author summarizes the benefit of using ionic LC electrolytes in iEAP actuators, discusses their overall performance, and explores future prospects for improving the reported materials and driving their real application. Through this

dissertation, the author highlights the significance of advancing LC membrane and molecular design to comprehend the mechanical properties and actuation behavior of the designed iEAP actuators. The innovative concept of combining photocured molecular design with nanoscale channels offers a new opportunity for significant advancements in the fields of soft electronics.

Keywords: *ionic electroactive actuator, photocured, ionic molecules, liquid-crystalline phases, ion-transport pathways.*

TABLE OF CONTENTS

Chapter 1 General Introduction..... 1

1.1 Electroactive Actuators in Soft Electronics. 2

1.2 Fundamental Introduction of Electroactive Polymer (EAP) Actuators. 3

1.3 The Common Design of Ionic EAP (iEAP) Actuators. 6

1.3.1 Electrode material effect and progress. 7

1.3.2 Nanostructured polymer electrolytes. 10

1.3.3 Evaluation of iEAP actuator performances. 12

1.4 Ionic Liquid Crystals. 12

1.4.1 Functional ionic liquid-crystalline membranes. 14

1.4.2 Self-assembly of ionic molecule in liquid-crystalline phase. 16

1.5 Objective and Outline of the Dissertation. 18

1.6 References. 20

Chapter 2 Low-Voltage-Driven Actuators Using Photo-Cross-Linked Ionic Columnar Liquid-Crystalline Polymer Films..... 23

2.1 Introduction. 24

2.2 Experimental Section. 27

2.2.1 Materials. 27

2.2.2 General methods. 27

2.2.3 Preparation of self-standing PEDOT:PSS films. 27

2.2.4 Preparation of photo-cross-linked polymer films and actuator. 28

2.2.5 Measurement of ionic conductivity. 29

2.2.6 Actuation performance test. 30

2.3 Results and Discussion. 31

2.3.1 Characteristic of ionic liquid-crystalline mixture. 31

2.3.2 Physicochemical and electrochemical analysis. 35

2.3.3 Bending actuation for ionic LC actuators. 36

2.3.4 Generation force from bending actuators. 39

2.4 Conclusions. 41

2.5 References. 42

Chapter 3 Liquid Crystal Self-Assembly of a Biomolecular Itaconate Ionic Amphiphile in an Ionic Liquid: Enhancement of Actuation by Uniformly Oriented Layered Ion Transport Pathways ***45***
3.1 Introduction. 46
3.2 Experimental Section. 49
3.2.1 Materials. 49
3.2.2 Synthesis of ionic molecule. 49
3.2.3 General methods. 49
3.2.4 Bio-degradation test. 49
3.2.5 Fabrication of liquid-crystalline actuators. 50
3.3 Results and Discussion. 51
3.3.1 Liquid crystal self-assembly of It and IL. 51
3.3.2 Ion-conductive properties of non-polymerized LC samples. 56
3.3.3 In-situ photopolymerization of the LC mixtures. 59
3.3.4 Characterization of ionic electroactive actuators with layered LC polymer electrolytes. 63
3.3.5 Combined the printable technology for preparation of ionic actuators. 66
3.3.6 Sustainable biodegradation of itaconic polymer film. 68
3.4 Conclusions. 70
3.5 References. 71

Chapter 4 Photocured Liquid-Crystalline Polymer Electrolytes with 3D Ion Transport Pathways for Electromechanical Actuators ***73***
4.1 Introduction. 74
4.2 Experimental Section. 77
4.2.1 Materials. 77
4.2.2 Synthesis of M–ILC and V–ILC. 77
4.2.3 Fabrication of P_V/IL(0) and P_{MV}/IL(x) actuators. 77
4.2.4 General methods. 78
4.2.5 Fabrication and observation of TEM samples. 78
4.2.6 Cyclic voltammetry measurements. 79
4.2.7 Ionic conductivity measurements. 79
4.2.8 Actuation performance test. 80

4.2.9 Preparation of artificial electronics devices and their operation. 80
4.3 Results and Discussion. 81
4.3.1 Liquid-crystalline and ion-conductive properties of ionic amphiphiles. 81
4.3.2 Liquid-crystalline and ion-conductive properties of ionic liquid-containing mixtures. 83
4.3.3 Characterization of columnar nanostructured polymer films. 87
4.3.4 Actuation performance of liquid-crystalline actuators. 91
4.3.5 Functional applications of liquid-crystalline actuators. 95
4.4 Conclusions. 96
4.5 References. 97

Chapter 5 Mechanically Tough Micellar Cubic Liquid-Crystalline Polymer Electrolytes for Electromechanical Actuators 99

5.1 Introduction. 100
5.2 Experimental Section. 103
5.2.1 Materials. 103
5.2.2 Synthesis of ionic amphiphilic (Vc12). 103
5.2.3 General methods. 103
5.2.4 Fabrication of liquid-crystalline actuators. 103
5.3 Results and Discussion. 105
5.3.1 Liquid-crystalline structure and ion conductive property. 105
5.3.2 Characterization of ion conductive liquid-crystalline polymer films. 110
5.3.3 Electroactive actuation for ionic liquid-crystalline actuators. 111
5.3.4 Generation force and mechanical characteristics of liquid-crystalline actuators. 113
5.4 Conclusions. 116
5.5 References. 117

Chapter 6 General Conclusion and Future Prospects 119

Appendix Synthesis and Identification Methods 125

7.1 General Procedures. 126
7.2 Synthesis of Ionic Molecule It. 126
7.3 Synthesis of Ionic Liquid Crystals M–ILC and V–ILC. 129

7.4 Synthesis of Ionic Liquid Crystal Vc12. 137

List of Publications ***141***

Acknowledgement ***142***

Chapter 1

General Introduction

1.1 Electroactive Actuators in Soft Electronics.

Human society, influenced by the rapid growth of the economic and technological industry, is now facing numerous unprecedented challenges. One intriguing issue is the replacement of traditional human labor with science technology or artificial intelligence (AI) in order to enhance work efficiency, reduce human error, and cut costs. For example, in 1785, the emergence of textile machinery opened the era of industrial weaving, and in 2000, the Da Vinci surgical system surpassed existing minimally invasive surgical techniques. The trend of machines replacing human labor has become indispensable in our future life. Although current technology has already brought us significant convenience, researchers are diligently working to further improve our living environment. The friendly and inspirational character, Baymax, from the science fiction anime “Big Hero 6” has attracted much interest in the development of soft electronic materials and related biomimetic devices. The soft, stretchable, and flexible electronic devices, with an appearance similar to human skin, have successfully sparked design ideas for next-generation soft robots. Therefore, actuators with the ability to convert response sources into mechanical motion are promising candidates for creating novel soft electronic and biomimetic robots.

To date, a variety of actuators that respond to different stimuli have been developed, such as ultraviolet light,[1] temperature,[2] magnetic,[3] humidity,[4] solvent,[5] voltage.[6] Actuators can change their shape or size when exposed to external stimuli, enabling them to exhibit locomotor behavior. Such deformable actuators that undergo volume expansion and material bending, have found successful applications in soft grippers,[6] active catheters,[7] and artificial iris[8] (**Figure 1.1**). Among the various types of actuators, the electroactive polymer (EAP) actuators made from commercial elastomers or polymers offer several advantages, such as large deformation, simple operation, controllable strain, and elasticity appearance. Consequently, they are recognized as potential tools for developing electronic skin and interactive human-machine interfaces (iHMI). Despite extensive research and use of EAP actuators in the preparation of the next-generation soft robots, critical challenges still remain in terms of designing principles that ensure safe operation, easy production, convenient use, material stability, and the incorporation of new materials into EAP actuators.

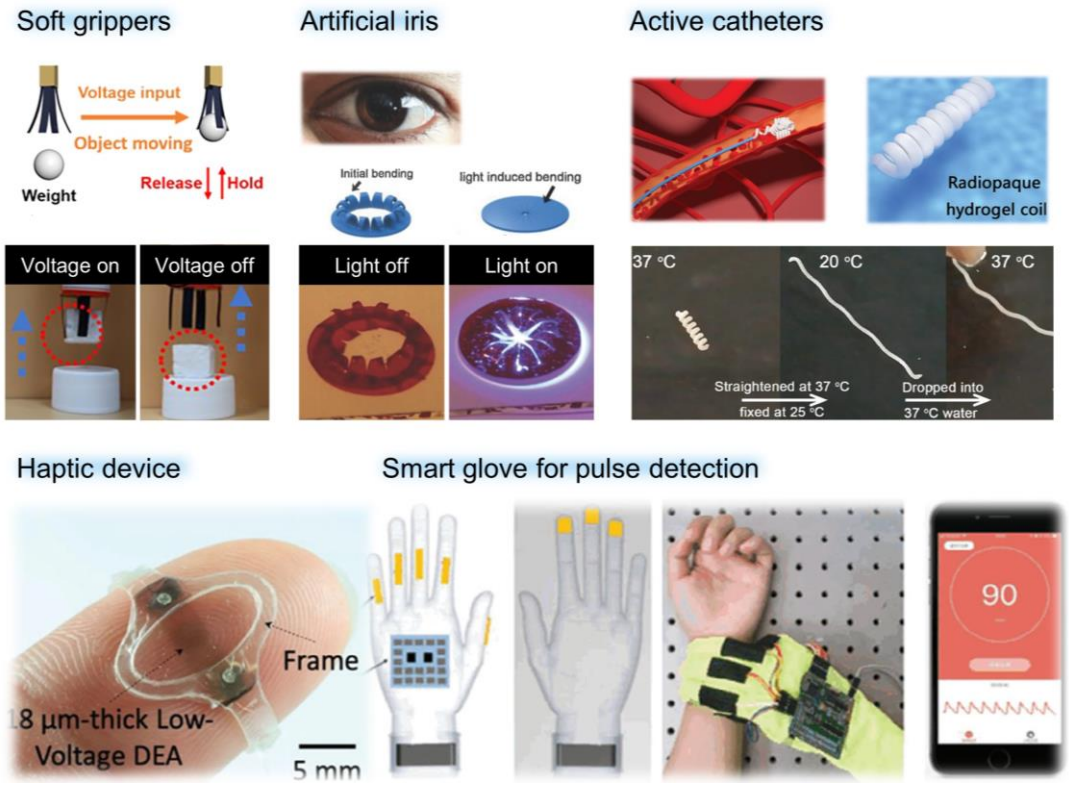

Figure 1.1 Functional applications of actuators.[6–10]

1.2 Fundamental Introduction of Electroactive Polymer (EAP) Actuators.

Electroactive polymer (EAP) actuators have the capability to change their original shape and volume when a voltage bias is applied. EAP is a general term used for polymers that exhibit electrically coupled responses. The early research on EAP actuators was pioneered by Roentgen and Sacerdote,[11] who discovered the responsive nature of dielectric polymers to electric fields. Since then, the benefits of these EAP actuators have been extensively studied, showcasing their potential in technology design. Scientists have noticed that these actuators not only induce deformation but also generate voltage at the material surface.[12,13] This unique ability has found wide applications in the development of soft robots, complex artificial systems or haptic sensors.[14]

EAP actuators are typically categorized into two main types: electronic EAP actuators and ionic EAP actuators.[11] In the case of electronic EAP actuator, deformation is primarily induced by Coulomb forces under applying electric fields. Examples of

electronic EAP actuators include dielectric elastomers, electrostrictive polymers, liquid-crystal elastomers, and piezoelectric polymers. These actuators are capable of changing their volume or shape when subjected to high electrical fields. On the other hand, ionic EAP actuators achieve material bending through the migration of dissociated cations and anions. This bending is mainly caused by the difference in volumes of mobile ions that accumulate on the opposite electrode surfaces. Well-known examples of ionic EAP actuators include ionic polymer metal composites (IPMCs), conductive polymers (CPs), ionic polymer gels (IPGs), and electrorheological fluids (ERFs).

One important advantage of the EAP actuators is their flexible, soft, and lightweight nature compared to inorganic actuators made from ceramics. This makes them more useful for practical application. The fundamental differences in working mechanisms between electronic EAP actuator and ionic EAP actuator result in their own benefit and drawbacks (**Table 1.1**).[15] The basic working mechanism of an electronic EAP actuator, such as the dielectric elastomer actuator, is a classic example of an electronic EAP actuator. The actuation was caused by the electrostatic force applied to the whole material (**Figure 1.2**). When a high electric field is applied to the surface electrode, the two electrodes are attracted to each other, causing the elastomer to be compressed by the electrostatic force (Maxwell stress). As a result, the specific surface area of the elastomer gradually increases with the thickness decreases. Once the electric field is switched off, the entire system can return to its original shape. This type of actuator can achieve the linear strain and rapid responses but requires high voltages.[11]

Table 1.1 Contrast list for Ionic EAP actuator and Electronic EAP actuator.[15]

Actuator	Advantage	Disadvantage
Ionic EAP	a. Produce large displacements. b. Require low voltages (less than 4V). c. Produce bi-directional actuation depended on the voltage polarity.	a. Generate slow responses. b. Induce a relatively low blocking force. c. Difficult to produce a consistent material. d. Need electrolytes and encapsulations. e. Low electromechanical coupling efficiency.
Electronic EAP	a. Operate in room conditions for a long time. b. Generate rapid responses. c. Hold strain under DC voltages. d. Induce relatively large blocking forces.	a. Require high voltages (150 MV/m). b. Require compromise between strain and stress. c. Produce monopolar actuation independent of voltage polarity.

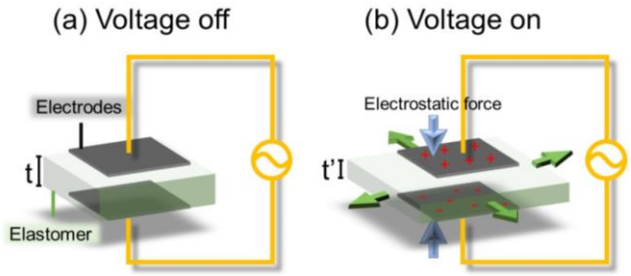

Figure 1.2 The working mechanism of electronic EAP actuator as one of the cases for dielectric elastomer actuator.

In the case of ionic EAP actuators, they are activated by the migration of free ions within the electrolyte. Ionic EAP actuators are comprised of a solid or quasi-solid polymer electrolyte sandwiched between a pair of electrodes, as shown in **Figure 1.3**. A commonly encountered solid polymer electrolyte is poly(ethylene glycol)–lithium salt complexes, which are stabilized by through ion-dipole interactions. Quasi-solid polymer electrolytes are composed of polymer matrices that incorporate diverse liquid electrolytes, such as ionic liquids, as well as aqueous or organic solutions of inorganic salts (*i.e.*, Li^+, K^+, Na^+, etc.) In the original state (voltage-off), the ions are randomly distributed throughout the electrolyte layer. When a voltage is applied to the actuator (voltage-on), the electrode layers become active, generating positive and negative electric charges on opposite surfaces. Simultaneously, the electric field triggers the dissociation of salts into cations and anions, which then migrate towards their respective electrode surfaces. The ions subsequently accumulate on the electrode surface, reaching a saturation state. Due to the variation in size and transference number between cation and anion, an imbalanced transport of ions occurs inside polymer matrices. This imbalance causes the electrolyte layer to undergo swelling and shrinking on opposite sides, leading to actuator bending.[11] This phenomenon can be explained by the principle of electric double-layer capacitance. However, depending on the electrode material, Faradaic redox reactions may occur instantaneously on the electrode surface, which can impact actuation. The redox process on the surface electrodes of an ionic EAP actuator can be determined through cyclic voltammetry measurement.

The driving voltage requirements on electronic EAP actuator and ionic EAP actuator differ significantly due to their distinct actuation mechanism. Indeed, the ionic EAP actuator driven by the dissociation ions can achieve remarkable actuation even with a low

supplied voltage. This is influenced by the ion content in polymer electrolytes. However, it should be noted that the use of ionic liquids or organic salts is limited to their specific electrochemical window, typically ranging between 4 V to –4 V. To ensure the safe operation and leverage knowledge of ionic material design, this thesis primarily focuses on the development of ionic EAP actuator by using our new designed ionic liquid crystals. The subsequent section will provide an overview of recent advancements in ionic EAP actuators, encompassing material design and new concepts.

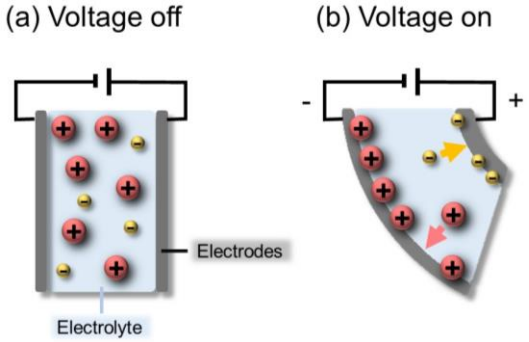

Figure 1.3 The working mechanism of ionic EAP actuator.

1.3 The Common Design of Ionic EAP (iEAP) Actuators.

The prototype of an ionic EAP (iEAP) actuator might be first proposed in the patent by Adolf team and Oguro team in around 1990.[16] They prepared the actuator from an ion exchange membrane sandwiched by a pair of electrodes. Meanwhile, they claimed the actuator not only responds by electric field but also subjected to solvent, temperature, or pH environments. The concept of such actuator was named electrically controlled polymeric gel actuators, in which the polymeric gel is mean the intermediate electrolyte layer. From the way of electrolyte layer, the earliest and most common use electrolyte, like Nafion (DuPont de Nemours, Inc.) or Flemion (AGC Inc.), that have the fluorine-contain polymer chain with pendant sulfonate groups (**Figure 1.4 (a)**). The hydrophilic sulfonate group was able to interact with water, ionic liquid, or hydrophilic ions (salts). After the membrane was formed, the preserved microscale of ionomeric channels can be accelerated the ion migration under electric fields (**Figure 1.4 (b)**). The commonly Nafion-based actuator has used the alkali metal cations (Li^+, Na^+, K^+) and water as the driving ions, resulting in the drawback on its durability for operation under an open-air environment. In order to improve the performances, researchers have successively

discovered that several commercial polymers (*i.e.*, poly(vinylidene fluoride–*co*–hexafluoropropylene), P(VdF–HFP); Thermoplastic Polyurethane, TPU; cellulose; polyimide; **Figure 1.4 (c)**) also exhibit good actuation after complexation with non-volatile ionic liquids. However, the presence of microstructure within the electrolyte layer was build up a vital concept for new actuator design in the future.

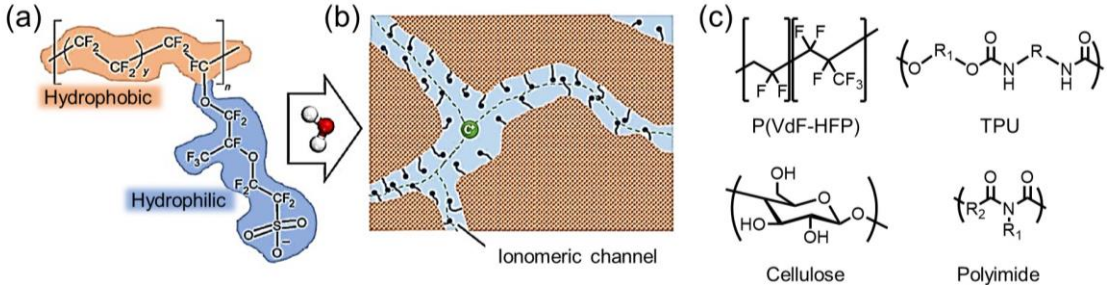

Figure 1.4 The iEAP actuators made from commercial polymers. (a) Molecular structure of Nafion.[17] (b) Microstructure of Nafion membrane containing ion channels. (c) Commonly used commercial polymers as the electrolyte layer in actuators.

1.3.1 Electrode material effect and progress.

The impact of electrode material in actuation performances acts as an important factor in iEAP actuators design. They dominate the ion movement and accumulation at the electrolyte/electrode interface. For example, the Nafion-based actuator was prepared as a kind of ionic polymer metal composites (IPMC) actuator in early-stage research. IPMC actuators are one of the most prominent categories of iEAP actuators. The common procedure for preparing such IPMC actuator was used electrochemical deposition or redox which allow forming the thin metallic conductive layer on the electrolyte surfaces (**Figure 1.5**).[18] This IPMC actuator has the advantage of a very high conductive electrode surface and well-attachment between electrode/electrolyte. However, the low durability of IPMC actuators caused by the evaporation of water or organic solvents inside is a common shortcoming that restricted their practical application.

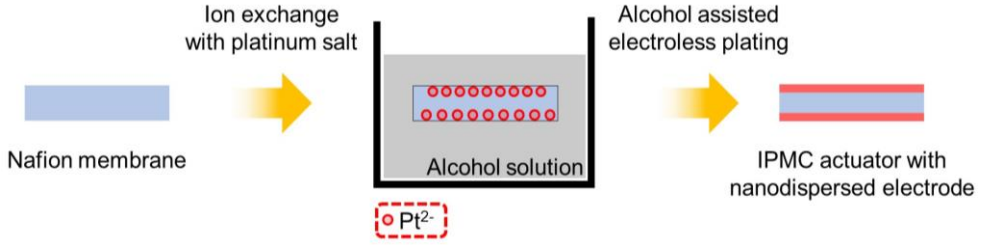

Figure 1.5 The preparation of metallic conductive electrode for IPMC actuators.[18]

Another commonly used commercial electrode, poly(3,4–ethylene dioxythiophene) doped with poly(styrene sulfonate) (**PEDOT:PSS**), was a polymer mixture that use to make high conductive and flexible polymer films. The **PEDOT:PSS** electrode was prepared by coating on the substrate, followed by evaporation of the residual solvent to obtain the conductive **PEDOT:PSS** layer. The ions doping/dedoping mechanism of **PEDOT: PSS**-based iEAP actuator is described follows: The mechanism can be divided into two cases (**Figure 1.6**). In the first case (Condition 1): the **PEDOT** is a conjugated polymer that carries positive charges, and **PSS** chain has the sulfonate group. The **PEDOT:PSS** presents the electroneutral under ambient conditions. When the voltage was applied to the **PEDOT:PSS**-based actuator, the **PEDOT** network was neutralized by electrons (reduced state). In this case, the macromolecule **PSS** unit was subsequential neutralized by dissociated cations and resulted in the expansion state. It is due to the large size of **PSS** that cannot migrate during the reduction. It called cation driven mechanism. In contrast, if the **PEDOT** doped with other small-size anions (*i.e.*, *p*–toluenesulfonic acid; PTSA), the anions were able to escape from the **PEDOT** network and neutralize with cations (Condition 2) when the voltage switch-on. It called anion driven mechanism.[19] The **PEDOT:PSS** electrode shows the advantage in simple fabrication, commercial availability, flexibility, and good conductivity. But the resistance in the electrode/electrolyte interface and the ordinary capacitance was the main challenge that need to overcome.

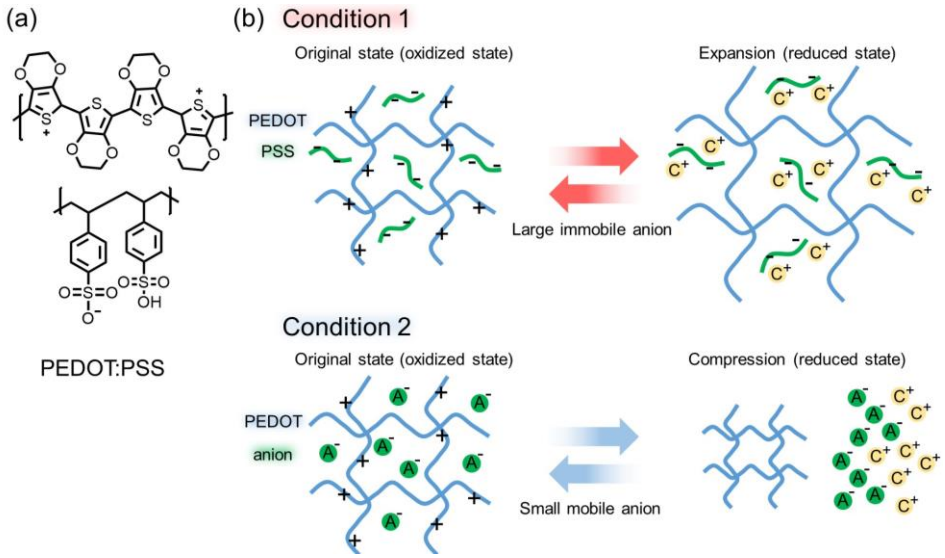

Figure 1.6 (a) The chemical structure of **PEDOT:PSS**. (b) The ionic actuation mechanism of **PEDOT:PSS**-based actuators.[19]

Based on the former discussion, good attachment between the electrode/electrolyte layers and large capacitance are the key factors to enhance the actuation performance. The electrode material would affect the kinetic diffusions and excessive storage for mobile ion within the electrolyte, owing on its tunable electrostatic forces and fast interfacial redox reactions. Therefore, significant recent efforts have focused on the architected electrodes embedding into new type of iEAP actuators. Recently, two-dimensional (2D) inorganic materials (*i.e.*, Graphene, Graphdiyne, Carbon nitride, MXene, Black phosphorous, Molybdenum disulfide…et al.) have been found to encompass the benefit of high interfacial transfer, fast ion diffusion, ion flooding intercalation, and high electron conduction (**Figure 1.7 (a)**). The design concept of the architected electrode has created the stereoscopic structure within the materials which could allow the insertion of ions into the electrode layer and guides larger volume expansion. For example, Oh *et al.* report the sulfur and nitrogen co-doped graphene/**PEDOT:PSS** hybrid electrode to enhance the electrochemical activities with electrolyte.[20] The newly designed composite electrode material contains highly porous, electrical conductive, and electric double-layer capacitive (EDLC) characteristics of dominantly affect and improve the ion redistribution response of the ionic liquids in the polymer electrolyte. It can efficiently enhance ion dissociation and aggregation in the electrode surface. The similar idea of such architected electrodes consisting of 1D to 3D heterogeneous surface structure impart to the function of large specific surface area, ordered microstructure, and controllable electrochemical activity that was able to efficiently decrease the interface resistance of electrode/electrolyte and improve specific capacitance (**Figure 1.7 (b)**).

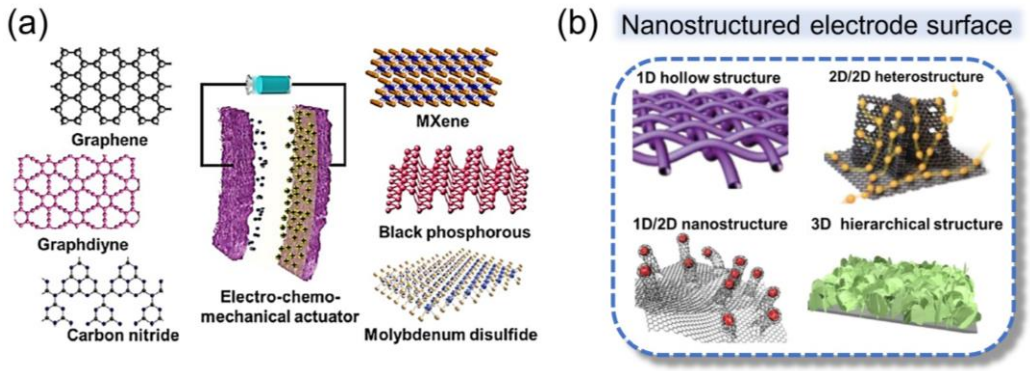

Figure 1.7 (a) The example of several types of nanostructured electrode materials. (b) Architected electrodes with 1D to 3D heterogeneous surface structure.[21]

1.3.2 Nanostructured polymer electrolytes.

The micro-channels within Nafion electrolyte was believed to enhance ion diffusion. This idea has encouraged the emergence of nanostructured electrolytes for the development of high-performance iEAP actuators. The important design concept of a nanostructured electrolyte was focused on the two aspects: (1) creation of interconnected ion-conduction domains, and (2) arrangement of ordered ionic channels. For example, Oh *et al.* reported a porous P(VdF–*co*–HFP) electrolyte-based actuator (**Figure 1.8 (a)**).[22] This micro-structured electrolyte was prepared from coating methods, followed by evaporation of incompatible solvent to leave the micro-sized porous structure. Then, the micro-sized porous polymer membrane was doped with ionic liquid, and covered with two pieces of **PEDOT:PSS** electrodes to afford actuators. In the actuation performance, the polymer actuator containing micro-sized porous structure exhibits better performance than the comparison non-porous electrolyte-based actuator. This enhancement of actuation was mainly due to the formation of continuous ion-conductive domains and the enhancement of ionic density for efficient ion migration.

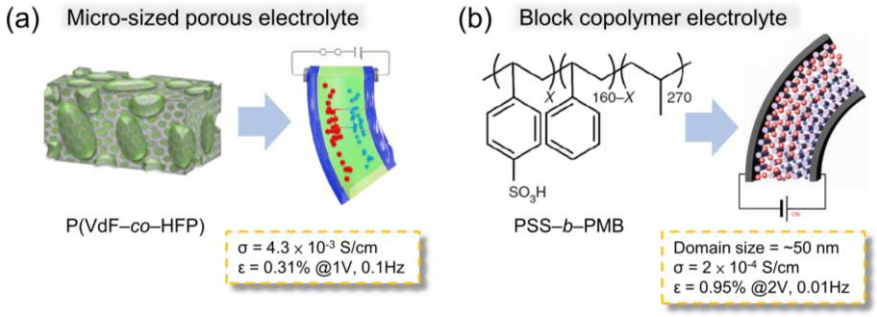

Figure 1.8 The example of iEAP actuators with (a) micro-sized porous electrolyte made from commercial P(VdF–*co*–HFP),[22] and (b) the PSS–*b*–PMB polymer electrolyte that present hexagonal-cylindrical (HEX) structure.[23]

On the other hand, the ordered arrangement of the nanostructure can be realized by using self-assembled block copolymers (BCPs) electrolyte. For example, Park *et al.* reported a fast-responded BCP gel actuator (**Figure 1.8 (b)**).[23] The self-assembly of poly (styrene sulfonate–*b*–methyl butylene) (PSS–*b*–PMB) polymer with ionic liquid exhibits hexagonal-cylindrical (HEX) arrangement due to the immiscibility between the ionic PSS and non-ionic PMB phases. This actuator has high ordering HEX structure and continuous

ion channels for efficient ion transport. Such actuator demonstrates high ionic conductivity, good actuation, and fast-response property.

Despite the BCP-based actuators having good performance, the design of a well-defined BCPs still suffered from the limitations arising from the complex thermodynamically self-assemble behaviors. The self-assembly of BCPs through microscale of phase separation to form diverse morphologies that are determined by three parameters: the degree of polymerization (N), the Flory-Huggins interaction parameter of two blocks (χ), and the volume fraction of blocks (f_A) (**Figure 1.9 (a)**). Based on the SCFT calculated phase diagram, the self-assembly of the BCP is directly related to χN value, where the χ was determined by the collocation of the monomer pair. The minimum segregation force (χN) for ordered equilibrium structures formed is 10.5. At the same χN value, the changing of fraction ratio can form the symmetric structure, but with an inverted arrangement. Therefore, the formation of phase-separated nanostructure would be precisely controlled by these three parameters. Furthermore, to obtain small-scale and high-density microphase-separated domains (< 10 nm), it will be another emphasis to develop BCPs with high χ value but low N (**Figure 1.9 (b)**). Although now has some paradigm to prepare high χ BCPs (*i.e.*, polyethylene-based sodium sulfosuccinate multiblock copolymer),[24] there is still a lack of records in the application of iEAP actuators based on ionic high χ BCPs.

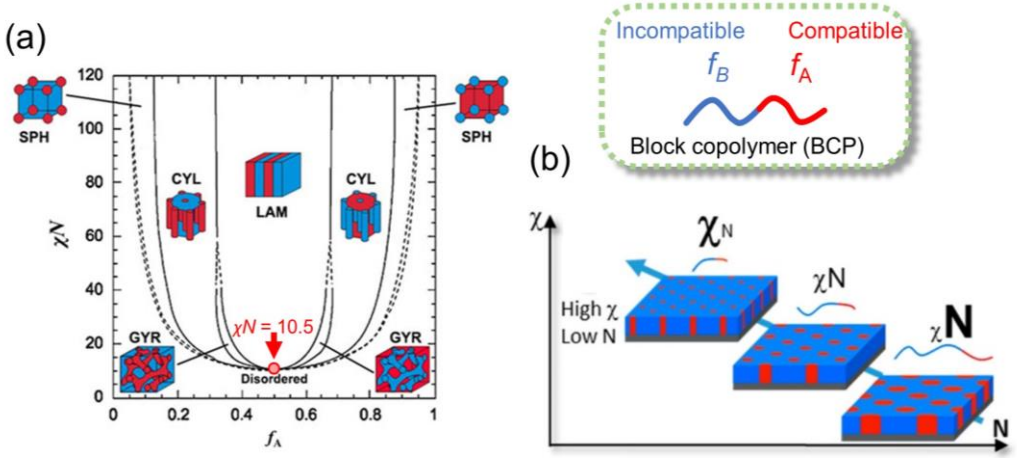

Figure 1.9 (a) Block copolymer phase diagram was calculated using the self-consistent mean-field theory (SCFT). Symbol of nanostructure: SPH (spheres), CYL (cylinders), LAM (lamellae) and GYR (gyroid). (b) The challenge of designing a high χ block copolymer with low molecular weight.[25]

1.3.3 Evaluation of iEAP actuator performances.

The iEAP actuator was able to respond under electric fields and shows symmetric bending oscillation. The bending displacement of actuator was quite related to its free length and thickness. To better evaluate the actuation performances from each distinct actuators, the research papers normally used the curvature and bending strain to compare them (**Figure 1.10**). The increased free length of actuators can induce the large displacement under the same condition. However, the displacement of actuators decreased as the thickness increases, but the bending strain increases. The blocking force generated from bending actuators can be estimated by the following equation: $P \propto \frac{3\delta EI}{L^3}$, where P is theoretical force, δ is displacement, E is modulus of elasticity, I is moment of inertia, and L is free length of actuator.[26] Therefore, the free length, displacement, and thickness would also affect the generation force. The tailored design of a comprehensive actuator with large bending strain and generated force has requires the consideration of not only material design but also the dimensional of actuator.

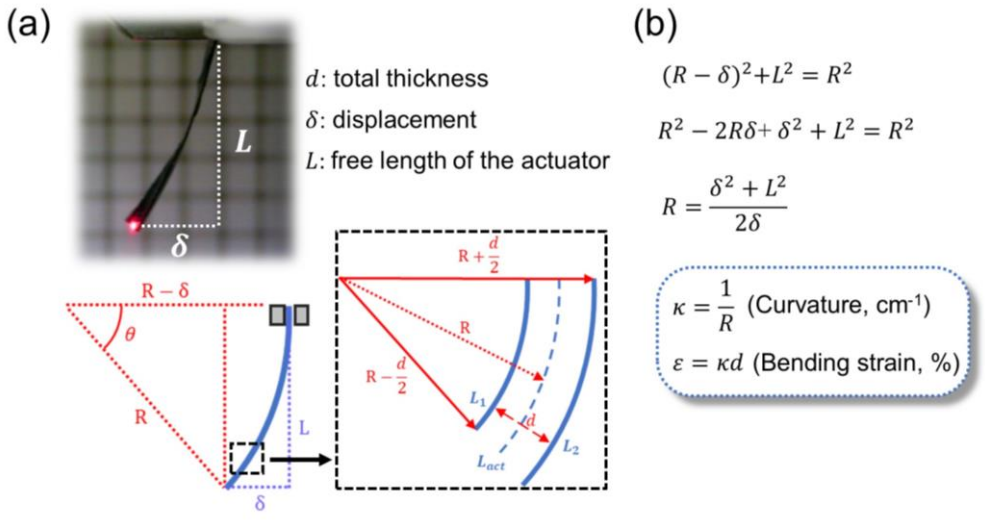

Figure 1.10 (a) Evaluation of the bending actuator. (b) The formula and relationship of bending strain and curvature.

1.4 Ionic Liquid Crystals.

Ionic liquid crystals (ILCs), consisting of the mesogenic domain and ionic group, were able to self-organization into liquid-crystalline mesophase, which show the combined characteristics of liquid crystals (anisotropy of physical properties) and ionic

liquid (ion conduction). The first example of a prototype ILC was the *N*–(n–alkyl) pyridinium chlorides reported by Knight and Shaw in 1938.[27] They have introduced an ionophobic alkyl chain into the pyridinium unit to form the liquid-crystalline phase. Due to the immiscibility between the ionic part and the alkyl chain, this ionic molecule leads to the formation of dimensionally ordered states. So far, several shape of ILCs structure have been proposed, including fan-shaped, disc-like, rod-shaped, gemini-types, simple ionic molecules, dendrimers…et al (**Figure 1.11 (a)**).[28] However, the selection of appropriate ionic moiety, molecular shape, functional groups, and ionic liquid were the essential factors to control the liquid-crystalline morphologies (**Figure 1.11 (b)**).[29] The self-organization of ILCs and ionic liquid allows forming the nanostructure with smectic (Sm), bicontinuous cubic (Cub_{bi}), hexagonal columnar (Col_h), and micellar cubic (Cub_M) symmetric, which exhibit the similar morphologies of the self-assembled BCPs (**Figure 1.11 (c)**).

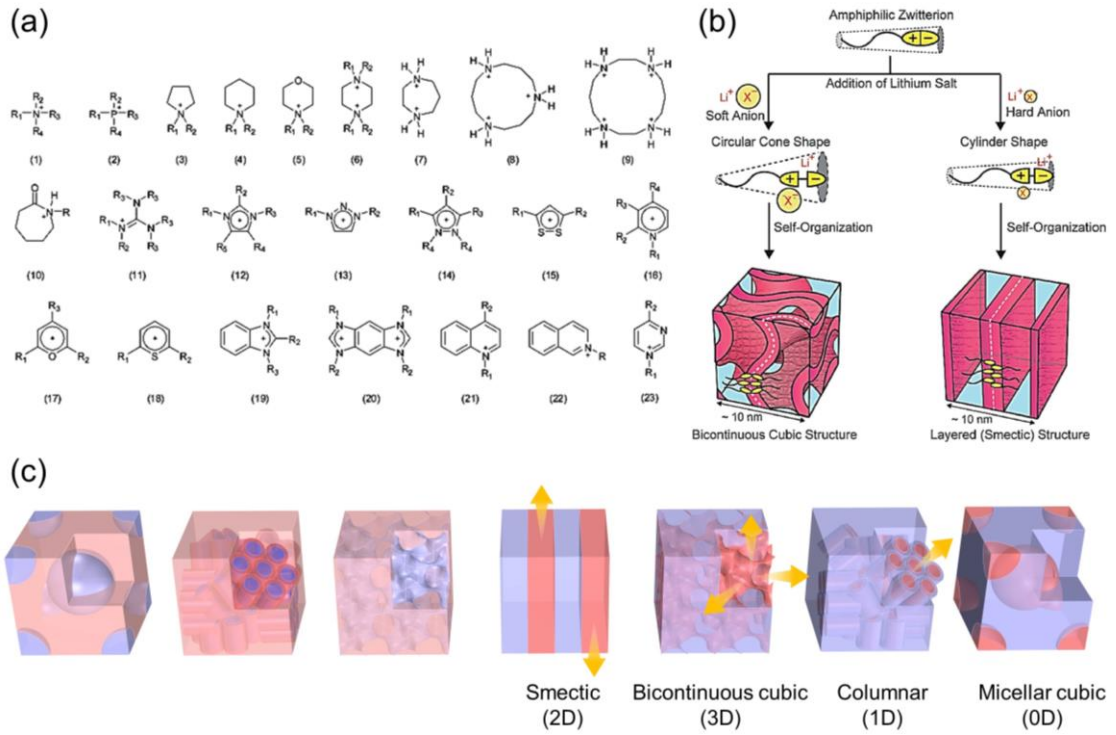

Figure 1.11 (a) Example of the general molecular structure of the organic cations based ionic liquid crystals.[28] (b) Schematic illustration that the selection of different lithium salts can induce the Cub_{bi} and Sm phases, respectively.[29] (c) Nano-segregation structure of ILCs (complexation with ionic liquid). The red part means ion conductive region. The blue part means the insulating region. The arrow means the direction of ion transport.

According to the induction media of the phase transition, ILCs are typically divided into two categories: thermotropic ILCs and lyotropic ILCs. The former was mainly controlled by the temperature to induce the liquid-crystalline structure transformation. The latter needs additional of organic solvent to guide the liquid-crystalline phase formed. The ion conductive liquid-crystalline nanostructure was formed by the phase-separated ionic section and insulated section, in which the ionic fraction in the liquid-crystalline domains have the partially connected or interconnected ion transport pathways (defined as 1D to 3D ion pathways, **Figure 1.11 (c)**). Thus far, these ionic channels have been found to efficiently enhance ion migration or matter diffusion/rejection and engaged in widespread applications of fuel cells, water treatment, electro-optical devices, or molecular sensing systems.

1.4.1 Functional ionic liquid-crystalline membranes.

ILCs containing the photo-polymerizable groups were able to form mechanically tough liquid-crystalline membranes by exposing ultraviolet (UV) light. Meanwhile, the nanoscale of ion-active channels can be retained in the membrane. Such nanostructured liquid-crystalline membranes have the potential to expand the application fields more than low molecular weight ILCs without polymerizable group. For example, Ichikawa *et al.* report a Cub_{bi} membrane prepared from a thermotropic ionic LC molecule (**Figure 1.12 (a)**).[30] A fan-shaped ILC consists of the mesogen admitted with two polymerizable 1,3–diene groups and an ammonium moiety. By complexation of $LiBF_4$ salt, the monomer mixture exhibits the Cub_{bi} and Col_h phases between -6 to 19 ºC and 19 to 56 ºC, respectively. After photopolymerization, the Cub_{bi} membrane show 36 times higher ionic conductivity than Col_h membrane. This is because Cub_{bi} phases possess 3D interconnected ionic porous that do not require additional macroscopic alignment technology for good ion transport. On the other case, Kato *et al.* report a nanostructured water-treatment membrane which was made from the self-assembly of gemini thermotropic smectic ILCs (**Figure 1.12 (b)**).[31] The layered structure of gemini-type ILCs may suppress the formation of pinholes due to the structural change during photopolymerization, resulting in the stable virus removal and higher water flux than Cub_{bi} and Col_h membranes.

The basically physicochemical properties of polymerizable ILCs and non-polymerizable ILCs are different. The rational design of a new photo-polymerizable ILC structure needs to consider the self-assembly driving force derived from ionic moieties and alkyl chain lengths in the molecular structure. The introduction of a polarity polymerizable group in the molecular tail (*i.e.*, alkyl chain end) might disturb the thermodynamic equilibrium of the liquid-crystalline phase, thereby affecting the molecules packing and arrangement as well as the formation of liquid-crystalline phase. Although liquid-crystalline membranes act as a novel and potential tool in various applications, the molecular structure design of polymerizable ILCs involving the formation of liquid-crystalline phase still heavily relied on empirical structures from the previous research.

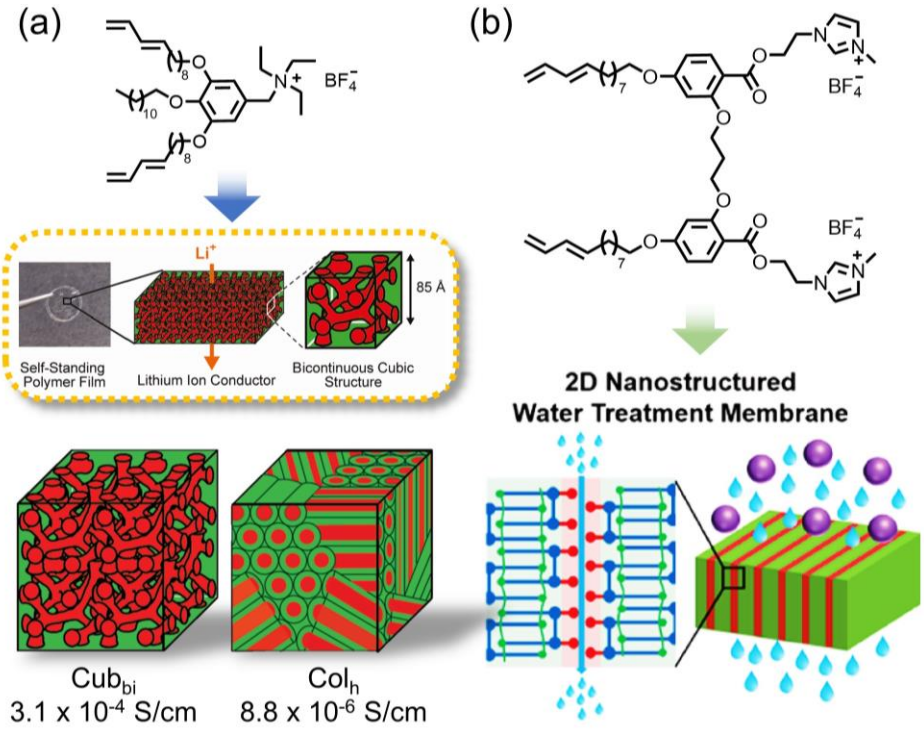

Figure 1.12 (a) The freestanding ion-conductive liquid-crystalline membrane has 3D interconnected Cub_{bi} structure formed by a fan-shaped polymerizable ILC with $LiBF_4$ salt. The Cub_{bi} and Col_h films show the ionic conductivity of 3.1×10^{-4} S/cm and 8.8×10^{-6} S/cm at 90 °C, respectively.[30] (b) The gemini-type polymerizable ILC was applied in a high virus removal and water permeation membrane.[31]

1.4.2 *Self-assembly of ionic molecule in liquid-crystalline phase.*

The liquid-crystalline phase formed by simple ionic molecules have received the attention in the few decades. Perhaps it is due to the successful employed cases of ILCs and related materials, the self-assembly behavior and their application based on ionic molecules has gradually aroused the keen interest of scientists. From the way of molecular structure, the ionic molecules, consisting of an ionic part with a simple alkyl chain but no mesogen unit, was similar to the surfactants that include both polar domain and non-polar domain. Thus, ionic molecules exhibit lyotropic liquid-crystalline behavior in most cases but still have a few examples that reported thermotropic ionic molecules.[32] Such self-assembly of ionic molecules normally demonstrates the diverse liquid-crystalline phases owing to the flexibility of the molecular chain that was easily rearranged by lyotropic solvent. The photo-polymerization of the polymerizable group-containing ionic molecule in the liquid-crystalline phase was a common strategy to obtain nanostructured liquid-crystalline film. Such films have the advantage of simple synthesis and preparation, low cost, and the easy formation of sub-1-nm porous structure,[33] which is more competitive than traditional ILC films. Recently, there have been reported a few successful cases in the preparation of liquid-crystalline films with 3D ionic pathways (*i.e.*, Cub_{bi}, or Col_h with a lipophilic cylinder surrounded by ionic shells.[34]) by using polymerizable ionic molecules.

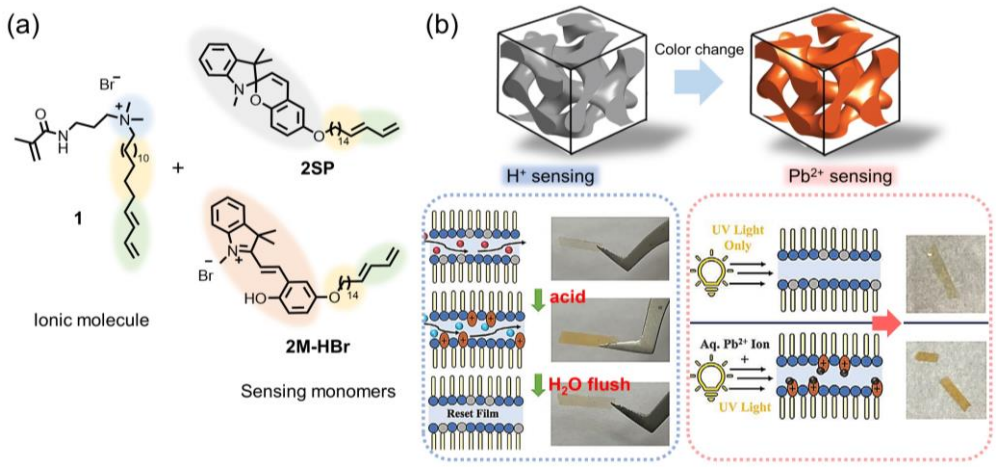

Figure 1.13 (a) The molecular structures of the cationic molecule (**1**), spiropyran-based sensing monomers (**2SP**), and its protonated-merocyanine form (**2M-HBr**). (b) The lyotropic Cub_{bi} film exhibits spiropyran acidochromism and UV-light-mediated Pb^{2+} ion uptake properties.[35]

For example, Gin *et al.* reported a first example of a functionalized periodic Cub_{bi} membrane for ion recognition.[35] The embedded of spiropyran-based sensing monomers into Cub_{bi} structure that composed of the self-assembled ionic molecules with tiny water, subsequent irradiated UV light can obtain a solid-state sensing material for gated transport and response to external stimuli (**Figure 1.13**). The Cub_{bi} membrane exhibits remarkable acidochromism by exposing acidic water/vapor, and also can act as an effective trap for capturing Pb^{2+} ions (**Figure 1.13 (b)**). This sensing Cub_{bi} membrane might demonstrate the erasing-writing property that would open up a new route in the application of colorimetric sorbent, gated response materials, or anti-counterfeiting materials.

The ionic molecules have similar properties to ILCs but offer a potential way to simplify the preparation procedure. Thus far, although most cases of lyotropic ionic molecule-based liquid-crystalline films show the potential benefit in the filter membranes, they were limited in use for only the water-existing conditions. In order to explore the professional operation fields including ionic battery and energy storage devices, the development of thermotropic ionic molecule-based liquid-crystalline film is necessary to satisfy the present requirement, which would favor push down toward scientific progress in the future.

1.5 Objective and Outline of the Dissertation.

The primary concept for this study is to construct a new iEAP actuator by using photo-crosslinked ionic liquid-crystalline (LC) membranes and to investigate the morphological effect of the ionic domain on its performance. Previous research has highlighted the significance of nanostructured electrolytes in facilitating efficient ion transport, which is crucial for achieving high-performance iEAP actuators. However, whether it is BCPs, covalent organic frameworks (COFs), or porous polymeric membranes, they all share common limitations such as low generation force and the need for a significant amount of ionic liquids, rendering them inadequate for current requirements of safety and high-power generation actuators in practical applications. To address these challenges, I propose a strategy that involves using a photo-crosslinked LC membrane as the electrolyte layer inside the iEAP actuator, anticipating that this approach will offer synergistic benefits of both the photo-crosslinked network and the nano-segregation ionic LC phase. By leveraging these advantages, it is possible to create nanoscale-ordered ionic pathways and enhance the mechanical toughness of the actuator simultaneously. This concept aims to overcome the existing limitations faced by traditional iEAP actuators. This dissertation aims to establish a comprehensive understanding of the relationship between LC morphologies and the performance of iEAP actuators. It covers a wide range of disciplines, including the design of ionic liquid crystals, synthesis methods, analytical techniques for the self-assembly of ionic liquid crystals, estimation of material properties, and their application in iEAP actuators.

The doctoral dissertation consists of 6 *Chapters* and an *Appendix* that focuses on the customized design of specific ion-active channels formed by polymerizable LC monomers and the evaluation of their performance employed in iEAP actuators. ***Chapter 1*** introduces the fundamental principles and advantages of EAP actuators, the working mechanism underlying their operation, the overall design concept, as well as the drawbacks found in the current adoption of iEAP materials. The subsequent chapter demonstrate the benefit of utilizing ionic liquid crystals and ionic monomer materials, and explore how to leverage the ionic pathways within LC membranes to create innovative functional applications. ***Chapter 2*** demonstrates that an LC membrane formed by the fan-shaped polymerizable LC monomers, in which the membrane contains the 1D

ionic channels inside the columnar structures. The result support that the creation of ionic columnar structure has a positive impact on enhancing the performance of iEAP actuators compared to the corresponding amorphous LC membrane. ***Chapter 3*** focuses on the discussion of diverse LC phase transformations managed by the biomolecular itaconate ionic amphiphile with an ionic liquid, and subsequential polymerization inducing the formation of the 2D ionic layered structures. I illustrate that the ordered arrangement of ion-active layer is important for ion transport in iEAP actuators. In ***Chapter 4***, I present a new design for fan-shaped LC monomers that can be self-organized into an inverted columnar structure, while the ionic part of each column interconnected to form a 3D ionic pathway. This chapter illustrates the potential performance of an almost alignment-free columnar structure to create a new type of iEAP actuators. In ***Chapter 5***, I further extend the concept of inverted polar domains in LC morphology to the design of periodic micellar cubic structures. By exploiting the benefit of periodic spherical structure with low tortuosity of ion conductive domains and high viscoelasticity behavior, I obtain an iEAP actuator that simultaneously achieves high bending strain and high blocking force under a low input voltage. Finally, in ***Chapter 6***, major findings and further prospects of this study are highlighted. And the overall synthesis and identification method are given in ***Appendix***.

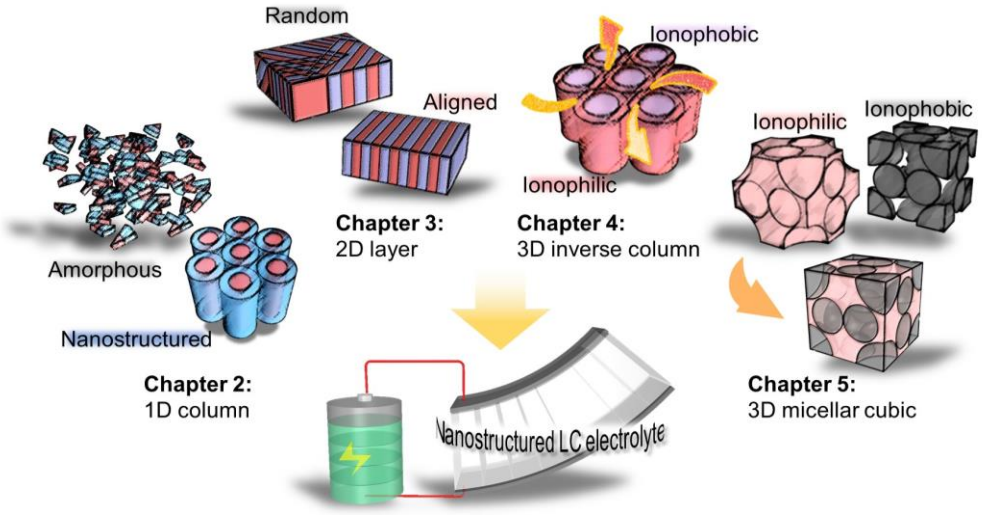

Figure 1.14 Schematic illustration of the design concept for the construction of novel iEAP actuators by using nanostructured LC polymer membranes containing different types of ion pathways. (The red part is ionic domains.)

1.6 References.

(1) Li, C.; Iscen, A.; Palmer, L. C.; Schatz, G. C.; Stupp S. I. Light-Driven Expansion of Spiropyran Hydrogels. *J. Am. Chem. Soc.* **2020**, *142*, 8447–8453.

(2) Huang, Y. C.; Cheng, Q. P., Jeng, U-. S.; Hsu, S-. H. A Biomimetic Bilayer Hydrogel Actuator Based on Thermoresponsive Gelatin Methacryloyl-Poly(N-isopropylacrylamide) Hydrogel with Three-Dimensional Printability. *ACS Appl. Mater. Interfaces* **2023**, *15*, 5798–5810.

(3) Kim, J.; Chung, S. E.; Choi, S-. E.; Lee, H.; Kim, J.; Kwon, S. Programming Magnetic Anisotropy in Polymeric Microactuators. *Nature Materials* **2011**, *10*, 747–752.

(4) Haan, L. T. d.; Verjans, J. M. N.; Broer, D. J.; Bastiaansen, C. W. M.; Schenning, A. P. H. J. Humidity-Responsive Liquid Crystalline Polymer Actuators with an Asymmetry in the Molecular Trigger That Bend, Fold, and Curl. *J. Am. Chem. Soc.* **2014**, *136*, 10585–10588.

(5) Sun, J-. K.; Zhang, W.; Guterman, R.; Lin, H-. J.; Yuan, J. Porous Polycarbene-Bearing Membrane Actuator for Ultrasensitive Weak-Acid Detection and Real-time Chemical Reaction Monitoring. *Nature Comm.* **2018**, *9*, 1717.

(6) Liu, L.; Wang, C.; Wu, Z.; Xing, Y. Ultralow-Voltage-Drivable Artificial Muscles Based on a 3D Structure MXene-PEDOT:PSS/AgNWs Electrode. *ACS Appl. Mater. Interfaces* **2022**, *14*, 18150–18158.

(7) Zhang, Y.; Gao, H.; Wang, H.; Xu, Z.; Chen, X.; Liu, B.; Shi, Y.; Lu, Y.; Wen, L.; Li, Y.; Li, Z.; Men, Y.; Feng, X.; Liu, W. Radiopaque Highly Stiff and Tough Shape Memory Hydrogel Microcoils for Permanent Embolization of Arteries. *Adv. Funct. Mater.* **2018**, *28*, 1705962.

(8) Zeng, H.; Wani, O. M.; Wasylczyk, P.; Kaczmarek, R.; Priimagi, A. Self-Regulating Iris Based on Light-Actuated Liquid Crystal Elastomer. *Adv. Mater.* **2017**, *29*, 1701814.

(9) Ji, X.; Liu, X.; Cacucciolo, V.; Civet, Y.; El Haitami, A.; Cantin, S.; Perriard, Y.; Shea, H. Untethered Feel-Through Haptics Using 18-μm Thick Dielectric Elastomer Actuators. *Adv. Funct. Mater.* **2021**, 2006639.

(10) Ming, Y.; Yang, Y.; Fu, R. P.; Lu, C.; Zhao, L.; Hu, Y. M.; Li, C.; Wu, Y. X.; Liu, H.; Chen, W. IPMC Sensor Integrated Smart Glove for Pulse Diagnosis, Braille Recognition, and Human-Computer Interaction. *Adv. Mater. Technol.* **2018**, *3*, 1800257.

(11) Rahman, M. H.; Werth, H.; Goldman, A.; Hida, Y.; Diesner, C.; Lane, L.; Menezes, P. L. Recent Progress on Electroactive Polymers: Synthesis, Properties and Applications. *Ceramics* **2021**, *4*, 516–541.

(12) Shoa, T.; Madden, J. D. W.; Mirfakhrai, T.; Alici, G.; Spinks, G. M.; Wallace, G. G. Electromechanical Coupling in Polypyrrole Sensors and Actuators. *Sens. Actuator. A* **2010**, *161*, 127–133.

(13) Wang, T.; Farajollahi, M.; Choi, Y. S.; Lin, I-. T.; Marshall, J. E.; Thompson, N. M.; Narayan, S. K-.; Madden, J. D. W.; Smoukov, S. K. Electroactive Polymers for Sensing. *Interface Focus.* **2016**, *6*, 20160026.

(14) Chen, S.; Tan, M. W. M.; Gong, X.; Lee, P. S. Low-Voltage Soft Actuators for Interactive Human-Machine Interfaces. *Adv. Intell. Syst.* **2021**, 2100075.

(15) Nguyen, V. H.; Kim, J.; Tabassian, R.; Kotal, M.; Jun, K.; Oh, J-. H.; Son, J-. M.; Manzoor, M. T.; Kim, K. J.; Oh, I-. K. Electroactive Artificial Muscles Based on Functionally Antagonistic Core-Shell Polymer Electrolyte Derived from PS-*b*-PSS Block Copolymer. *Adv. Sci.* **2019**, *6*, 1801196.

(16) Wang, Y.; Sugino, T. Ionic Polymer Actuators: Principle, Fabrication and Applications. *Actuators* DOI: 10.5772/intechopen.75085.

(17) Gonçalves, R.; Tozzi, K. A.; Saccardo, M. C.; Zuquello, A. G.; Scuracchio, C. H. Nafion-based Ionomeric Polymer/Metal Composites Operating in the Air: Theoretical and Electrochemical Analysis. *J. Solid. State. Electrochem.* **2020**, *24*, 1845–1856.

(18) Wang, H. S.; Cho, J.; Song, D. S.; Jang, J. H.; Jho, J. Y.; Park, J. H. High-Performance Electroactive Polymer Actuators Based on Ultrathick Ionic Polymer-Metal Composites with Nanodispersed Metal Electrodes. *ACS Appl. Mater. Interfaces* **2017**, *9*, 21998–22005.

(19) Hu, F.; Xue, Y.; Xu, J.; Lu, B. PEDOT-Based Conducting Polymer Actuators. *Actuators. Front. Robot. AI* **2019**, 114. doi: 10.3389/frobt.2019.00114.

(20) Kotal, M.; Kim, J.; Kim, K. J.; Oh, I-. K. Sulfur and Nitrogen Co-Doped Graphene Electrodes for High-Performance Ionic Artificial Muscles. *Adv. Mater.* **2016**, *28*, 1610-1615.

(21) Zhu, X.; Hu, Y.; Wu, G.; Chen, W.; Bao, N. Two-Dimensional Nanosheets-Based Soft Electro-Chemo-Mechanical Actuators: Recent Advances in Design, Construction, and Applications. *ACS Nano* **2021**, *15*, 9273−9298.

(22) Raza, U.; Oh, S.; Tabassian, R.; Mahato, M.; Nguyen, V. H.; Oh, I-. K. Micro-Structured Porous

Electrolytes for Highly Responsive Ionic Soft Actuators. *Sens. Actuators B* **2022**, *352*, 131006.
(23) Kim, O.; Shin, T. J.; Park, M. J. Fast Low-Voltage Electroactive Actuators using Nanostructured Polymer Electrolytes. *Nature Comm.* **2013**, *4*, 2208.
(24) Park, J.; Staiger, A.; Mecking, S.; Winey, K. I. Sub-3-Nanometer Domain Spacings of Ultrahigh-χ Multiblock Copolymers with Pendant Ionic Groups. *ACS Nano* **2021**, 15, 16738–16747.
(25) Sinturel, C.; Bates, F. S.; Hillmyer, M. A. High χ-Low N Block Polymers: How Far Can We Go? *ACS Macro Lett.* **2015**, *4*, 1044–1050.
(26) Kim, J.; Kang, Y.; Yun, S. Blocked Force Measurement of Electro-Active Paper Actuator by Micro-Balance. *Sens. Actuators A* **2007**, *133*, 401–406.
(27) Knight, G. A.; Shaw, B. D. Long-Chain Alkylpyridines and Their Derivatives. New Examples of Liquid Crystals. *J. Chem. Soc.* **1938**, 682−683.
(28) Goossens, K.; Lava, K.; Bielawski, C. W.; Binnemans, K. Ionic Liquid Crystals: Versatile Materials. *Chem. Rev.* **2016**, *116*, 4643−4807.
(29) Matsumoto, T.; Ichikawa, T.; Sakuda, J.; Kato, T.; Ohno, H. Design of Amphiphilic Zwitterions Forming Liquid-Crystalline Phases and Effects of Lithium Salt Addition on Their Phase Behavior. *Bull. Chem. Soc. Jpn.* **2014**, *87*, 792796.
(30) Ichikawa, T.; Yoshio, M.; Hamasaki, A.; Kagimoto, J.; Ohno, H.; Kato, T. 3D Interconnected Ionic Nano-Channels Formed in Polymer Films: Self-Organization and Polymerization of Thermotropic Bicontinuous Cubic Liquid Crystals. *J. Am. Chem. Soc.* **2011**, *133*, 2163–2169.
(31) Hamaguchi, K.; Ichikawa, R.; Kajiyama, S.; Torii, S.; Hayashi, Y.; Kumaki, J.; Katayama, H.; Kato, T. Gemini Thermotropic Smectic Liquid Crystals for Two-Dimensional Nanostructured Water-Treatment Membranes. *ACS Appl. Mater. Interfaces* **2021**, *13*, 20598−20605.
(32) Huang, Z.; Qi, P.; Liu, Y.; Chai, C.; Wang, Y.; Song, A.; Hao, J. Ionic-Surfactants-based Thermotropic Liquid Crystals. *Phys. Chem. Chem. Phys.* **2019**, *21*, 15256−15281.
(33) Wu, H.; Xu, F.; Gao, G.; Feng, X. Highly Ordered Interconnected 1 nm Pores in Polymers Fabricated from Easily Accessible Gyroid Liquid Crystals. *Macromolecules* **2021**, *54*, 5856−5865.
(34) Zhang, Y.; Dong, R.; Gabinet, U. R.; Poling-Skutvik, R.; Kim, N. K.; Lee, C.; Imran, O. Q.; Feng, X.; Osuji, C. O. Rapid Fabrication by Lyotropic Self-Assembly of Thin Nanofiltration Membranes with Uniform 1 Nanometer Pores. *ACS Nano* **2021**, *15*, 8192–8203.
(35) Li, P.; Johnson, C.; Dyer, S. S.; Osuji, C. O.; Gin, D. L. A pH- and Light-Responsive Nanoporous Lyotropic Gyroid Polymer Network. *Adv. Mater. Interfaces* **2023**, 10, 2201761.

Chapter 2

Low-Voltage-Driven Actuators Using Photo-Cross-Linked Ionic Columnar Liquid-Crystalline Polymer Films

2.1 Introduction.

Ionic electroactive polymer (iEAP) actuators have been intensively investigated for their use in the potential applications, such as soft grippers, active catheters, and haptic devices.[1–5] The large deformation induced by ion diffusion at low driving voltage (few volts) is beneficial for such applications, compared with piezoelectric and dielectric polymer actuators that require high driving fields of several 10 V μm^{-1}. Polymer electrolytes are one of the essential components to achieve high performance in iEAP actuators. Conventionally, amorphous polymer ion gels containing ionic liquids and hydrated ionic polymers, like Nafion have been employed as polymer electrolytes.[6–8] However, they have drawbacks of low force generation and poor durability under long term actuation in air, mainly because of the lack of mechanical robustness and leakage of the inner electrolytes and water. Currently, several approaches have been reported to obtain ionic liquid-containing nanostructured polymer electrolytes with high ionic conductivities and mechanical toughness, such as using block copolymer self-assembly[9–12] and geometric engineering in polymer blends[13] and electrode-electrolyte interfaces.[14,15] Although these nanostructured polymers have improved the leakage problems of electrolytes, their deformability and generation force remain insufficient. It is a great challenge to develop new nanostructured polymer electrolytes that combine the contradictory functions of high ionic conductivity and high elastic modulus for the next generation of iEAP actuators. Our strategy is a confinement of ionic liquids into one-dimensional ion channels formed in photo-cross-linked ionic columnar liquid-crystalline polymer matrices to form more mobile continuous ion transport pathways.

Self-assembly of nano-segregated liquid crystals and subsequent interlocking of the structures by *in-situ* photo-polymerization play critical roles in producing ion-active and mechanically tough polymer membranes.[16–21] Our group previously reported a diverse range of nanostructured polymer electrolytes forming 1D to 3D ion channels through self-assembly of columnar, smectic, and bicontinuous cubic ionic liquid crystals.[16,22,23] For example, by using *in-situ* photo-polymerization of columnar ionic liquid-crystalline phase of a polymerizable fan-shaped imidazolium salt with diacrylate groups (**DA**, **Figure 2.1**) that formed vertical columnar orientation on a chemically modified surface,[22] we have successfully developed the first example of a one-dimensionally ion-conductive

freestanding polymer film. It was found that the through-plane conductivity of the nanostructured polymer membrane was three orders of magnitude higher than the in-plane membrane conductivity at 100 °C. However, the very low conductivity at ambient temperature limited its applications as practical use in electrochemical energy devices. I envisaged that the incorporation of fluidic ionic liquids into the nano-channels should increase the conductivity while maintaining the continuity of the channels, which can expand their applicability in a variety of fields including iEAP actuators, carbon dioxide gas separation,[24] and water-treatments.[25,26]

In this chapter, I show two-voltage driven nanostructured iEAP actuators using the columnar ionic liquid-crystalline polymer film of **DA**, featuring a confinement of ionic liquid (**IL**) into the 1D ion channels. The freestanding flexible nanostructured membrane organizing 30 mol% of **IL** (7.9 wt%) was sandwiched between two conductive polymer electrodes, poly(3,4–ethylene dioxythiophene) doped with poly(styrene sulfonate) (**PEDOT:PSS**). I successfully demonstrated the faster and larger bending displacement and higher force generation for the nanostructured polymer membrane actuators, compared with the corresponding non-ordered actuator using the amorphous membrane obtained by photo-preservation of **DA** in the isotropic liquid (Iso) phase.

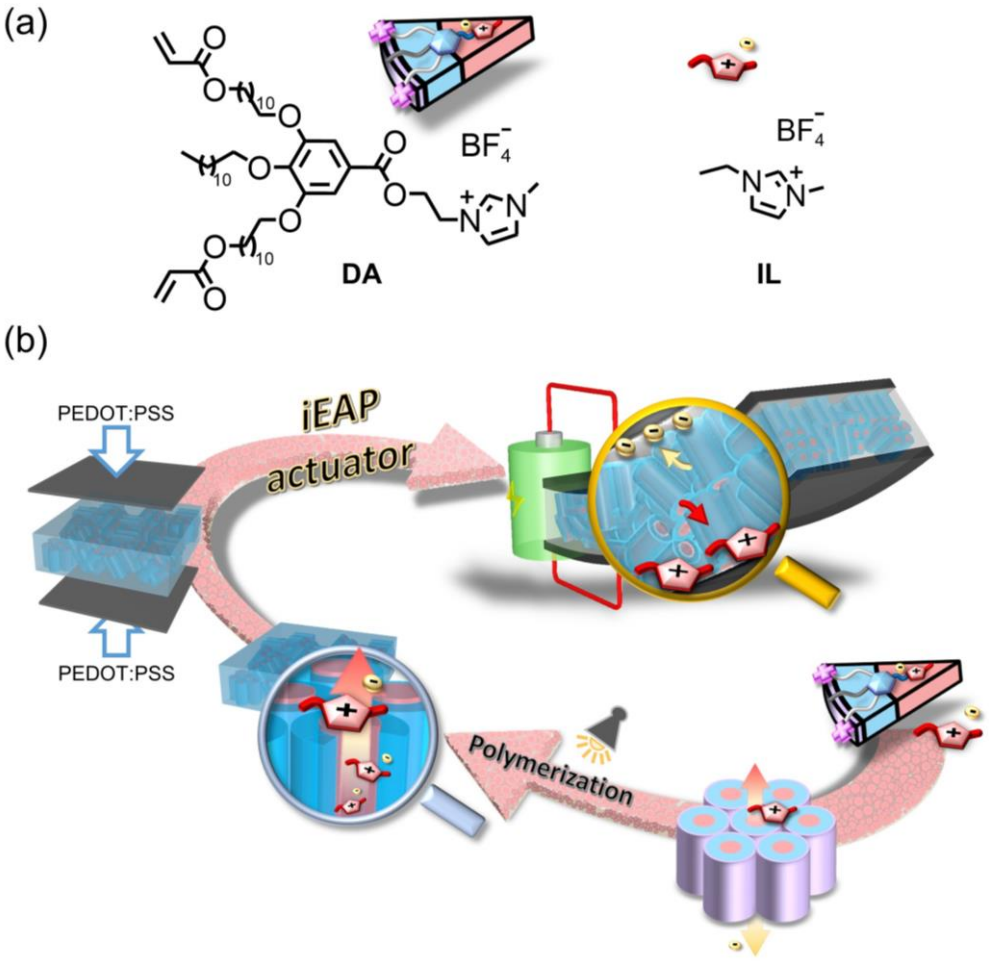

Figure 2.1 (a) Molecular structures of wedge-shaped imidazolium compound with diacrylate groups (**DA**) and ionic liquid [EMIM][BF_4] (**IL**). (b) Illustration of our design concept: photo-polymerizable ionic liquid-crystalline membrane was sandwiched by a pair of poly(thiophene)-based electrode (**PEDOT:PSS**) to afford iEAP actuators with 1D ion transport channels.

2.2 Experimental Section.

2.2.1 Materials.

A liquid-crystalline compound (**DA**), 3–{3,5–bis(11–acryloxyloxyundecyloxy)–4–dodecyloxybenzolyloxyethyl}–1–methylimidazolium tetrafluoroborate, was synthesized by the same procedure reported in our previous paper.[22] 1–Ethyl–3–methylimidazolium tetrafluoroborate (**IL**) was purchased from Tokyo chemical industry. Poly(3,4–ethylene dioxythiophene) polystyrene sulfonate **PEDOT:PSS** (Clevios™ PH1000) was purchased from Heraeus. Ethylene glycol was purchased from Kanto chemical. 2,2–Dimethoxy–2–phenylacetophenone as a photo-initiator was purchased from Sigma-Aldrich. All the chemicals were used as received without further purification.

2.2.2 General methods.

Attenuated total reflection-Fourier transform infrared (ATR-FTIR) spectroscopy was conducted using a BRUKER FT-IR ALPHA II spectrometer equipped with a single bounce diamond ATR module. Differential scanning calorimetry (DSC) measurements were carried out under a continuous argon purge (40 mL/min) by using NETZSCH DSC-3500 Sirius connected with a liquid nitrogen cryo-system. The heating and cooling scan rate is 10 ºC/min. Polarizing optical microscopic observation was conducted using Olympus BX51N-31P-O3 with a digital camera DP22 and a temperature control system (LINKAM T95-HS, LTS420E). X-ray diffraction measurements were carried on a Rigaku MiniFlex 600 diffractometer using Ni-filtered Cu Kα radiation. A 100 W Xenon lamp (Asahi Spectra, HAL-C100) equipped with a UV mirror module and bandpass filters was employed as an UV irradiation source. The cyclic voltammetry measurements were carried out using a CH Instruments (ALS Electrochemical Analyzer, model 611E).

2.2.3 Preparation of self-standing PEDOT:PSS films.

Ethylene glycol (0.3 g) was added into a **PEDOT:PSS** aqueous solution (3 ml) and vigorously stirred for 1 hour. Subsequently, the mixed solution was transferred to ABS plastic tip trays (Nihon Entegris, Inc) and dried at 60 ºC for 4 hours. The resultant gelatinous films containing solvents were peeled off from the substrate and placed on a Teflon plate. After vacuum drying at 120 ºC for 4 hours, the self-standing conductive **PEDOT:PSS** film (300-500 S cm^{-1}) was obtained. The electrical conductivity of the films

was evaluated by four-point method with a Loresta-GX (MCP-T700, Nittoseiko Analytech Co., Ltd.).

2.2.4 Preparation of photo-cross-linked polymer films and actuator.

Compounds **DA** and **IL** in the 7:3 molar ratio and 2,2–dimethoxy–2–phenylacetophenone (0.1 wt% to the mixture of **DA** and **IL**) were dissolved in a mixed solution of chloroform/methanol (4/1 in volume) and the solvents were removed by rotary evaporator under light resistant conditions. The residue was dried under vacuum at 30 °C for 1 day to give the liquid-crystalline sample of **DA/IL(30)** at room temperature.

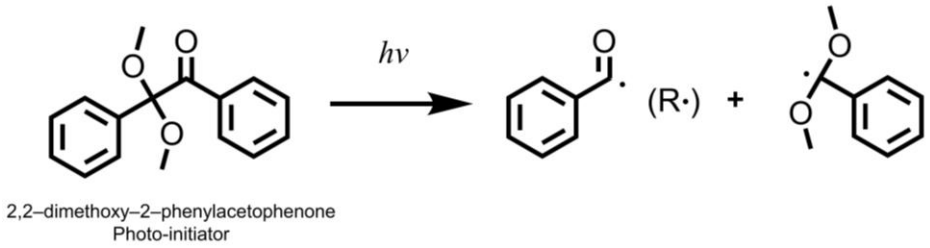

Scheme 2.1 Chemical structure of photo-initiator and initiation program (free radical generation: R•) by using UV irradiation (*hv*).

Scheme 2.2 shows the schematic illustration for the preparation of freestanding polymer films, **P_{Col}/IL(30)** and **P_{Iso}/IL(30)**, and their actuation strips. **Step 1**: The monomeric sample **DA/IL(30)** in the Col phase was placed between the cover glass and glass substrate covered with polyimide tape. The thickness of the sample was fixed using 35 μm thick polyimide (PI) tape spacer. **Step 2**: The sandwiched cell was heated to a temperature at which the sample became the isotropic liquid state and then cooled to room temperature at the rate of 1 °C/min to increase the domain size of vertically oriented columnar liquid crystal. Subsequently, the cell was irradiated with UV light (365 nm, 5.5 mW/cm^2) for 150 seconds at room temperature. **Step 3**: The resultant **P_{Col}/IL(30)** film was carefully peeled off from the substrate. **Step 4**: The **P_{Col}/IL(30)** film was sandwiched between two conductive **PEDOT:PSS** sheets and pressed by hand. The three-layered film was cut into 15 mm × 4 mm pieces to evaluate the performance of the actuator. The **P_{Iso}/IL(30)** film was similarly obtained by UV irradiating the cell filled with **DA/IL(30)** in the isotropic liquid state on a hot plate and then peeling the film from the substrate.

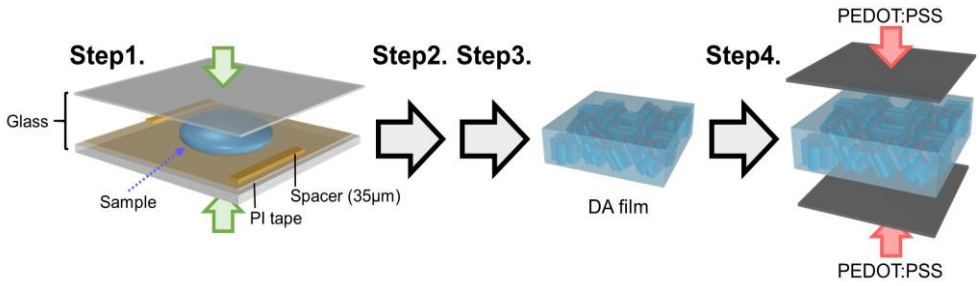

Scheme 2.2 Preparation of $\mathbf{P_{Col}/IL(30)}$ polymer film and its actuator.

2.2.5 Measurement of ionic conductivity.

Alternating current impedance measurements were carried out using a Metrohm AUTOLAB PGSTAT128N impedance analyzer. The frequency range is 10^7-10^2 Hz and the applied voltage is 0.6 V. The monomer, **DA/IL(x)**, was sandwiched between a pair of indium tin oxide (ITO)-coated glass substrates using a 35 μm thick polyimide tape spacer with a 3 mm diameter hole. The temperature was controlled by using a Linkam hot stage. The impedance data were recorded every 5 °C in the temperature range of 25-70 °C during the heating process. The impedance data were fitted by the equivalent circuit consisting of a constant phase element and a parallel RC element. The ionic conductivity σ (S cm^{-1}) was calculated according to equation (1), where R_b is the bulk resistance (Ω), L is the sample thickness (cm), and A is the sample area (cm^2). The R value was obtained from the intercept of the semicircle on the real axis of impedance in Nyquist plots.

$$\sigma = \frac{L}{R_b A} \tag{1}$$

The temperature-dependent ionic conductivities can be fitted by the Arrhenius equation (2), where R is a gas constant (8.314 J K mol^{-1}), T is the temperature in Kelvin, and σ_0 is the pre-exponential factor. The activation energy (E_a) was estimated from the slope of line obtained by using the logarithmically transformed Arrhenius equation (3).

$$\sigma = \sigma_0 e^{\left(\frac{-E_a}{RT}\right)} \tag{2}$$

$$ln\frac{\sigma}{\sigma_0} = \frac{-E_a}{R} \times \frac{1}{T} \tag{3}$$

2.2.6 Actuation performance test.

The actuator strip with a copper foil on one end was clamped between two stainless steel electrodes connected to a potentiostat (Hokudo Denko, HAL3001A). Symmetrical square-wave alternating voltages or DC voltages generated by a function generator (YOKOGAWA FG400 30MHz) were controlled by the potentiostat and applied to the actuator strip. The bending displacement was measured by using a laser meter (Keyence, LK-H050 and LK-HD500). The laser was irradiated perpendicular to the surface of actuator at 10 mm away from the tip of strip. The signals of voltage, current, and displacement were recorded in a MEMORY HiLOGGER (HIOKI LR8880). The actuating behavior was captured using a USB microscope camera (Sanwa Supply, 400-CAM058). The blocking force measurement was carried out by the load sensor and force detection monitor (KYOWA LTS-50GA / KYOWA WGA-680A).

The blocking force (F_{bl}) of actuators depends on the sample volume according to the equation (4), where w, t, and l are the width, thickness, and free length of the actuator, respectively.

$$F_{\mathrm{bl}} \propto \frac{wt^2}{l} \tag{4}$$

Therefore, the experimantally obtained blocking force ($F_{\mathrm{exp.}}$) using a load cell was normalized using the following equation (5) to give the normalized blocking force ($F_{\mathrm{Nor.}}$).

$$F_{\mathrm{Nor.}} = \frac{F_{\mathrm{exp.}} l}{wt^2} \tag{5}$$

2.3 Results and Discussion.

2.3.1 Characteristic of ionic liquid-crystalline mixture.

Selecting of appropriate ionic liquids as non-volatile lyotropic solvents and electrolytes is a key to inducing nanostructured liquid-crystalline phases and achieving high ionic conductivity. To obtain room-temperature columnar liquid crystals confining ionic liquids into the ionic channels of **DA**, I examined the miscibility of **DA** and various imidazolium-based ionic liquids such as 1–ethyl–3–methylimidazolium bis(trifluoromethylsulfonyl)imide ([EMIM][TFSI]) and 1–butyl–3–methylimidazolium tetrafluoroborate ([BMIM][BF_4]). The combination of **DA** and 1–ethyl–3–methylimidazolium tetrafluoroborate ([EMIM][BF_4]) (**IL**) in the various compositions provided the room-temperature columnar liquid crystals, while other ionic liquid mixtures became the liquids at ambient temperature. The size, shape, and ionicity of ionic liquids are delicate for the induction of the columnar liquid-crystalline phase. **IL** is one of the promising liquid electrolytes for fabricating nanostructured actuators because it exhibits the highest ionic conductivity among the conventional ionic liquids.[13, 27-29]

Figure 2.2 shows the phase diagram of the binary mixtures of **DA** and **IL** (**DA/IL(x)**) as a function of the mole% (**X**) of **IL** in the mixture and the plots of *d*-spacing value assigned to the X-ray diffraction from the (100) plane of the columnar (Col) phase. The homogeneous mixtures forming the Col phase are obtained up to 40 mole% of **IL**. As the **IL** content increases, the temperature range of the Col phase is decreased. For example, **DA/IL(30)** shows the Col-Iso phase transition at 36.9 °C (**Figure 2.3**), whereas the transition of **DA** alone is observed at 50.0 °C. In addition, the intercolumnar distance is increased by the addition of **IL**. Monomeric **DA** gives the d_{100} value of 36.8 Å, and the d_{100} value for monomeric **DA/IL(40)** is 42.4 Å. These results suggest that the incorporation of **IL** in the center of the columns results in the formation of highly mobile one-dimensional ion channels with larger diameter.

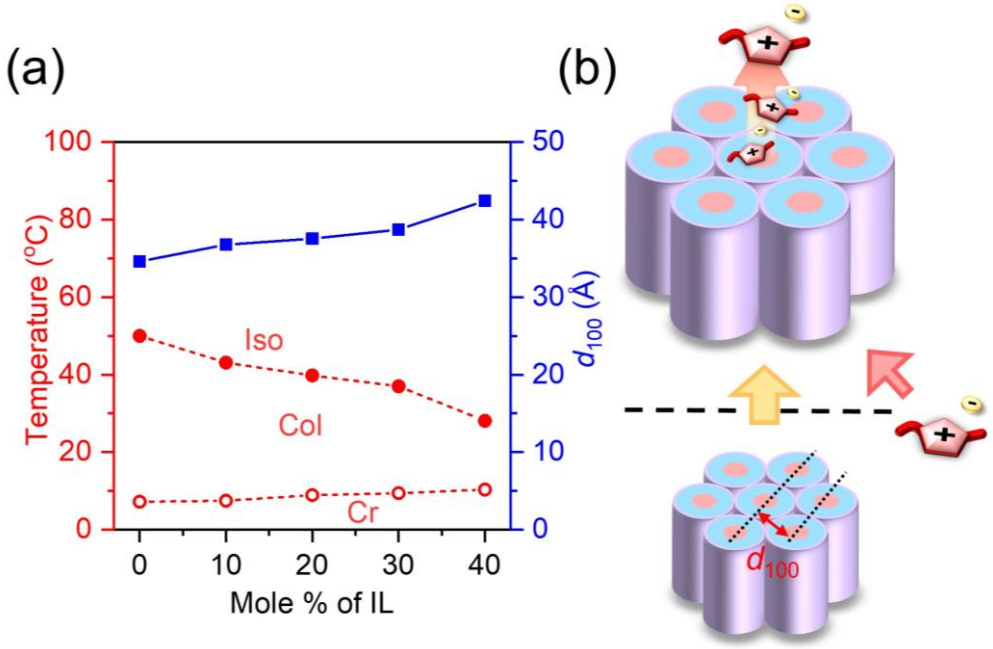

Figure 2.2 (a) Phase transition temperatures of the binary mixtures of **DA** and **IL** as a function of the mole% of **IL**, and the *d*-spacing value assigned to the X-ray diffraction of the (100) plane of the columnar phase. Iso, Col, and Cr are isotropic liquid, columnar, and crystalline, respectively. (b) Illustration of the swelling in non-polymerized columnar ionic channels by incorporating ionic liquid.

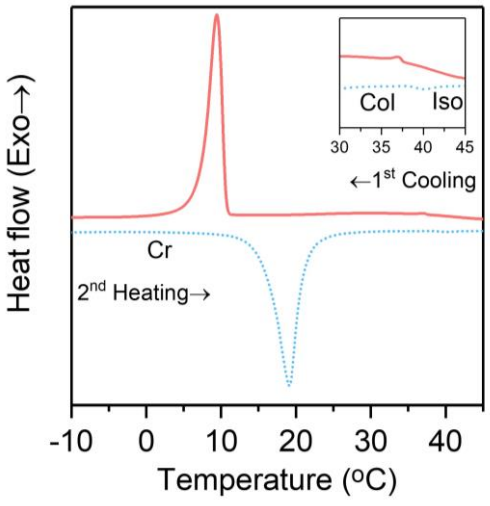

Figure 2.3 DSC thermograms of **DA/IL(30)**. The inset shows the magnified chart in a temperature range of 30-45 °C.

Monomeric mixture **DA/IL(x)** (**x** = 10-40) formed the polydomain columnar structures in a sandwiched glass cell with the gap of 35 μm by slow cooling from the isotropic liquid state, although previously report achieved the homeotropic alignment of columns up to 10 μm thickness for **DA** alone.[22] The polarized optical microscopic image of **DA/IL(30)** (**Figure 2.4(a)**) shows a mixed texture with black regions indicating vertical alignment and birefringent regions due to planar and tilted columnar orientations.

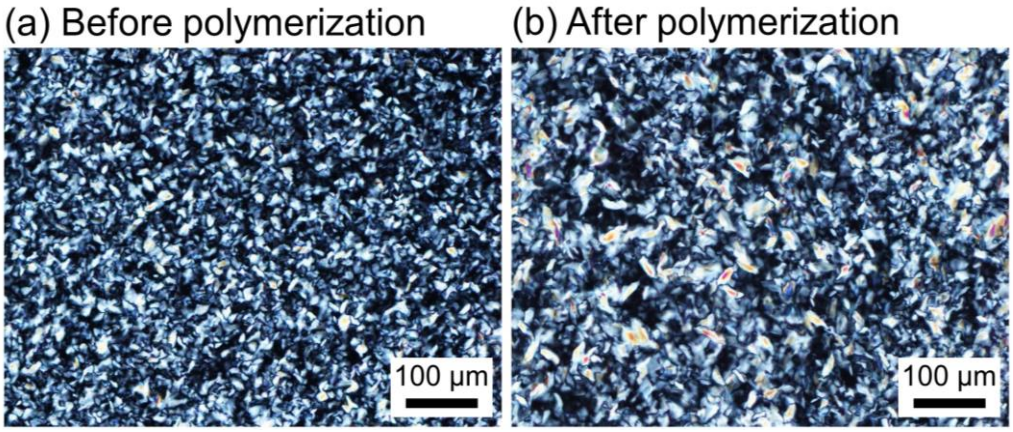

Figure 2.4 Polarizing optical micrographs of **DA/IL(30)** at room temperature (a) before and (b) after UV light irradiation.

The photopolymerization of **DA/IL(x)** in the Col phases were examined to obtain high ion-conductive polymer films with sufficient mechanical properties to be used as iEAP actuators. The prolonged UV irradiation at a power density of 5.5 mW/cm^2 for 150 seconds resulted in a freestanding and flexible polymer film preserving the Col orientation (**Figure 2.4(b)**). The FT-IR spectrum confirmed the polymerization, as the stretching bands of acrylate at 1636 and 811 cm^{-1} were hardly observed (**Figure 2.5**). In addition, the photopolymerization of monomeric mixtures in the Iso phases produced the flexible amorphous films. Hereafter, the polymer films obtained by photo-crosslinking **DA/IL(x)** in the Col and Iso phases are denoted as **P$_{Col}$/IL(x)** and **P$_{Iso}$/IL(x)**, respectively.

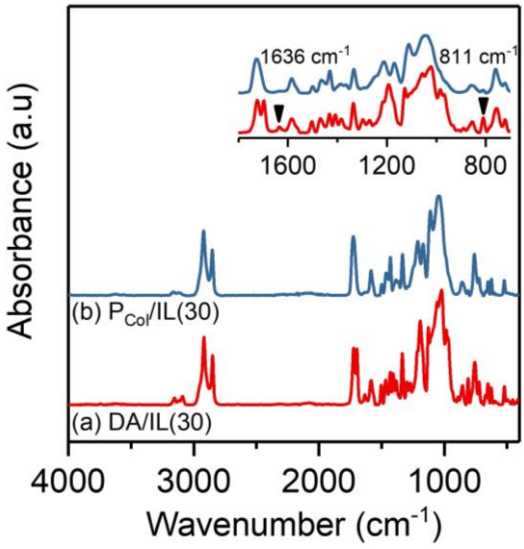

Figure 2.5 ATR-FTIR spectra of (a) **DA/IL(30)** and (b) **P_{Col}/IL(30)**. The inset shows the magnified spectra in a wavenumber range of 1800-700 cm^{-1}.

2.3.2 Physicochemical and electrochemical analysis.

The ionic conductivity for the polymer films increased with an increase in the mole% of **IL** (**Figure 2.6 (a)**). The activation energies (E_a) for **P_{Col}/IL(0)** and **P_{Col}/IL(30)** are estimated to be 66 kJ/mol and 60 kJ/mol, respectively. It is noteworthy that **P_{Col}/IL(30)** exhibits eight times higher ionic conductivity at 25 °C compared to **P_{Iso}/IL(30)** (**Figure 2.6 (b)**). Besides, the activation energy of **P_{Col}/IL(30)** is smaller than that of **P_{Iso}/IL(30)** (E_a = 82 kJ/mol). The formation of columnar ionic channels confining ionic liquids is a significant key to achieve an efficient ion transport. Moreover, **P_{Col}/IL(30)** maintains the anisotropic structure up to 150 °C and possesses the glass transition temperature at -14 °C attributed to the assembled ionic moieties (**Figure 2.7**). Alignment of columns is essential way to achieve high ionic conductivity. The concept of nanosegregation, consisting of liquid-like ion-conductive and rigid mesogenic domains, may lead to new designs of iEAP actuators that combine high elasticity for power generation and high conductivity for bendability.

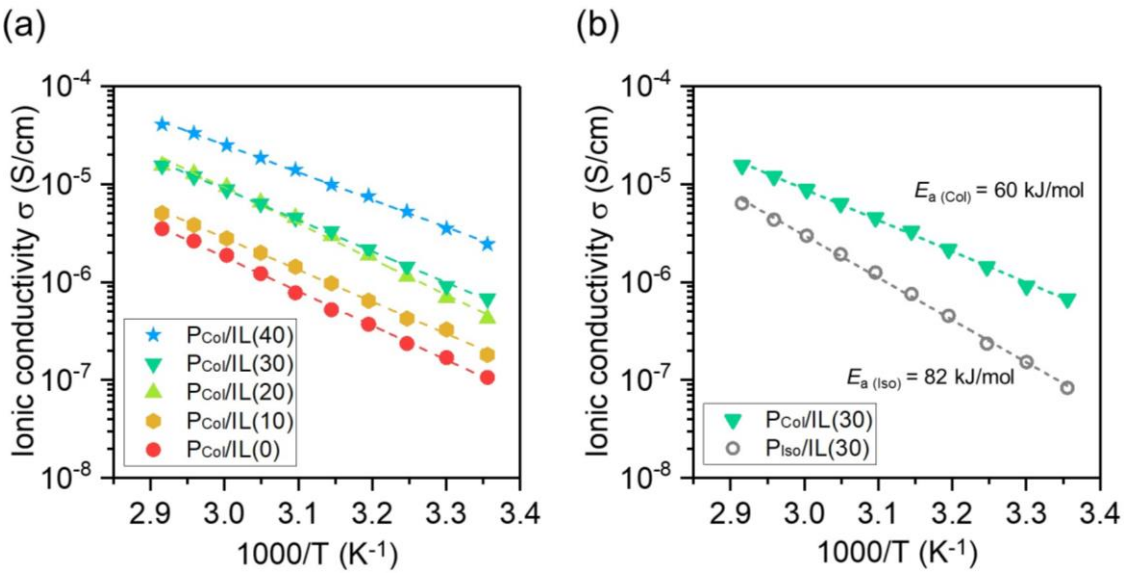

Figure 2.6 (a) Temperature dependence of ionic conductivity for the columnar nanostructured polymer films of **P_{Col}/IL(x)** with different mole% of IL. (b) Comparison of the conductivity for the columnar polymer film **P_{Col}/IL(30)** (triangle) and the amorphous polymer film **P_{Iso}/IL(30)** (open circle). The dashed lines are fit by the Arrhenius equation.

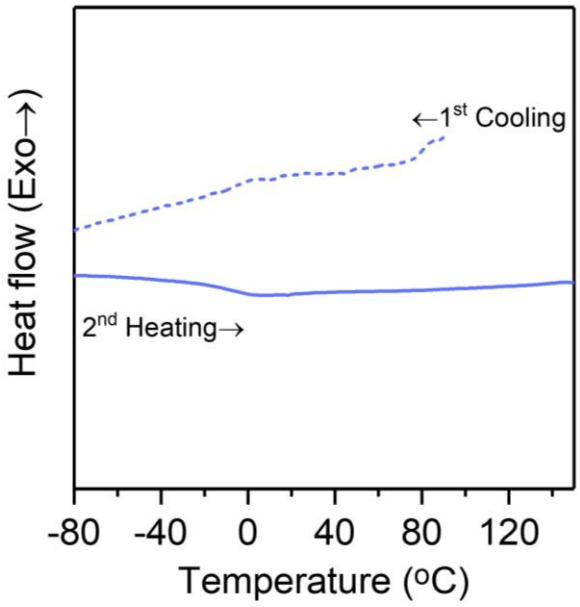

Figure 2.7 DSC thermograms of **P_{Col}/IL(30)**.

2.3.3 Bending actuation for ionic LC actuators.

Figure 2.8 (a) shows the bending displacement of the actuator strip under applying an alternating current (AC) square voltage of ± 2 V at a frequency of 0.01 Hz under ambient condition. The actuator strip showed a bending motion to the anode side. The size of the imidazolium cation of **IL** is larger than that of the tetrafluoroborate anion. It has been reported that the cationic transference number in neat **IL** is larger than that of anion by PGSE-NMR experiments.[30,31] Therefore, the faster migration of cations confined in the channels to the cathode may cause the swelling of the cathode layer, although the polarization of the columnar liquid-crystalline polymer under electric fields should also contribute to the bending displacement. In fact, the tri-layered actuator strip of **P_{Col}/IL(0)** without ionic liquid and **PEDOT:PSS** showed a slight bending actuation upon application of voltages (maximum displacement of 30 μm under 2 V at 0.01 Hz). To gain further insight into the actuation mechanism, cyclic voltammetry measurements were conducted for the **P_{Col}/IL(0)** and **P_{Col}/IL(30)**-based actuators. The cyclic voltammogram of the **P_{Col}/IL(30)** actuator shows a capacitive current-voltage behavior (**Figure 2.9**), although the capacitive saturation of the current is not reached as resistive contributions decrease the overall current. In addition, no Faradic current due to the redox reactions between **IL** and **PEDOT:PSS** is seen. On the contrary, for the **P_{Col}/IL(0)**

without ionic liquids, no capacitive and Faradic currents are observed. These results indicate that the columnar liquid-crystalline polymer matrix (**P_{Col}/IL(0)**) only served as a nanostructured reservoir for the ionic liquid.

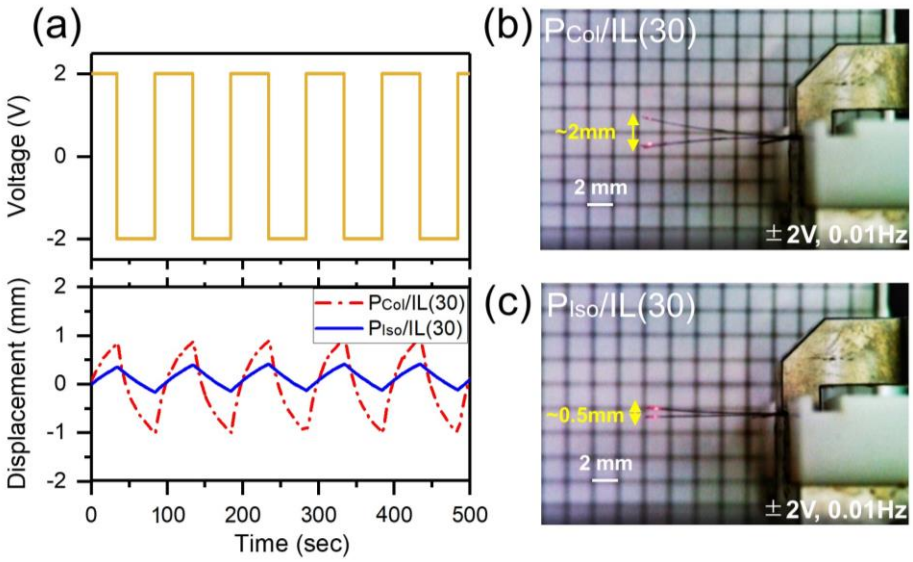

Figure 2.8 Actuation response of the columnar and amorphous polymer film electrolytes sandwiched between **PEDOT:PSS** electrodes. (a) Applied voltage and tip displacement under an AC voltage of 2 V at a frequency of 0.01 Hz. (b) and (c) Photographs of the columnar and amorphous actuators bending at ± 2 V and 0.01 Hz, respectively.

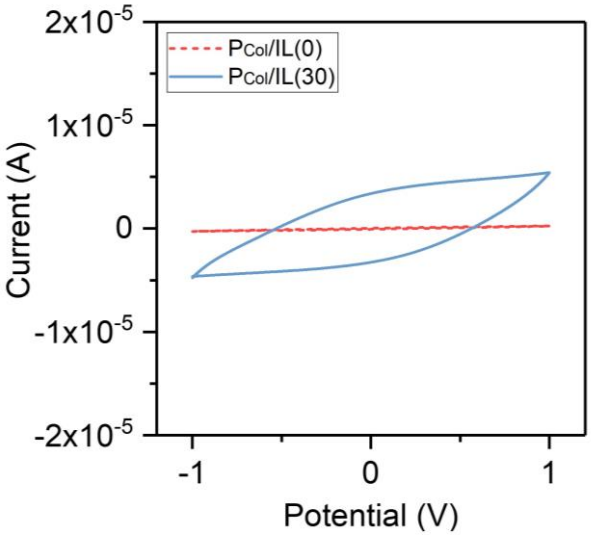

Figure 2.9 Cyclic voltammograms of the actuators based on **P_{Col}/IL(0)** and **P_{Col}/IL(30)** films sandwiched between **PEDOT:PSS** electrodes with the potential range of -1 to 1 V at scan rate of 1 mV s^{-1}.

The maximum peak-to-peak tip displacement of **P_{Col}/IL(30)**-based actuator reaches 2 mm, while **P_{Iso}/IL(30)**-based actuator shows the maximum displacement of 0.5 mm. **Figure 2.10 (a)** shows the peak-to-peak bending strain of the actuators based on **P_{Col}/IL(30)** and **P_{Iso}/IL(30)** under applying 2 V with the frequency of 0.01, 0.05, 0.1, 0.5, and 1 Hz. The bending strain was calculated by the following equation: $\varepsilon = 2\delta d \times 100/(\delta^2 + L^2)$,[32] where δ is the peak-to-peak displacement, d is the total thickness of actuator, and L is the free length of strip. At the frequency of 0.01 Hz, the bending strain of **P_{Col}/IL(30)**-based actuator (ε = 0.20 %) showed about two times larger than that of **P_{Iso}/IL(30)**-based actuator (ε = 0.09 %). This may be due to the increased ion migration through the partially continuous ion channels from the nanostructured polymer electrolyte to the electrode surface. For **P_{Iso}/IL(30)**, the ionic liquid may be encapsulated in insulating and rigid polymerized mesogenic domains, which leads to very slow diffusion of ions. In contrast, the **P_{Col}/IL(30)**-based actuator at 1 Hz exhibited a bending motion with the strain value of 0.0032 %, whereas no bending behavior was observed for **P_{Iso}/IL(30)**. These results indicate that at frequencies higher than 1 Hz, the disordered polymer matrix cannot store enough charges in the electrodes to cause bending actuation, even though it contains the same number of ions as the columnar polymer matrix. In addition, the **P_{Col}/IL(30)**-based columnar actuator showed 3.5 times faster response than the amorphous **P_{Iso}/IL(30)**-based actuator (**Figure 2.10 (b)**). The **P_{Col}/IL(30)**-based columnar actuator also exhibited fair cycling stability under 2 V at 1 Hz with strain degradation of 8 % after 2000 cycles (**Figure 2.10 (c)**).

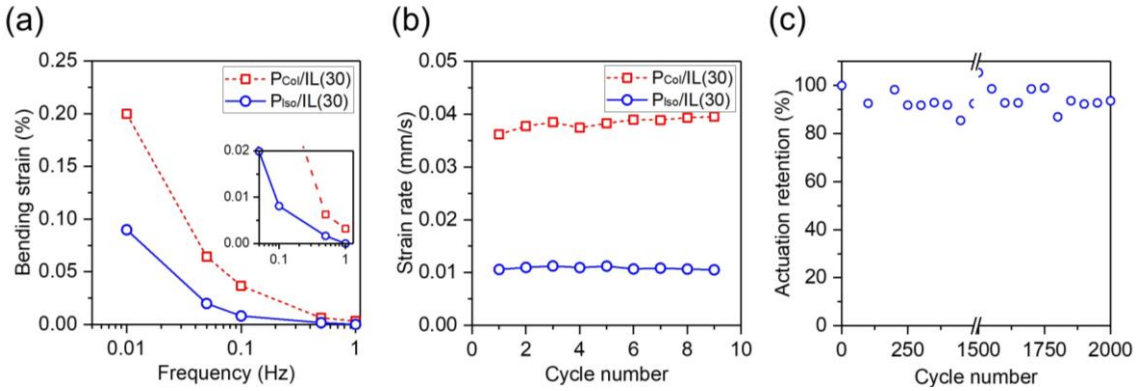

Figure 2.10 (a) Bending strain (%) of actuators at AC 2 V with the frequency range from 0.01 Hz to 1 Hz. (b) Strain rate of the actuators derived from the displacement *vs* time plots in **Figure 2.10 (a)**. (c) Cyclic stability of the columnar polymer film actuator under 2 V at 1 Hz. The bending strain for each cycle is normalized by the initial strain value.

2.3.4 Generation force from bending actuators.

The **P_{Col}/IL(30)**-based columnar actuator can yield a blocking force of 0.28 mN when an AC bias of ± 2 V at 0.01 Hz is applied (**Figure 2.11 (a)**), which is twice larger than that obtained for **P_{Iso}/IL(30)**-based actuator. The generated force was reduced by decreasing the applied voltage (**Figure 2.11 (b)**) and controlled with step changes in voltage (**Figure 2.12**). Moreover, lifting an aluminum foil of 10–60 mg was successfully demonstrated for the **P_{Col}/IL(30)**-based columnar actuator (size: 12 mm × 4 mm × 61 μm, weight: 2.9 mg) under applying DC 2 V (**Figure 2.11 (c)**) and the actuator was able to lift objects at least three times its own weight. The lifting angle of the actuator was proportional to the load weight (**Figure 2.11 (d)**). The force generation of the **P_{Col}/IL(30)**-based columnar actuator containing 7.9 wt% of **IL** is comparable to polymer ion gel actuators, composed of thermoplastic polyurethane containing 80 wt% of ionic liquid (1–ethyl–3–methylimidazolium bis(trifluoromethylsulfonyl)imide) and **PEDOT:PSS** electrode (0.32 mN at 2 V)[34] and zwitterion-doped single-cation conducting block copolymers sandwiched by single-walled carbon nanotube electrodes (0.3 mN at 1 V).[10] It is noteworthy that only a small number of ions confined in the nanoscale space can generate the bending motion and force, which can contribute to reduce the risk of ionic liquid leakage and the production cost.

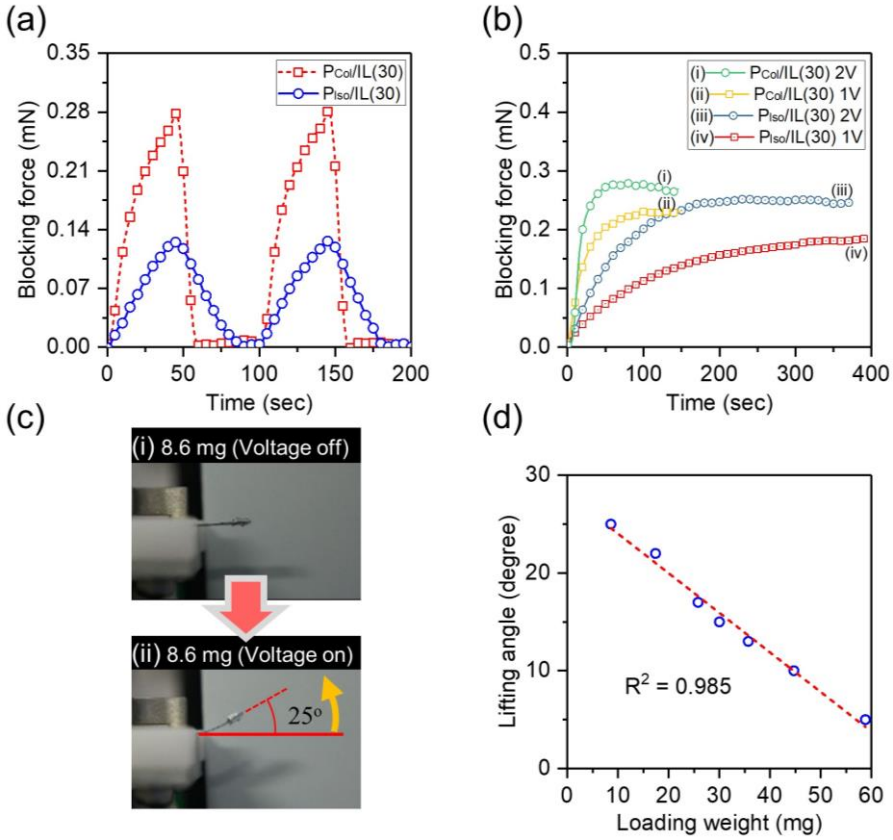

Figure 2.11 Blocking force for the columnar and amorphous polymer actuators under (a) AC voltage of 2 V at 0.01 Hz and (b) DC voltage of 1 and 2 V. (c) Photograph of the columnar polymer actuator lifting 8.6 mg of aluminum foil under DC voltage of 2 V. The dimension of the actuator strip is 12 mm × 4 mm × 61 μm. The weight of actuator is 2.9 mg. (d) Lifting angle of the columnar actuator *vs* loaded weight.

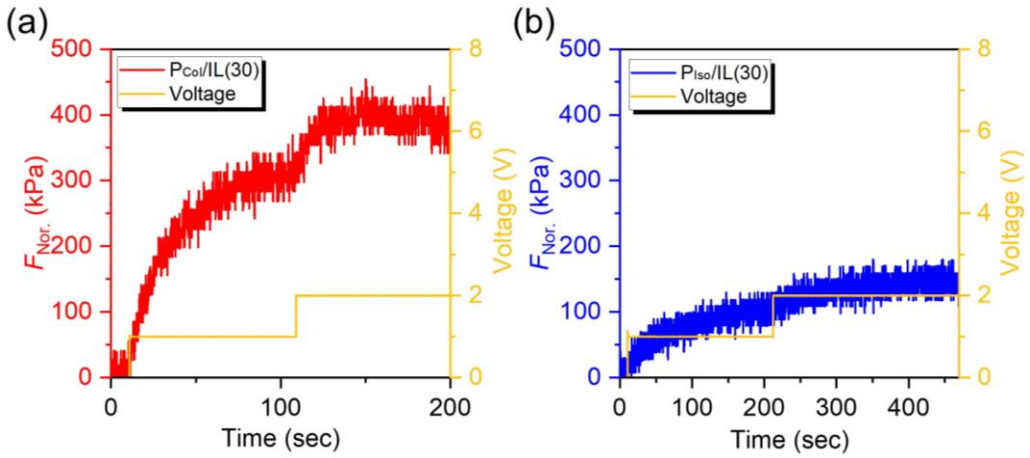

Figure 2.12 Voltage dependence of the normalized blocking force generated by the actuators based on (a) **P_{Col}/IL(30)** and (b) **P_{Iso}/IL(30)**.

2.4 Conclusions.

In summary, I have reported the photo-cross-linked ionic columnar liquid-crystalline polymer films confining ionic liquid into the 1D channels and the first application to electroactive actuators that show low-voltage driven bendability in the air and yield the controlled force generation. I have unveiled the direct correlation between the nanochannels and the actuation performances, in which the columnar LC electrolyte-based actuator exhibits the good performances than isotropic LC electrolyte-based actuator. These results suggest that the construction of 1D ionic channels has a positive impact on the development of ionic actuators. The concept of nanosegregation, consisting of liquid-like ion-conductive and rigid mesogenic domains, may lead to new designs for ionic electroactive actuators to achieve the conflicting functions of high-power generation and fast motion.

2.5 References.

(1) Asaka, K.; Okuzaki, H. *Soft Actuators: Materials, Modeling, Applications, and Future Perspectives*, 2nd ed.; Springer, Singapore, 2019.

(2) Feng, C.; Hemantha Rajapaksha, C. P.; Jákli, A. Ionic Elastomers for Electric Actuators and Sensors. *Engineering* **2021**, *7*, 581–602.

(3) Kim, O.; Kim, S. J.; Park, M. J. Low-Voltage-Driven Soft Actuators. *Chem. Commun.* **2018**, *54*, 4895–4904.

(4) White, T; Long, T. E. Advanced in Polymeric Materials for Electromechanical Devices. *Macromol. Rapid Commun*. **2019**, *40*, 1800521.

(5) Martins, P.; Correia, D. M.; Correia, V.; Lanceros-Mendez, S. Polymer-Based Actuators: Back to the Future. *Phys.Chem.Chem.Phys*. **2020**, *22*, 15163–15182.

(6) Ueki, T.; Watanabe, M. Macromolecules in Ionic Liquids: Progress, Challenges, and Opportunities. *Macromolecules* **2008**, *41*, 3739–3749.

(7) Fukushima, T.; Asaka, K.; Kosaka, A.; Aida, T. Fully Plastic Actuator through Layer-by-Layer Casting with Ionic-Liquid-Based Bucky Gel. *Angew. Chem., Int. Ed. Engl.* **2005**, *44*, 2410–2413.

(8) Duncan, A. J.; Leo, D. J.; Long, T. E. Beyond Nafion: Charged Macromolecules Tailored for Performance as Ionic Polymer Transducers. *Macromolecules* **2008**, *41*, 7765–7775.

(9) Kim, O.; Shin, T. J.; Park, M. J. Fast Low-Voltage Electroactive Actuators Using Nanostructured Polymer Electrolytes. *Nat. Commun*. **2013**, *4*, 2208.

(10) Kim, O.; Kim, H.; Choi, U. H.; Park, M. J. One-Volt-Driven Superfast Polymer Actuators Based on Single-Ion Conductors. *Nat. Commun*. **2016**, *7*, 13576.

(11) Lee, J.-W.; Yu, S.; Hong, S. M.; Koo, C. M. High-Strain Air-Working Soft Transducers Produced from Nanostructured Block Copolymer Ionomer/Silicate/Ionic Liquid Nanocomposite Membranes. *J. Mater. Chem. C* **2013**, *1*, 3784–3793.

(12) Imaizumi, S.; Kokubo, H.; Watanabe, M. Polymer Actuators Using Ion-Gel Electrolytes Prepared by Self-Assembly of ABA-Triblock Copolymers. *Macromolecules* **2012**, *45*, 401–409.

(13) Guo, D.; Han, Y.; Huang, J.; Meng, E.; Zhang, H.; Ding, Y. Hydrophilic Poly(vinylidene Fluoride) Film with Enhanced Inner Channels for Both Water- and Ionic Liquid-Driven Ion-Exchange Polymer Metal Composite Actuators. *ACS Appl. Mater. Interfaces* **2019**, *11*, 2386–2397.

(14) Simaite, A.; Tondu, B.; Souères, P.; Bergaud, C. Hybrid PVDF/PVDF-graft-PEGMA Membranes for Improved Interface Strength and Lifetime of PEDOT:PSS/PVDF/Ionic Liquid Actuators. *ACS Appl. Mater. Interfaces* **2015**, *7*, 19966–19977.

(15) Kim, J.; Jeon, J.-H.; Kim, H.-J.; Lim, H.; Oh, I.-K. Durable and Water-Floatable Ionic Polymer Actuator with Hydrophobic and Asymmetrically Laser-Scribed Reduced Graphene Oxide Paper Electrodes. *ACS Nano* **2014**, *8*, 2986–2997.

(16) Kato, T.; Yoshio, M.; Ichikawa, T.; Soberats, B.; Ohno, H.; Funahashi, M. Transport of Ions and Electrons in Nanostructured Liquid Crystals. *Nat. Rev. Mater.* **2017**, *2*, 17001.

(17) Cho, B.-K. Nanostructured Organic Electrolytes. *RSC Adv.* **2014**, *4*, 395–405.

(18) Kerr, R. L.; Miller, S. A.; Shoemaker, R. K.; Elliott, B. J.; Gin, D. L. New Type of Li Ion Conductor with 3D Interconnected Nanopores via Polymerization of a Liquid Organic Electrolyte-Filled Lyotropic Liquid-Crystal Assembly. *J. Am. Chem. Soc.* **2009**, *131*, 15972–15973.

(19) van Kuringen, H. P.; Eikelboom, G. M.; Shishmanova, I. K.; Broer, D. J.; Schenning, A. P. H. J. Responsive Nanoporous Smectic Liquid Crystal Polymer Networks as Efficient and Selective Adsorbents. *Adv. Funct. Mater.* **2014**, *24*, 5045–5051.

(20) Wang, S.; Liu, X.; Wang, A.; Chen, J.; Zeng, Q.; Wang, X.; Zhang, L. An Ionic Liquid Crystal-Based Solid Polymer Electrolyte with Desirable Ion-Conducting Channels for Superior Performance Ambient-Temperature Lithium Batteries. *Polym. Chem*. **2018**, *9*, 4674–4682.

(21) Feng, C.; Rajapaksha, C. P. H.; Cedillo, J. M.; Piedrahita, C.; Cao, J.; Kaphle, V.; Lüssem, B.; Kyu, T.; Jákli, A. Electroresponsive Ionic Liquid Crystal Elastomers. *Macromol. Rapid Commun.* **2019**, *40*, 1900299.

(22) Yoshio, M.; Kagata, T.; Hoshino, K.; Mukai, T.; Ohno, H.; Kato, T. One-Dimensional Ion-Conductive Polymer Films: Alignment and Fixation of Ionic Channels Formed by Self-Organization of Polymerizable Columnar Liquid Crystals. *J. Am. Chem. Soc.* **2006**, *128*, 5570–5577.

(23) Ichikawa, T.; Yoshio, M.; Hamasaki, A.; Kagimoto, J.; Ohno, H.; Kato, T. 3D Interconnected Ionic Nano-Channels Formed in Polymer Films: Self-Organization and Polymerization of Thermotropic Bicontinuous Cubic Liquid Crystals. *J. Am. Chem. Soc.* **2011**, *133*, 2163–2169.

(24) Gin, D. L.; Bara, J. E.; Noble, R. D.; Elliott, B. J. Polymerized Lyotropic Liquid Crystal Assemblies for Membrane Applications. *Macromol. Rapid Commun*. **2008**, *29*, 367–389.
(25) Lugger, J.; Mulder, D. J.; Sijbesma, R.; Schenning, A. Nanoporous Polymers Based on Liquid Crystals. *Materials* **2018**, *11*, 104.
(26) Sakamoto, T.; Ogawa, T.; Noda, H.; Nakatsuji, K.; Mitani, M.; Soberats, B.; Kawata, K.; Yoshio, M.; Tomioka, H.; Sasaki, T.; Kimura, M.; Henmi, M.; Kato, T. Development of Nanostructured Water Treatment Membranes Based on Thermotropic Liquid Crystals: Molecular Design of Sub-Nanoporous Materials. *Adv. Sci*. **2017**, *5*, 1700405.
(27) Takeuchia, I.; Asaka, K.; Kiyoharaa, K.; Suginoa, T.; Terasawa, N.; Mukai, K.; Fukushima, T.; Aida, T. Electromechanical Behavior of Fully Plastic Actuators based on Bucky Gel Containing Various Internal Ionic Liquids. *Electrochim. Acta* **2009**, *54*, 1762–1768.
(28) Ue, M.; Murakami, A.; Nakamura, S. A Convenient Method to Estimate Ion Size for Electrolyte Materials Design. *J. Electrochem. Soc.* **2002**, *149*, A1385–A1388.
(29) Hagiwara, R.; Lee, J. S. Ionic Liquids for Electrochemical Devices. *Electrochemistry* **2007**, *75*, 23–34.
(30) Noda, A.; Hayamizu, K.; Watanabe, M. Pulsed-Gradient Spin–Echo ^{1}H and ^{19}F NMR Ionic Diffusion Coefficient, Viscosity, and Ionic Conductivity of Non-Chloroaluminate Room-Temperature Ionic Liquids. *J. Phys. Chem. B* **2001**, *105*, 4603–4610.
(31) Hayamizu, K.; Aihara, Y.; Nakagawa, H.; Nukuda, T.; Price, W. Ionic Conduction and Ion Diffusion in Binary Room-Temperature Ionic Liquids Composed of [emim][BF_4] and $LiBF_4$. *J. Phys. Chem. B* **2004**, *108*, 19527–19532.
(32) Mukai, K.; Asaka, K.; Sugino, T.; Kiyohara, K.; Takeuchi, I.; Terasawa, N.; Futaba, D. N.; Hata, K.; Fukushima, T.; Aida, T. Highly Conductive Sheets from Millimeter-Long Single-Walled Carbon Nanotubes and Ionic Liquids: Application to Fast-Moving, Low-Voltage Electromechanical Actuators Operable in Air. *Adv. Mater.* **2009**, *21*, 1582–1585.
(33) Nemat-Nasser, S; Wu, Y. Comparative Experimental Study of Ionic Polymer-Metal Composites with Different Backbone Ionomers and in Various Cation Forms. *J. Appl. Phys.* **2003**, *93*, 5255–5267.
(34) Kim, S. Y.; Kim, Y.; Cho, C.; Choi, H.; Park, H. W.; Lee, D.; Heo, E.; Park, S.; Lee, K.; Kim, D. H. Deformable Ionic Polymer Artificial Mechanotransducer with an Interpenetrating Nanofibrillar Network. *ACS Appl. Mater. Interfaces* **2019**, *11*, 29350–29359.

Chapter 3

Liquid Crystal Self-Assembly of a Biomolecular Itaconate Ionic Amphiphile in an Ionic Liquid: Enhancement of Actuation by Uniformly Oriented Layered Ion Transport Pathways

3.1 Introduction.

Electrically-driven polymer actuators are essential components in the development of soft robotic and haptic technologies.[1–6] Ionic polymer actuators, which display significant deformation due to ion diffusion, are among the most promising candidates for such applications.[7] This is due to their low-operation voltage less than 2 V, easy processability, and lightness.[8] However, actuators that can simultaneously achieve both large deformation and high force output are relatively rare. Nanostructured polymer electrolytes[9–11] have emerged as a promising alternative to conventional amorphous electrolytes, such as ionic liquid-containing polymer gels[12–18] and lithium-ion/poly(ethylene glycol) complexes[19–21] for improving device performance. Recent successful examples include ionic covalent organic frameworks,[22] block copolymers,[10,11,23] and nanophase-segregated liquid-crystalline (LC) polymers,[24] which promote fast ion transport, resulting in fast frequency response and increased actuator force. The use of liquid crystal assembly offers numerous benefits, particularly in terms of the ease of macroscopic alignment of ion pathways.[25,26] In my recent report, I discussed the development of ionic actuators composed of photopolymerized ionic columnar liquid crystals and conductive polymer electrodes made of poly(3,4–ethylene dioxythiophene):poly(styrenesulfonic acid) (**PEDOT:PSS**).[27,28] These innovative actuators exhibit larger strain and higher force, despite having a lower ion content compared to conventional gel electrolytes. However, achieving a vertically oriented ion-transport pathway across photocured polymer electrolyte film, which would provide ideal device performance, remains as a significant challenge. This underscores the fundamental importance of developing new strategies for designing polymer electrolytes. To address this challenge, I propose a novel approach based on the use of a polymerizable ionic amphiphile derived from biomolecular itaconate. By harnessing its liquid crystal self-assembly in ionic liquids, I aim to design nanostructured electrolytes with layer, columnar, and bicontinuous cubic phases.

Herein, I present a new lyotropic LC assembly of reactive, biomolecular itaconate-based ionic amphiphile **It** and 1–ethyl–3–methylimidazolium tetrafluoroborate **IL** into the smectic (Sm), bicontinuous cubic (Cub_{bi}), and hexagonal columnar (Col_h) structures (**Figure 3.1**). UV irradiation was able to retain each nanostructure in the solid polymer

film, but the resulting films were weak. To produce LC polymer films with mechanical strength that can withstand actuator fabrication and its evaluation, the lyotropic LC monomer **It** was copolymerized with poly(ethylene glycol) diacrylate. Tough polymer films with layered nanostructures were successfully obtained. Ionic electroactive actuators based on the LC polymer electrolytes with vertically aligned layers to the film surface have been demonstrated for the first time. The uniform orientation of layered ion transport pathways over large areas has been achieved by applying mechanical shear force to the non-polymerized LC sample sandwiched between glass substrates. The oriented ion pathways can greatly enhance ion migration, which resulted in large bending strain (0.8 % at 0.01 Hz, 2 V) and high blocking force (0.7 mN, at 0.1 Hz, 2 V) for the actuators. Each of these properties is superior to other ionic liquid-based actuators including block polymers and polyimides and is comparable to my recent columnar LC polymer actuator with 3D ion-transport pathways.[28] In addition, I have observed the biodegradability of the nanostructured polymer electrolyte film. This sustainable design of polymerizable liquid crystals using itaconate offers exciting opportunities for electromechanical energy conversion in the development of next-generation soft robotic and haptic technologies.

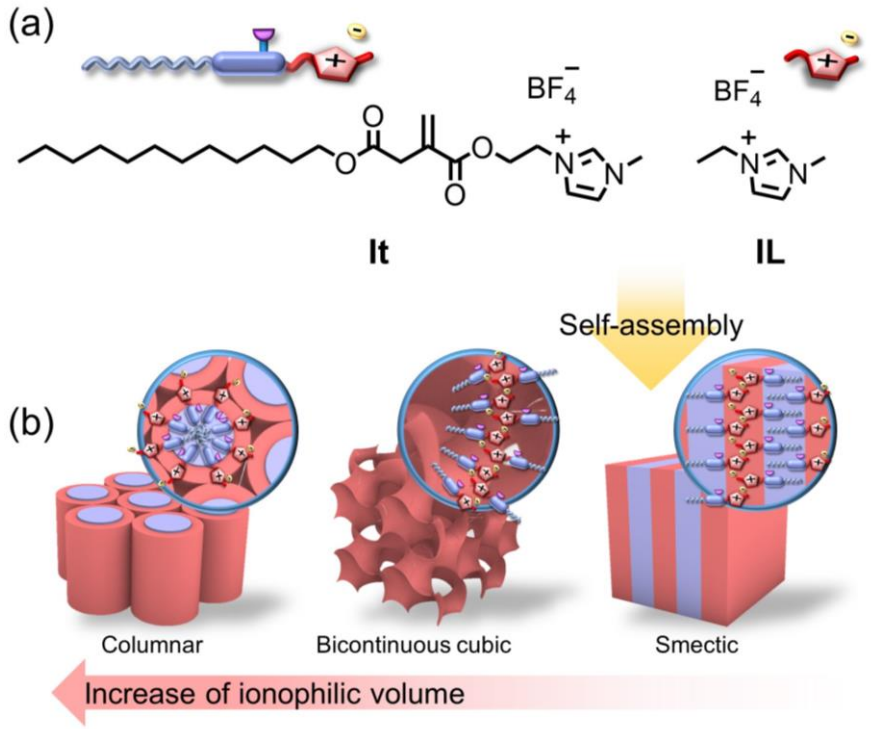

Figure 3.1 (a) Molecular structures of polymerizable ionic liquid-crystalline itaconate (**It**) and ionic liquid (**IL**). (b) Self-assembly of the binary mixtures into nanosegregated LC structures consisting of ionophilic and ionophobic parts which are shown in red and blue, respectively: from smectic (Sm) to bicontinuous cubic (Cub_{bi}) and hexagonal columnar (Col_h) assembled structures with increasing **IL** content.

3.2 Experimental Section.

3.2.1 Materials.

Itaconic anhydride (>95%), 1–Dodecanol (>99%), 4–Dimethylaminopyridine (DMAP, >99%), *N,N*–Dicyclohexylcarbodiimide (DCC, >98%), 1–Ethyl–3–methylimidazolium tetrafluoroborate (**IL**, >99%), 1–(2–Hydroxyethyl)–3–methylimidazolium tetrafluoroborate (>98%) were purchased from Tokyo chemical industry. Ethylene glycol were purchased from KANTO CHEMICAL. Poly(3,4–ethylene dioxythiophene) polystyrene sulfonate **PEDOT:PSS** (Clevios™ PH1000) was purchased from Heraeus. 2,2–Dimethoxy–2–phenylacetophenone as a photo-initiator was purchased from Sigma-Aldrich. All the chemicals were used directly without further purification.

3.2.2 Synthesis of ionic molecule.

The detailed synthetic route, procedures, and their nuclear magnetic resonance (NMR) spectra were written in ***Appendix 7.2***.

3.2.3 General methods.

Polarized optical microscopy (POM) observations, differential scanning calorimetry (DSC) measurements, X-ray diffraction (XRD) measurements, cyclic voltammetry (CV) measurements, ionic conductivity measurements, and actuation tests were performed using the same equipment and methods as described in the previous Chapter. Rheological measurements were performed using an Anton Paar MCR 102 rheometer (Anton Paar, Austria). A parallel plate geometry with an 8 mm diameter plate and a gap spacing of 0.3 mm were used for all the measurements. The measurements were conducted at an angular frequency of 10 rad s^{-1} and a shear strain amplitude of 0.01%-1000%. The SEM observation was performed using a Hitachi S-4800 field-emission scanning electron microscope operating at 3 kV.

3.2.4 Bio-degradation test.

An itaconate LC film $\mathbf{P_{It}}$ with the dimension of 8 mm × 6 mm × 60 μm was used to perform soil burial experiments. The film was buried 5 mm deep in normal garden soil (weight: 1 g) placed in a glass cell-culture dish with a diameter of 4 cm. The setup was kept at room temperature (23 ± 2 °C) and an average relative humidity of (30 ± 5)%, and

the soil was regularly watered to maintain moisture. Biodegradation was verified through observations of the film's appearance, both longitudinally and cross-sectionally, using POM and SEM analyses.

3.2.5 Fabrication of liquid-crystalline actuators.

The mixture of ionic molecule **It** and the [EMIM][BF_4] ionic liquid (**IL**) at the 7:3 molar ratio with 2.5 wt% of cross-linker polyethylene glycol diacrylate (PEGDA 400) and 1 wt% of photo-initiator (2,2–dimethoxy–2–phenylacetophenone) were dissolved in a mixed solution of chloroform/methanol (4/1 by volume), and the solvents were removed in a rotary evaporator under light–resistant condition. The monomeric sample **It/IL(30)** containing PEGDA was placed between an untreated cover glass and a glass substrate covered with a polyimide (PI). The sandwiched cell was heated to a temperature at which the sample became the isotropic liquid state and then cooled to room temperature at a rate of 1 ºC/min to form a randomly orientation liquid-crystalline nanostructure. Subsequently, the cell was irradiated with UV light (350 nm, 10 mW/cm^2) for 5 minutes at room temperature. After polymerization, the $\mathbf{P_{It}}$ film was carefully peeled off from the substrate. The $\mathbf{P_{It}}$ film was sandwiched between two **PEDOT:PSS** sheets and pressed. The tri-layered composite was cut into rectangular shape that were used as $\mathbf{P_{It}}$-based actuator. The uniaxially parallel aligned nanostructure film, $\mathbf{P_{It(//)}}$ was prepared from the macroscopically aligned by shearing them parallel to the glass substrate and subsequent polymerization.

3.3 Results and Discussion.

3.3.1 Liquid crystal self-assembly of It and IL.

The design of new, sustainable, and environmentally benign synthetic polymers is crucial towards meeting the goals of economic growth and environmental protection. I focus on the use of biomolecular itaconate as a photopolymerizable monomer. The new designed ionic itaconate derivative **It** was synthesized by the ring-opening addition reaction of itaconate anhydride with 1–dodecanol, followed by esterification of the carboxylic acid group with a commercially available 1–(2–hydroxyethyl)–3–methylimidazolium tetrafluoroborate.

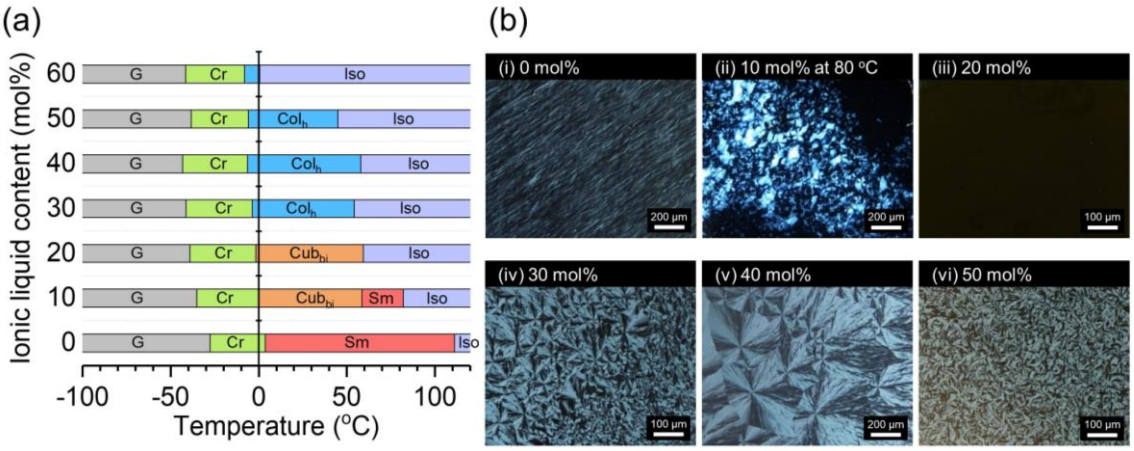

Figure 3.2 (a) Phase transition behavior of **It** and the mixtures of **It** and **IL** (**It/IL(x)**, x = 10-60 mol%) on heating as a function of the mole% of **IL**. The transition temperatures were taken at the peak top of the second heating DSC curve. G, Cr, Sm, Cub_{bi}, Col_h, and Iso are glassy, crystal, smectic, bicontinuous cubic, hexagonal columnar, and isotropic liquid phases, respectively. (b) Polarized optical micrographs (POM) of (i) **It** and (ii–vi) the mixtures of **It** and **IL** in different molar ratios. The POM images were taken at room temperature, except for (ii) **It/IL(10)** at 80 °C.

LC properties of **It** and the mixtures of **It** and **IL** were characterized by differential scanning calorimetry (DSC) and X-ray diffraction (XRD) measurements and polarized optical microscopic (POM) observation. Compound **It** alone exhibits a thermotropic smectic A (Sm) phase in a wide range of temperatures from 3.6 to 111 °C (**Figure 3.2 (a)**). The POM image of **It** at room temperature shows an oily streak texture (**(i) in Figure 3.2**

(b)). The XRD pattern of **It** at room temperature (**Figure 3.3 (a)**) presents three peaks at 35.2, 17.7, and 11.8 Å with a reciprocal *d*-spacing ratio of 1 : 2 : 3 , which can be indexed to the (001), (002), and (003) reflections from a layered smectic A phase with an interlayer distance of 35 Å. The estimated molecular length of **It** with the extended conformation is 24.8 Å (**Figure 3.3 (b)**). From the results of XRD measurement and calculation, the Sm phase is expected to form an interdigitated bilayer packing of **It**, consisting of an imidazolium ionic layer and a hydrophobic alkyl chain layer.

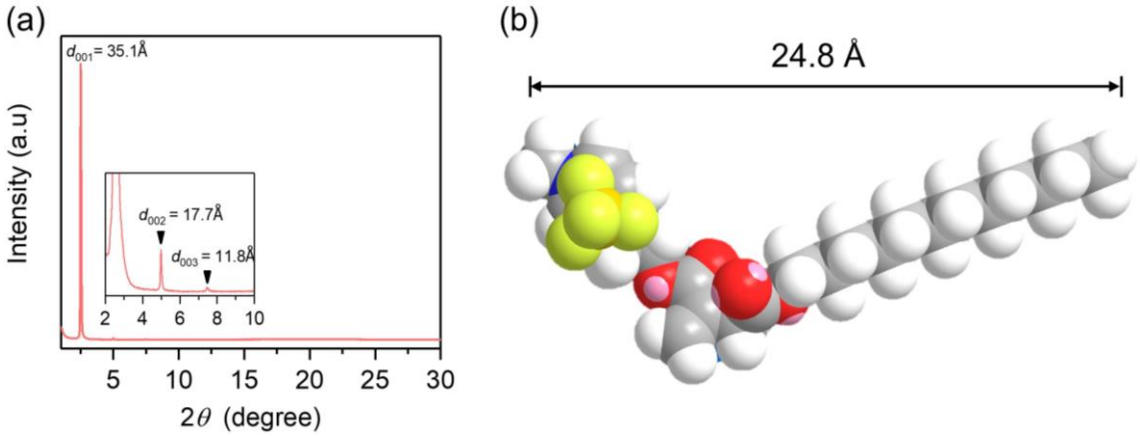

Figure 3.3 (a) XRD pattern of **It** at room temperature. (b) Molecular structure of **It** calculated by density functional theory.

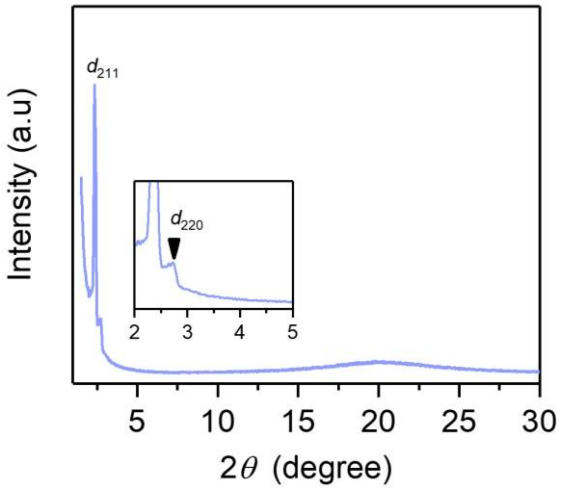

Figure 3.4 XRD pattern of binary mixture **It/IL(20)** at room temperature.

The mixtures of **It** and **IL** (**It/IL(x)**, where **x** denotes the mol% of **IL**) exhibit room-temperature Cub_{bi} and Col_h phases as illustrated in **Figure 3.1** were obtained as homogeneous viscous solids after evaporation of the mixed chloroform/methanol solution (4/1 by volume) containing the requisite amounts of **It** and **IL**. The phase transition behavior of the mixtures up to 60 mol% of **IL** is shown in **Figure 3.2 (a)**. I have found that mixtures **It/IL(10)** and **It/IL(20)** exhibit Cub_{bi} phases with *Ia3d* symmetry and the mixtures containing 30-60 mol% of **IL** form Col_h phases. It is noteworthy that the self-organized structure of ions at room temperature is easily controlled by changing the mixing ratio of **It** and **IL** in the absence of water.

The isotropization temperature decreases with increasing **IL** in the mixture. Mixture **It/IL(20)** exhibits only a Cub_{bi} LC phase between -1.7 and 59.4 ºC, while **It/IL(10)** shows a Cub_{bi} phase between 0 and 58 °C and an Sm phase up to 81 °C. These Cub_{bi} phases show no birefringence under POM observation, as shown in **Figure 3.2 (b) (iii)**. The XRD pattern of **It/IL(20)** shows two peaks at 37.6 and 32.2 Å with a reciprocal *d*-spacing ratio of √6 and √8, which can be assigned to the (211) and (220) reflections of a normal gyroid Cub_{bi} phase with *Ia3d* symmetry (**Figure 3.4**). The normal Cub_{bi} phase is thought to be consisted of two interwoven, non-intersecting hydrophobic networks separated by a continuous ionic layer surface in three directions. Prof. Kato groups previously reported the first example of thermotropic, reverse *Ia3d* Cub_{bi} phase of taper-shaped molecules containing ammonium and phosphonium moieties as ion conductors.[30,31] It has been found that the cubic phase provides 3D interconnected ionic channels that do not require alignment for optimal transport. Since the normal Cub_{bi} phase is inherently considered to form a larger 3D continuous ionic surface than the inverse Cub_{bi} phase, photopolymerization of **It/IL(10)** and **It/IL(20)** in the normal Cub_{bi} phases is expected to result in polymer electrolytes that exhibit superior transport properties without the need for alignment. The development of Cub_{bi} LC materials for separations and electrolytes for devices is one of the active areas in advanced science.[32]

On the other hand, the hexagonal ordering of nanosegregated columns consisting of ionophobic cylinders surrounded by ionic shells are also promising electrolytes for ionic electroactive actuators, because ions could jump from one column to the other even if the columns are randomly oriented.[28] The formation and temperature range of Col_h phase for

the mixtures containing 30-60 mol% of **IL** was determined by the combined results of POM observations, XRD measurements (**Figure 3.5**), DSC, and isotropic ionic conductivity independent on the columnar alignment, which are discussed later. For example, **It/IL(40)** exhibits a Col_h phase between -6 and 58 °C, while the Col_h phase of **It/IL(30)** was observed between -3.6 and 54 °C. Further addition of **IL** resulted in the destabilization of the Col_h phase. The POM image of **It/IL(30)** shows a fan-shaped texture typical for a Col_h phase (**Figure 3.2 (b), (iv)**). The XRD pattern of **It/IL(30)** at 25 °C shows three peaks at 38.7, 22.2, 19.5 Å with the reciprocal *d*-spacing ratio of 1 : √3 : 2 reflections, which can be indexed as the (100), (110), and (200) reflections of the columns with hexagonal lattice (**Figure 3.5**).

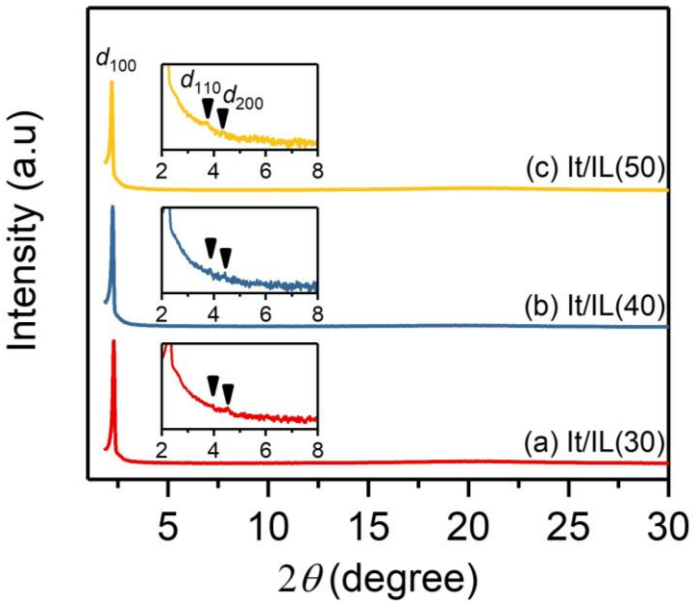

Figure 3.5 XRD pattern of (a) **It/IL(30)**, (b) **It/IL(40)**, and (c) **It/IL(50)** at room temperature.

Ionic electroactive actuation behaviours are believed to be highly dependent on the mechanical and ion-conductive properties of polymer electrolytes. The viscoelasticity of non-polymerized samples (**It** in the Sm phase, **It/IL(20)** in the Cub_{bi} phase, and **It/IL(30)** in the Col_h phase at room temperature) was measured as a function of strain at a constant frequency to understand the effect of assembled structures on their strength (**Figure 3.6**). In the low-strain linear viscoelastic region until 1% strain, the G' (storage modulus) values are higher than the G'' (loss modulus) values. The Cub_{bi} sample has been found to exhibit the highest G' (storage modulus) value of about 10^6 Pa. The G' value is

comparable to that of aqueous lyotropic Cub_{bi} liquid crystals[33,34] and supramolecular hydrogels.[35,36] In addition, the G' value of the Col_h phase (~10^5 Pa) was higher than that of the Sm phase (~10^3 Pa). It is well known that **IL** can acts as a plasticizer for polymers. In the present study, however, the viscoelasticity of **It** increased upon the addition of **IL**. This result suggests that **IL** is not randomly dispersed into the mixtures, but is organized into the nanosegregated ionophilic domains through electrostatic and hydrogen bonding interactions between the cation and anion. By further increase of the shear strain over 6%, the values of G' dropped at a critical yield strain, followed by a crossover of G' and G''. The G'' > G' suggests a change from the elastic solid-like behaviour to a liquid-like behaviour.

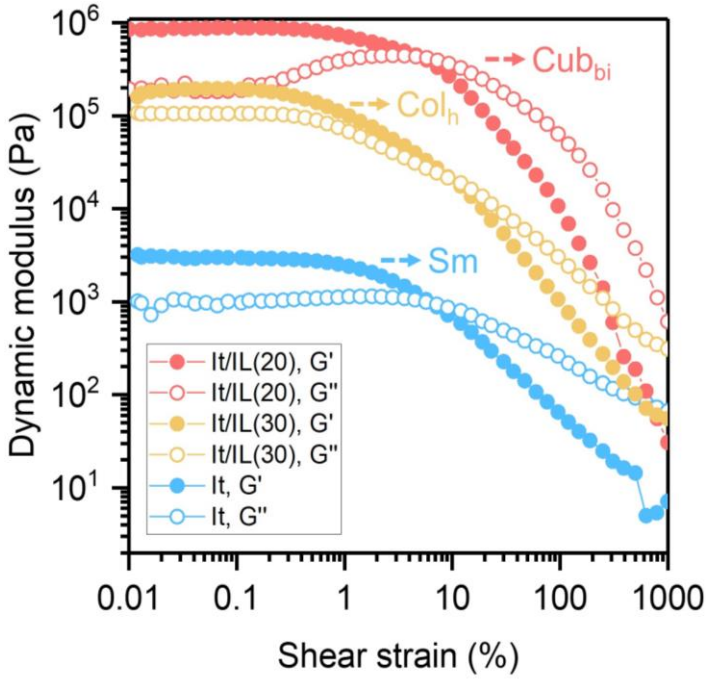

Figure 3.6 The storage (G', filled) and loss (G", open) moduli as a function of % strain at an angular frequency of 10 rad s^{-1} for **It** (Sm phase, blue), **It/IL(20)** (Cub_{bi} phase, red), and **It/IL(30)** (Col_h phase, orange) at room temperature.

3.3.2 Ion-conductive properties of non-polymerized LC samples.

To apply these LC materials as novel ion conductors, I conducted the ionic conductivity measurement as a function of temperature, as shown in **Figure 3.7**. Compound **It** has an ionic conductivity of 1.2×10^{-5} S/cm in the Sm phase at 25 °C. The ionic conductivities show an Arrhenius temperature dependence. The activation energy of **It** in the Sm phase was estimated to be 51 kJ/mol. Upon the introduction of **IL**, the ionic conductivity is drastically increased, and the activation energy is significantly decreased. The Cub_{bi} phase for **It/IL(20)** shows the conductivity of 2×10^{-4} S/cm at room temperature. The maximum room-temperature conductivity of 5×10^{-4} S/cm is achieved for **It/IL(40)** in the Col_h phase and the estimated activation energy is about 23 kJ/mol. These high conductivities in the Cub_{bi} and Col_h phases at room temperature have never been achieved for non-aqueous LC systems. For example, I recently reported that the Col_h phase formed by binary mixtures of polymerizable wedge-shaped ionic molecules and **IL** showed the conductivity of 5.4×10^{-5} S/cm, which is one order of magnitude lower than that obtained in this work.[28] A simple molecular design of reducing the number of insulating alkyl moieties should play an essential key to improving the conductivity.

As for **It/IL(10)**, a drop in conductivity at the Cub_{bi}-Sm phase transition around 55 °C has been observed (**Figure 3.7, orange circle**). The POM observation reveals that the Cub_{bi} phase is gradually changed to the randomly oriented Sm phase upon heating. Therefore, this drop in conductivity at the phase transition suggests that the 3D interconnected ion pathways formed in the Cub_{bi} phase facilitates ion transport compared to the Sm phase, in which the polydomain boundaries may disturb ion transport.

For anisotropic ionic conductivity measurements (**Figure 3.8**), the self-organized Col_h structures for the mixtures containing 30-50 mol% **IL** were sheared and aligned macroscopically between comb-shaped gold electrodes on a glass substrate in a direction parallel and perpendicular to the electric field. The ionic conductivities of the polydomain sample with preferentially vertical orientation and the shear-aligned samples with planar orientation are nearly identical. The observed isotropic conductivity regardless of the differences in the alignment suggests that a continuous 3D ionic pathway is formed on the outside of the lipophilic cylinders, as schematically illustrated in **Figure 3.8 (b)**.

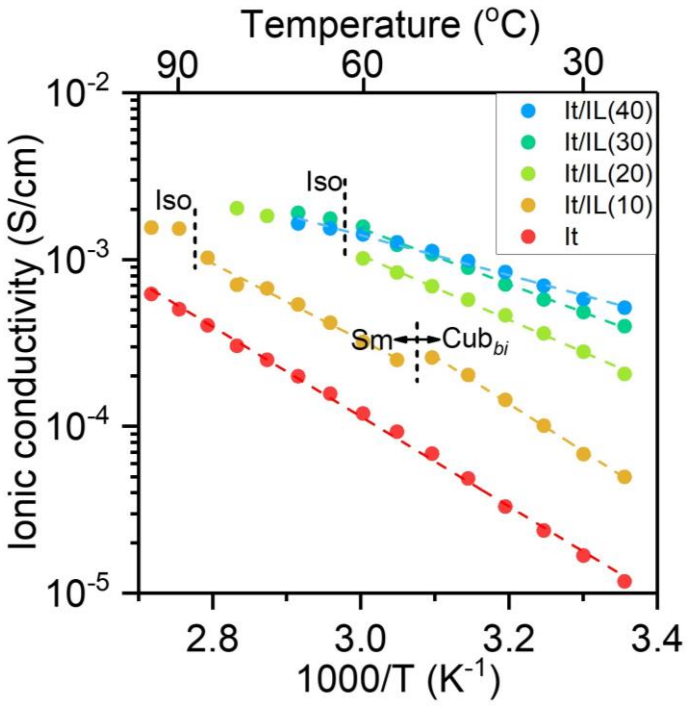

Figure 3.7 Temperature dependence of ionic conductivity for **It/IL(x)** with **x** = 0-40 mol% of **IL** on heating.

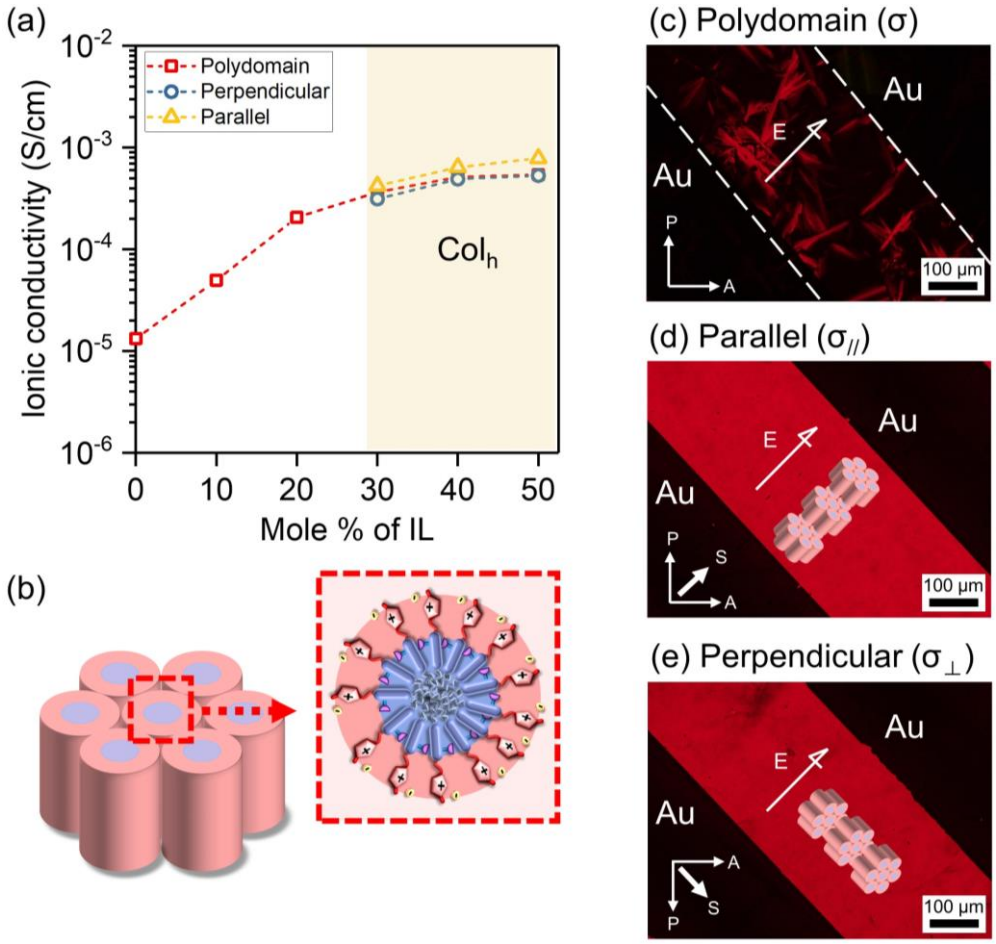

Figure 3.8 (a) Ionic conductivities of compound **It** as a function of the mole% of **IL**. The yellow area shows the ionic conductivity for the oriented columns (△: parallel and ○: perpendicular to the applied electric field and randomly oriented columns (□). (b) The image illustrated the Col_h LC structure form by the hydrophobic cylinders surrounded by ionic shells. POM images for different orientations of the columns: (c) the columns are randomly oriented between electrodes, (d) the columns are aligned by shearing to the direction of electric field, and (e) the columns are aligned perpendicular to the electric field by shearing. Arrows indicate the directions of the mechanical shear force (*S*), analyzer (*A*), polarizer (*P*), and electric field (*E*).

3.3.3 In-situ photopolymerization of the LC mixtures.

Polyethylene glycol diacrylate (PEGDA 400) was selected as a cross-linking agent that reacts with the vinyl group of **It** and can bridge between nanophase-separated hydrophobic domains without interfering with ionic conduction pathways, but rather accelerating them. After optimizing the concentration, 2.5 wt% PEGDA 400 to **It/IL(x)** was found to be sufficient to obtain mechanically tough free-standing polymer films. However, the addition of polar PEGDA 400 to **It/IL(x)** resulted in the formation of Sm phases.

Among them, *In-situ* photopolymerization of **It/IL(30)** containing 2.5 wt% PEGDA 400 in the Sm phase at room temperature produced a layered nanostructured polymer film (**Figure 3.9 (b), inset**) with good mechanical strength that could withstand actuator fabrication and high room-temperature ionic conductivity of 3.6×10^{-5} S/cm in randomly oriented layered domains. It should be noted that polymerization does not significantly reduce the conductivity. Hereafter, this film is denoted as $\mathbf{P_{It}}$.

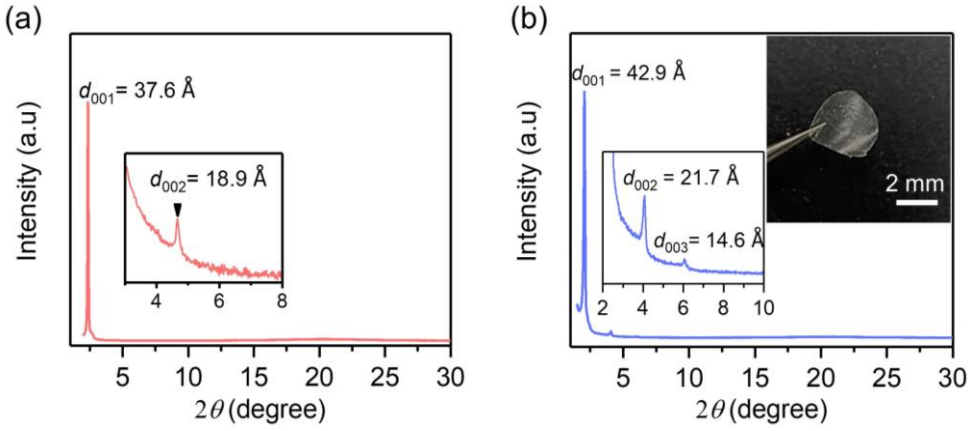

Figure 3.9 XRD patterns of (a) monomeric mixture **It/IL(30)** containing 2.5 wt% PEGDA 400 at 25 °C. The inset indicates the magnified image of the selected region, and (b) $\mathbf{P_{It}}$ film obtained after UV polymerization of **It/IL(30)** containing 2.5 wt% of PEGDA 400 at room temperature. The inset shows its appearance.

The XRD pattern of $\mathbf{P_{It}}$ shows three peaks at 42.9, 21.7, and 14.6 Å with a reciprocal *d*-spacing ratio of 1 : 2 : 3 (**Figure 3.9 (b)**). The estimated interlayer distance of $\mathbf{P_{It}}$ is 43 Å. In contrast, the monomer shows two peaks at 37.6 and 18.9

Å corresponding to (001) and (002) reflections, respectively (**Figure 3.9**) and the layer distance is about 38 Å. It was found that polymerization increases the periodicity of the layered structure and widens the interlayer distance.

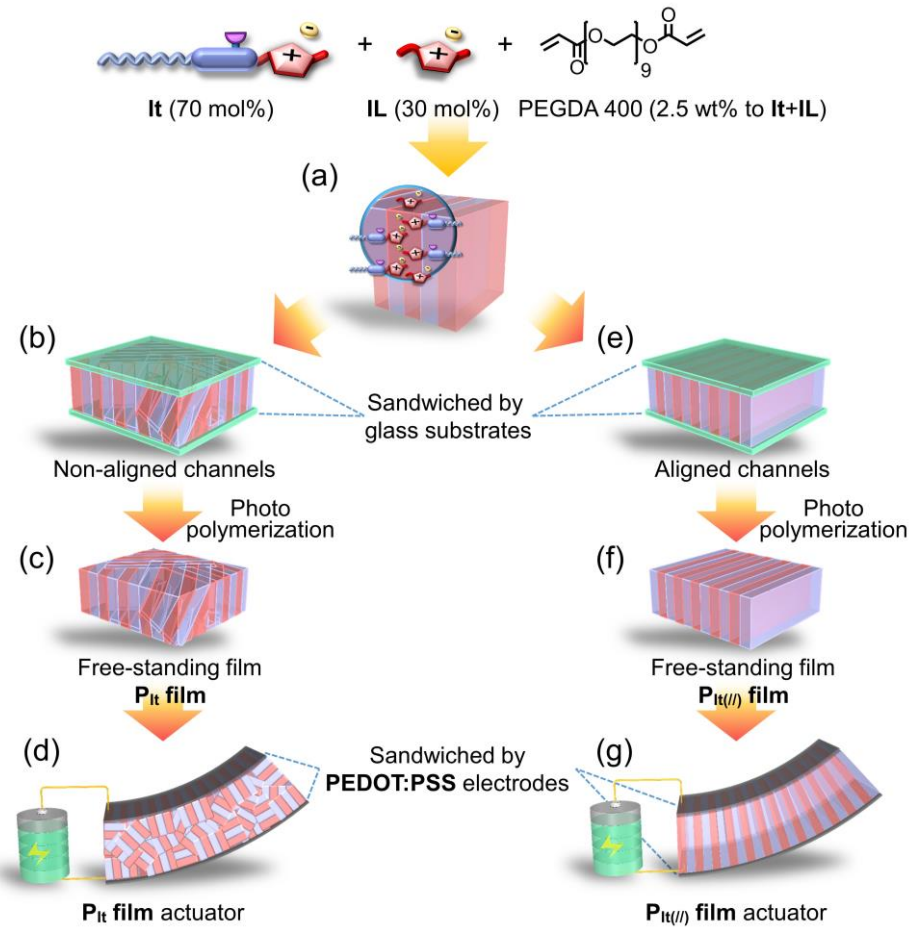

Figure 3.10 Schematic illustration of (a) a layered self-assembly of **It/IL(30)** containing a crosslinker and a fabrication of ion-conductive polymer films and actuators with 2D ion-transport pathways that is randomly oriented (b-d) and vertically oriented (e-g) to the surface of polymer electrolyte. Macroscopic alignment of the LC sample was achieved by mechanical shearing.

The macroscopic arrangement of layered ion pathways in the polymer film may affect not only the conductive and mechanical properties, but also the actuation performance. I have prepared two types of polymer films: $\mathbf{P_{It}}$ with randomly oriented ion pathways and $\mathbf{P_{It(//)}}$ with oriented ion pathways perpendicular to the film surface, as shown in **Figure 3.10**. Uniform horizontal

orientation of the layered assemblies within sandwiched glass plates, *i.e.*, vertical orientation of the ion conduction pathways to the LC film surface, was achieved by applying mechanical shear force to the sample in the Sm phase with polydomain structure. POM observation reveals that the layered molecules tend to align parallel to the shearing direction. As shown in **Figure 3.11**, the birefringence of the oriented sample of **It/IL(30)** and the photocured sample (**$P_{It(//)}$**) alternately changes from dark to light upon a 45° rotation under the crossed polarizers. The ionic conductivity of **$P_{It(//)}$** from 25 to 100 °C is slightly increased compared to **P_{It}** (**Figure 3.12**). The room-temperature conductivity of **$P_{It(//)}$** is 4.1×10^{-5} S/cm. In addition, the Young's modulus of **$P_{It(//)}$** is 1.5 times greater than that of **P_{It}** (**Figure 3.13**).

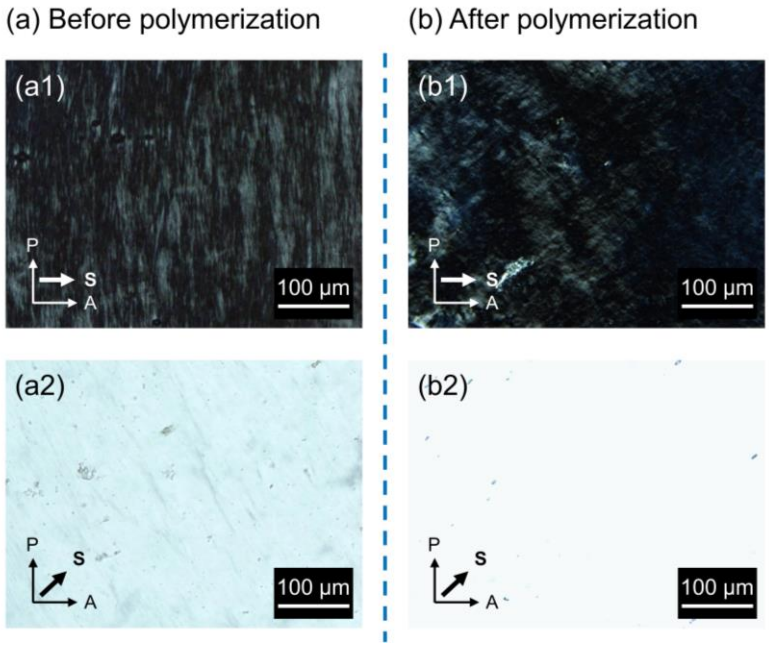

Figure 3.11 POM images of (a) the uniaxially oriented **It/IL(30)** containing 2.5 wt% PEGDA 400 in the Sm phase at room temperature by means of mechanical shearing and (b) after polymerization. Arrows indicate the directions of the mechanical shear force (*S*), polarizer (*P*) and analyzer (*A*). Rotating the sample by 45° produces periodic (a1,b1) dark and (a2,b2) bright images under the crossed Nicols condition.

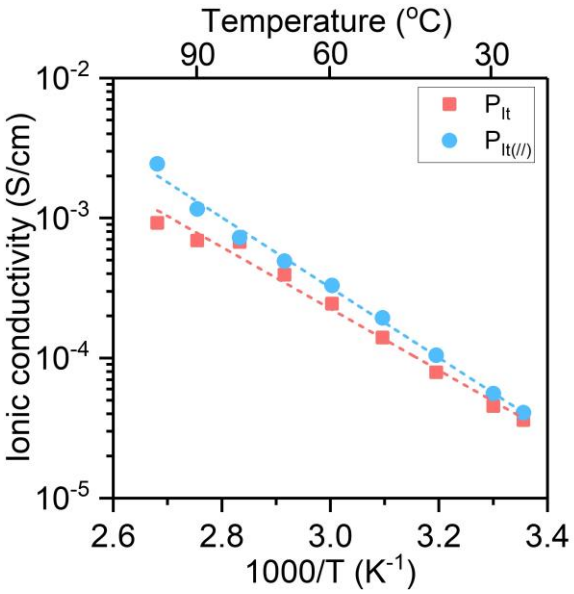

Figure 3.12 Temperature dependence of ionic conductivity for randomly aligned polymer film (**P_{It}**) and vertical aligned polymer film (**$P_{It(//)}$**).

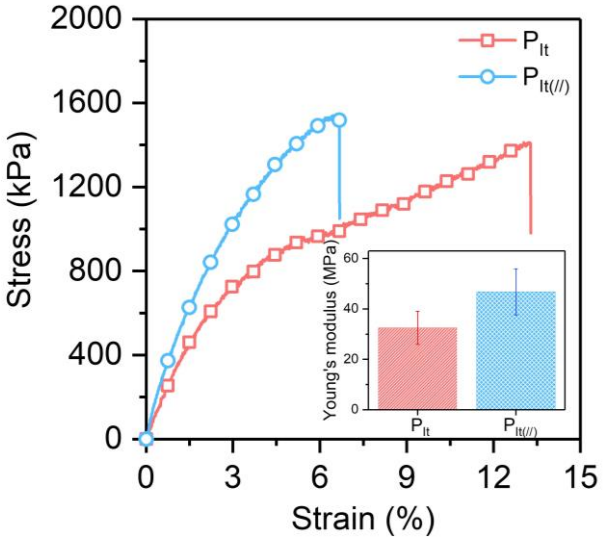

Figure 3.13 Tensile stress-strain curve of **P_{It}** and **$P_{It(//)}$** films. The insert shows the corresponding Young's modulus.

3.3.4 Characterization of ionic electroactive actuators with layered LC polymer electrolytes.

The layered LC polymer film electrolytes $\mathbf{P_{It}}$ and $\mathbf{P_{It(//)}}$ were sandwiched by a pair of free-standing conductive **PEDOT:PSS** electrodes (ca. 500 S/cm) and pressed them at room temperature (**Figure 3.10, panes (d) and (g)**). The electrodes are well adhered to the surface of polymer electrolytes and no delamination of electrodes was observed during long-term actuation experiment. The dimensions of the actuator is 17 mm in length, 4 mm in width, and 50 μm in thickness (electrolyte thickness: 40 μm, PEDOT:PSS thickness: 10 μm).

Figure 3.14 (a) shows a photograph of bending actuator based on $\mathbf{P_{It(//)}}$ under applying an alternating current (AC) voltage of 2 V at 0.1 Hz. The actuator bended toward the positively polarized anodic side. The maximum peak-to-peak bending displacement at the tip is 12 mm. To evaluate the actuation performance by normalized the sample dimension, the peak-to-peak bending strain (%) is calculated by the following equation: $\varepsilon = 2\delta d \times 100/(\delta^2 + L^2)$, where δ is the peak-to-peak displacement, d is the total thickness and L is the free length of the actuator. The $\mathbf{P_{It}}$-based actuator responds in the frequency range of 0.01-20 Hz at 2 V. Bending strain decreased with increasing frequency. For example, the bending strain at 0.01 Hz is 0.5 %, while the strain at 0.1 Hz is 0.2 %. These strain values are calculated from the displacement measured by a laser displacement meter at 7 mm from the clamped end of the actuator strip.

Interestingly, I found that bending strain can be improved by using the macroscopically oriented polymer electrolyte $\mathbf{P_{It(//)}}$. The bending strain of $\mathbf{P_{It(//)}}$ at 0.01 Hz, 2 V is 0.8 %, which is 1.6 times larger than that of $\mathbf{P_{It}}$-based actuator (**Figure 3.14 (b)**). Cyclic voltammetry measurements of these actuators exhibit electrical double-layer capacitance behaviors in a potential window of ± 1 V with scan rates of 10-50 mV/s (**Figure 3.15**). $\mathbf{P_{It(//)}}$-based actuator was found to show higher specific capacitance than $\mathbf{P_{It}}$-based actuator (**Figure 3.14 (c)**), despite the same ion content in the polymer electrolyte. This result suggests that the dissociated ions can efficiently pass through the oriented ion pathways and accumulated on the electrode surfaces. The newly developed layered polyelectrolytes exhibit combined features of easy alignment and high conductivity, in comparison to 1D ion conductive columnar LC polymer films,[27] giving

them a greater advantage in the development of ionic conductors. **PIt(//)**-based actuator also displays good durability of only 10 % strain degradation after 14,000 cyclic operation.

Furthermore, I found that **PIt(//)**-based actuator can generate larger bending forces than **PIt**-based actuator (**Figure 3.14 (d)**). Under an AC 2 V at 0.1 Hz, the blocking force of **PIt(//)** and **PIt**-based actuators are 0.7 and 0.37 mN, respectively. This may be due to the synergistic effect of the aligned 2D ion channels across the film and the higher young's modulus. As the response frequency is increased, the generated force gradually decreases to 0.04 mN at 2 Hz, which is about the same as the material's own weight. The force generation of the layered actuator is remarkably higher than those reported previously, despite its low **IL** content (14.3 wt%). This may be attributed to the strong chemically cross-linked network and weak plasticity.

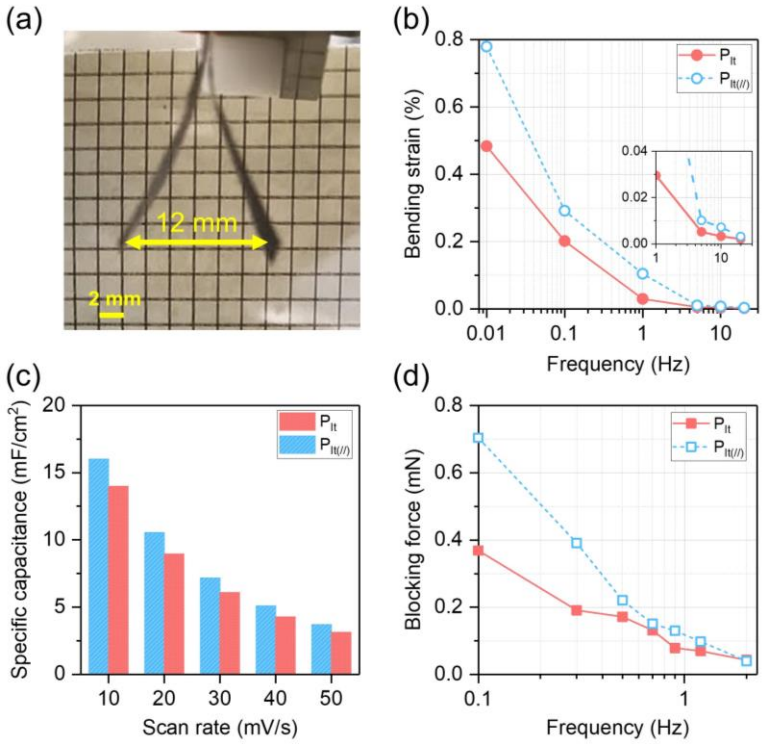

Figure 3.14 (a) Photograph of a bending actuator based on **PIt(//)** film. (b) Frequency dependence of the bending strains of randomly oriented **PIt**-based actuator and planar oriented **PIt(//)**-based actuator under an AC voltage 2 V. (c) Specific capacitance for these actuators at different scan rates. The electric potential window is -1 V to 1 V. (d) Frequency dependence of the blocking force for these actuators at AC voltage 2 V. The generation force data was recorded from the actuator with the dimensions of 10 mm in length, 3 mm in width, and 80 μm in thickness.

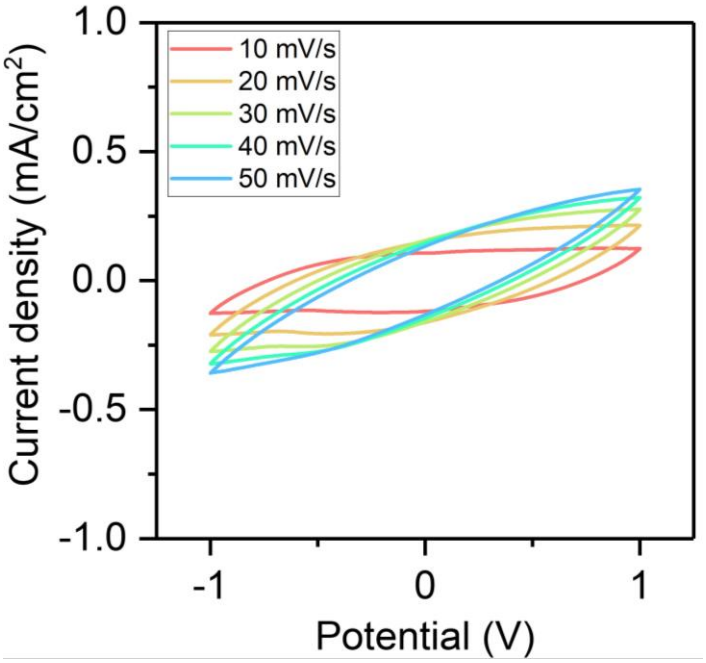

Figure 3.15 Cyclic voltammograms of $\mathbf{P_{It(//)}}$-based actuator with the potential range of -1 to 1 V at scan rate of 10 to 50 mV s^{-1}.

3.3.5 Combined the printable technology for preparation of ionic actuators.

To fully explore the potential of printable technology in the preparation of ionic actuators, a T-shaped photomask was utilized to fabricate a patterned LC film and actuator (**Figure 3.16**). The photomask was covered on the glass substrate while the LC phase was formed inside, and followed by exposure to UV light for photocuring. The sharp contrast between polymerization and non-polymerization regions can be distinguish by heating the sample to its isotropic melt state. The POM texture reveals that the regions covered by the mask did not undergo polymerization, and appeared as isotropic liquid when subjected to heat. In contrast, the presence of the smectic LC structure signifies successful polymerization in that area (**Figure 3.16 (a), (iii)**). Finally, the patterned actuator was achieved by laying **PEDOT:PSS** electrodes onto the electrolyte surface.

I prepare a soft actuation platform which can performed by connecting the patterned actuator to the indium tin oxide (ITO)-coated glass substrates (**Figure 3.16 (b)**). By applying a DC voltage, the main body and branches of the T-shaped actuator exhibit different bending directions, respectively. I successfully demonstrated a simple method to prepare the printable ionic actuator with different bending modes. The special patterned actuator could be prepared by not only photomask but also accurate laser cutter, and the various benefits including high bending strain, efficient ionic pathways, and mechanically toughness can be maintained. These advantage of photocuring manufacture serve as a promising way to guide the tiny actuators into Micro Electro-Mechanical Systems (MEMS). Furthermore, in the application fields of haptic sensors, the single actuator having various directions of actuation would be advantageous in increasing the contact area and enhancing the feedback, which might potentially result in unprecedented and superior outcomes (**Figure 3.16 (c)**).

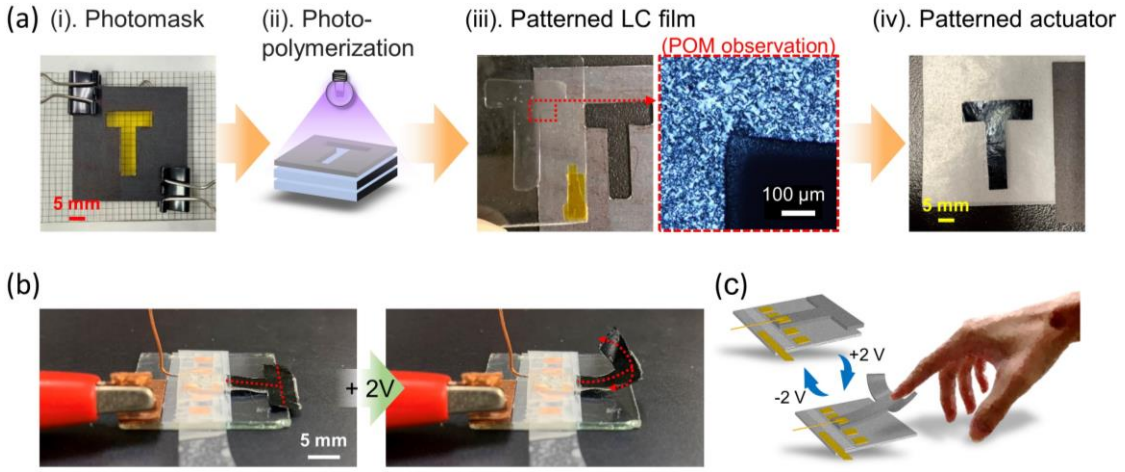

Figure 3.16 (a) The flow chart shows the preparative methodology of the patterned actuator. (b) A facile actuation platform that was able to exhibit the stereoscopic bending behavior with two different directions at an ITO glass under the application of DC 2 V. (c) The schematic illustrates that the T-shaped patterned actuator can be applied in the haptic sensor.

3.3.6 Sustainable biodegradation of itaconic polymer film.

The biomass itaconate film demonstrates biodegradation properties through soil incubation, as shown in **Figure 3.17**. This degradable itaconate polymer film offers a sustainable alternative to commercial plastics, providing promising opportunities for environmentally friendly materials.[37,38] The optical appearance of the itaconate film changes from transparent to cloudy after 3 weeks of soil burial test, and microscope observations illustrate some holes and weak topographical spots on the membrane surface. SEM observation further confirms the degradation of the itaconic film (**Figure 3.18**). The notable changes in the film structure can be ascribed to the decomposition of the ester bonds on the itaconate molecule by microorganisms. This caused the formerly dense and smooth membrane to turn rough and porous.

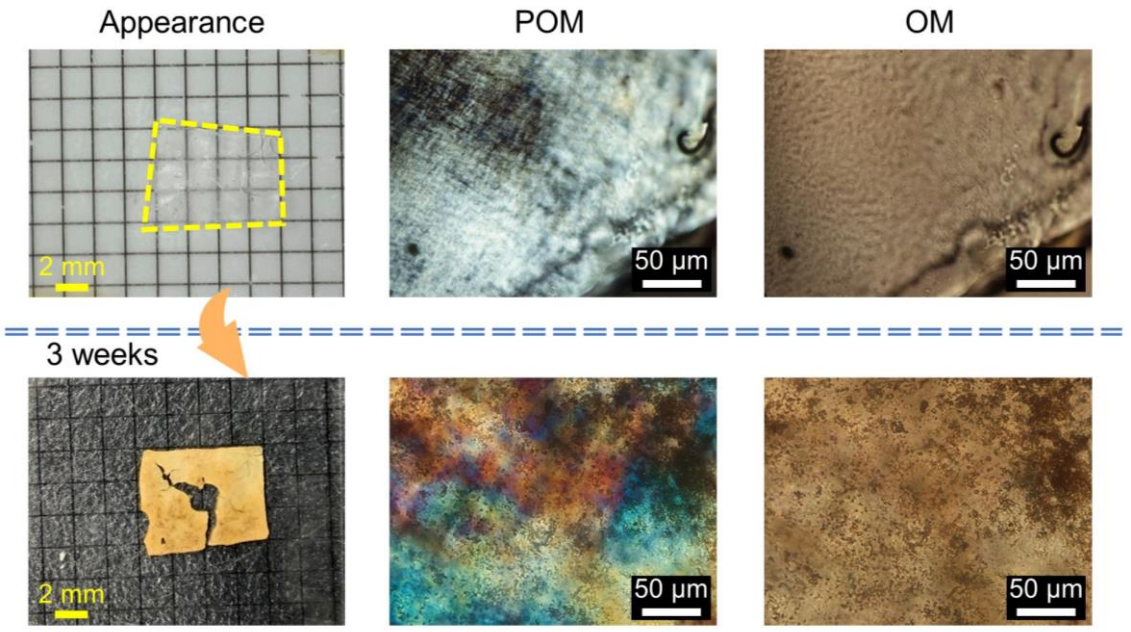

Figure 3.17 Photographs of $\mathbf{P_{It}}$ and the polarized optical microscope (POM) and optical microscope (OM) images before and after soil incubation for 3 weeks. The initial itaconate film $\mathbf{P_{It}}$ is transparent. After soil incubation, the film became opaque and had a rough surface topography.

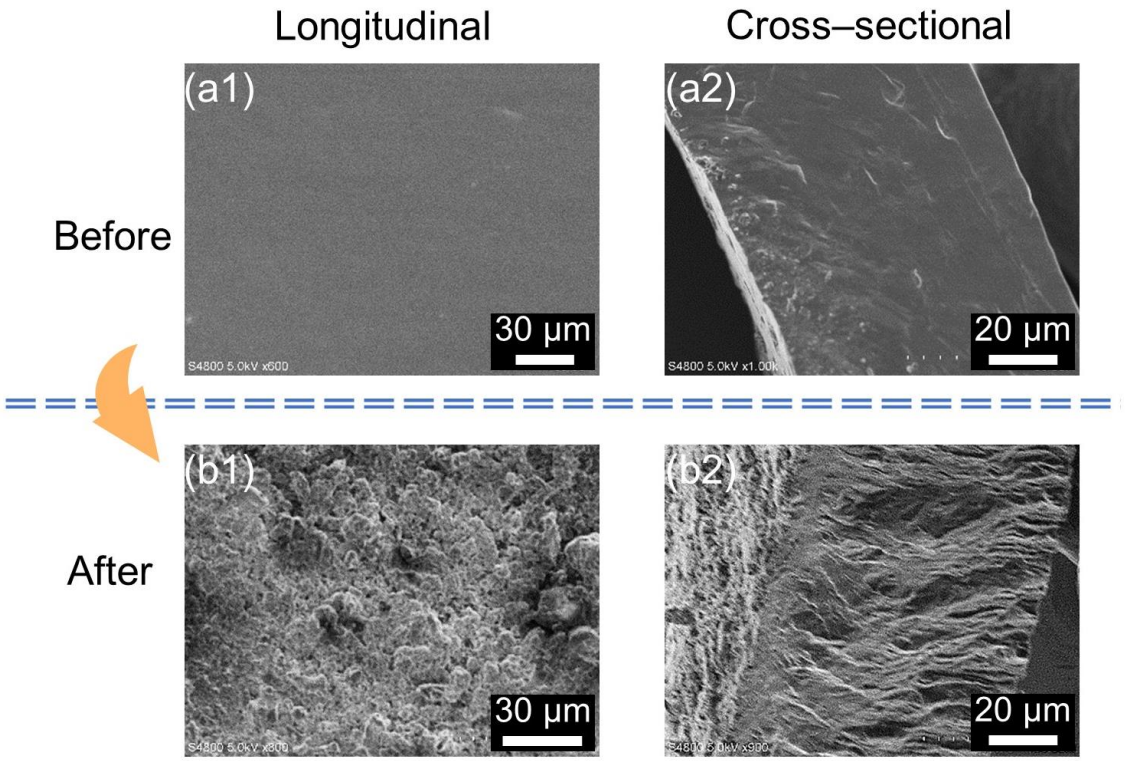

Figure 3.18 The longitudinal and cross-sectional SEM images of $\mathbf{P_{It}}$ (a1 and a2) before and (b1 and b2) after soil incubation for 3 weeks.

3.4 Conclusions.

In conclusion, I have reported a new design of photopolymerizable LC itaconate derivative, functionalized by an imidazolium salt. Through the complexation with an ionic liquid, I demonstrate the expansion of ionic layered structure to the gyroid cubic and hexagonal columnar phases with inverted polar domains. These findings offer multiple options for designing ion-conductive materials, including the knowledge on modulus, LC phase, ionic liquid contents, and ionic conductivity. Our results also show that the photo-preserved layered LC electrolyte can be applied to ionic electroactive actuators, which exhibit excellent bending performance even under low ionic liquid contents. Macroscopic alignment of the layered nanostructure can significantly improve the bending strain and generation force. The combination of simple production and multifunctional molecular structures offers new approaches for developing next-generation ion conductive materials.

3.5 References.

(1) H. Bai, S. Li, and R. F. Shepherd, *Adv. Funct. Mater.*, 2021, **31**, 2009364.
(2) Ankit, T. Y. K. Ho, A. Nirmal, M. R. Kulkarni, D. Accoto and N. Mathews, *Adv. Intell. Syst.*, 2021, **4**, 2100061.
(3) S. Chen, M. W. M. Tan, X. Gong, and P. S. Lee, *Adv. Intell. Syst.*, 2021, **4**, 2100075.
(4) N. El-Atab, R. B. Mishra, F. Al-Modaf, L. Joharji, A. A. Alsharif, H. Alamoudi, M. Diaz, N. Qaiser and M. M. Hussain, *Adv. Intell. Syst.*, 2020, **2**, 2000128.
(5) J. Yin, R. Hinchet, H. Shea and C. Majidi, *Adv. Funct. Mater.*, 2021, **31**, 2007428.
(6) I. Must, E. Sinibaldi and B. Mazzolai, *Nat. Commun*, 2019, **10**, 344.
(7) M. H. Rahman, H. Werth, A. Goldman, Y. Hida, C. Diesner, L. Lane and P. L. Menezes, *Ceramics*, 2021, **4**, 516–541.
(8) C. Feng , C.P. H. Rajapaksha and A. Jákli, *Engineering*, 2021, **7**, 581–602.
(9) U. Raza, S. Oh, R. Tabassian, M. Mahato, V. H. Nguyen and I-. K. Oh, *Sens. Actuators B*, 2022, **352**, 131006.
(10) O. Kim, T. J. Shin and M. J. Park, *Nat. Commun*, 2013, **4**, 2208.
(11) S. Imaizumi, H. Kokubo and M. Watanabe, *Macromolecules*, 2012, **45**, 401–409.
(12) H. Kokubo, R. Sano, K. Murai, S. Ishii and M. Watanabe, *Eur. Polym. J.*, 2018, **106**, 266–272.
(13) N. Terasawa, *RSC Adv.*, 2017, **7**, 2443–2449.
(14) D. M. Correia, L. C. Fernandes, N. Pereira, J. C. Barbosa, J. P. Serra, R. S. Pinto, C. M. Costa and S. Lanceros-Méndez, *Appl. Mater. Today*, 2021, **22**, 100928.
(15) N. Terasawa and K. Asaka, *Sens. Actuators B*, 2017, **248**, 237–279.
(16) V. Panwar and A. Gopinathan, *J. Mater. Chem. C*, 2019, **7**, 9389–9397.
(17) L. Lu, J. Liu, Y. Hu, Y. Zhang, H. Randriamahazaka and W. Chen, *Adv. Mater.*, 2012, **24**, 4317–4321.
(18) S. Imaizumi, Y. Ohtsuki, T. Yasuda, H. Kokubo and M. Watanabe, *ACS Appl. Mater. Interfaces*, 2013, **5**, 6307–6315.
(19) J.-H. Baik, S. Kim, D. G. Hong and J.-C. Lee, *ACS Appl. Mater. Interfaces*, 2019, **11**, 29718–29724.
(20) A. J. D'Angelo and M. J. Panzer, *J. Phys. Chem. B*, 2017, **121**, 890–895.
(21) D. Zhou, D. Shanmukaraj, A. Tkacheva, M. Armand and G. Wang, *Chem*, 2019, **5**, 2326–2352.
(22) F. Yu, J.-H. Ciou, S. Chen, W. C. Poh, J. Chen, J. Chen, K. Haruethai, J. Lv, D. Gao and P. S. Lee, *Nat. Commun.*, 2022, **13**, 390.
(23) O. Kim, H. Kim, U. H. Choi and M. J. Park, *Nat. Commun*, 2016, **7**, 13576.
(24) C. Feng, C. P. H. Rajapaksha, J. M. Cedillo, C. Piedrahita, J. Cao, V. Kaphle, B. Lüssem, T. Kyu and A. Jákli, *Macromol. Rapid Commun.*, 2019, **40**, 1900299.
(25) K. Salikolimi, A. A. Sudhakar and Y. Ishida, *Langmuir*, 2020, **36**, 11702–11731.
(26) K. Goossens, K. Lava, C. W. Bielawski and K. Binnemans, *Chem. Rev.*, 2016, **116**, 4643–4807.
(27) C.-H. Wu, W. Meng and M. Yoshio, *ACS Materials Lett.*, 2022, **4**, 153–158.
(28) C.-H. Wu, W. Meng, K. Iakoubovskii and M. Yoshio, *ACS Appl. Mater. Interfaces*, 2023, **15**, 4495–4504.
(29) C. Liu, S. Cao and M. Yoshio, *Adv. Funct. Mater.*, 2023, **59**, 2300538.
(30) T. Ichikawa, M. Yoshio, A. Hamasaki, T. Mukai, H. Ohno and T. Kato, *J. Am. Chem. Soc.*, 2007, **129**, 10662−10663.
(31) T. Ichikawa, M. Yoshio, A. Hamasaki, S. Taguchi, F. Liu, X.-B. Zeng, G. Ungar, H. Ohno and T. Kato, *J. Am. Chem. Soc.*, 2012, **134**, 2634−2643.
(32) B. R. Wiesenauer and D. L. Gin, *Polym. J.*, 2012, **44**, 461–468.
(33) R. Mezzenga, C. Meyer, C. Servais, A. I. Romoscanu, L. Sagalowicz and R. C. Hayward, *Langmuir*, 2005, **21**, 3322–3333.
(34) P. Astolfi, E. Giorgini, D. R. Perinelli, F. Vita, F. C. Adamo, S.Logrippo, M. Parlapiano, G. Bonacucina, S. Pucciarelli, O. Francescangeli, L. Vaccari and M. Pisani, *Langmuir*, 2021, **37**, 10166–10176.
(35) H. Fan, J. Wang, Z. Tao, J. Huang, P. Rao, T. Kurokawa and J. P. Gong, *Nat. Commun.*, 2019, **10**, 5127.
(36) H. Yang, E. v. Ruymbeke and C.-A. Fustin, *Macromolecules*, 2022, **55**, 5058–5070.
(37) Y.-N. Phang, S.-Y. Chee, C.-O. Lee and Y.-L. Teh, *Polym. Degrad. Stab.*, 2011, **96**, 1653-1661.
(38) A. Bora and N. Karak, *Eur. Polym. J.*, 2022, **176**, 111430.

Chapter 4

Photocured Liquid-Crystalline Polymer Electrolytes with 3D Ion Transport Pathways for Electromechanical Actuators

4.1 Introduction.

Electromechanical soft actuators that transduce electrical energy into mechanical deformation are enabling new cutting-edge applications such as bio-mimicking robots[1–6] and medical devices.[7–11] There is a growing interest in ionic electroactive polymer (iEAP) soft actuators, leveraging a combination of electric double-layer capacitance and Faradaic redox reactions to store and release ionic charges.[12–14] iEAP actuators have multiple benefits such as large, quick, and silent deformation at low input voltages of less than 2 V[15–17] and the ease of fabrication compared with other soft actuators. To further improve the electromechanical actuation, introduction of self-organized ionic channels into polymer electrolytes is one of the promising approaches. Recent successes in iEAP actuators were based on the use of nanostructured polymer electrolytes containing an ionic liquid. Self-assembly of block copolymers,[15,18–20] liquid crystals,[21,22] and covalent organic frameworks[23] forms hierarchically ordered ionic nanochannels, which accelerates the ionic transport. However, most high-performance actuators based on these advanced electrolytes contain more than 50 wt% ionic liquid,[20,24–26] which increases the bending strain and reduces the response time but lowers the mechanical modulus. In addition, the presence of a liquid electrolyte in a polymer matrix enhances a risk of leakage, which restricts practical applications.

To overcome the trade-off between bendability and mechanical stiffness in iEAP actuators, I focus on the use of nanosegregated liquid-crystalline (LC) structures as ion transport pathways. Self-assembly of ionic liquid crystals derived from ionic liquids is particularly attractive for use in iEAP actuators because of their high ionic mobility in the ordered state. In this context, I have developed a new type of iEAP actuator using ion-conductive columnar LC polymer films (***Chapter 2***), in which a low amount of ionic liquid (8 wt%) was confined in one-dimensional (1D) ionic nanochannels (**Figure 4.1 (a)**).[27] Such "1D" LC actuators, in which the self-organized columns are randomly arranged between electrodes, exhibited a small bending strain of 0.2 % under a voltage of 2 V applied at a frequency of 0.01 Hz. Yet, it was able to generate a high blocking force that was 20 times of the actuator weight despite the low ionic liquid content. The output force of the 1D LC actuator is comparable to those of polymer iongel and block polymer actuators containing 30-80 wt % of ionic liquids.[8,28] Thus, our ionic LC polymers can contribute to the design of lightweight, mechanically tough actuators. However, the 1D LC actuators still suffer from small bending deformation and slow response time due to the discontinuity of the 1D ionic channels at the domain boundaries between the randomly oriented columns.

In this chapter, I propose a strategy to create a new columnar LC polymer membrane electrolyte having three-dimensionally (3D) connected ion pathways (**Figure 4.1 (b)**). I envision that self-assembly of nanosegregated columns, consisting of lipophilic cylinder surrounded by ionic shells, into a hexagonally ordered film can lead to efficient ion transport, even if the columns are randomly oriented. To create such 3D continuous ionic pathways, it is essential to design the molecular shape and intermolecular interactions such as electrostatic force and van der Waals forces and hydrogen bonds.[28–30] In this work, I have synthesized two wedge-shaped amphiphilic molecules shown in **Figure 4.1 (c)**: the methyl imidazolium salt **M–ILC** and its analogous vinyl imidazolium salt **V–ILC**. These molecules have two ionic head groups and a single lipophilic tail containing a polymerizable diene moiety. I chose 1–ethyl–3–methylimidazolium tetrafluoroborate as an ionic liquid (**IL**) that provides mobile ions to the 3D pathways. The segregation of the ionic and non-ionic moieties and the geometry of the molecules can allow the mixtures to be organized into pizza-like disks and columns by stacking them (**Figure 4.1 (d)**). The vinyl moiety of **V–ILC** can be utilized to rigidify columnar networks by inter- and intra-columnar polymerization at the outer part of the columns. Although the supramolecular columnar LC assembly of tapered molecules, pioneered by Percec, Gin, and co-workers[31,32] has been utilized to develop functional nanostructured membranes[33–36] for water treatment[37–39] and battery electrolytes,[40,41] the 3D ion transport and electromechanical actuation based on the thermotropic columnar ionic LC polymer membrane has not been demonstrated so far.

In the present study, I have inverted the polar domains in the supramolecular columns by self-assembly of the amphiphilic imidazolium salts of **M–ILC** and **V–ILC** and the ionic liquid **IL** (**Figure 4.1 (c), (d)**), and preserved the nanostructures forming the 3D ionic pathways in solid polymer films by photopolymerization. The LC membranes sandwiched between conductive polymer electrodes (**Figure 4.1 (b)**) exhibit high bending strain (0.8 % at 2 V and 0.01 Hz), a wide frequency response (0.01-20 Hz), a voltage-controllable blocking force (from 0.3 mN to 1.1 mN at 0.2-2 V) and long-term stability (> 16,000 cycles). It is noteworthy that such improved actuation performance compared with the 1D LC actuator was realized by incorporating only 5.6 wt% (20 mol%) of **IL** into the 3D ordered solid membranes. This approach may open a new route for the fabrication of miniature soft robots, tactile sensors, and energy-storage devices.

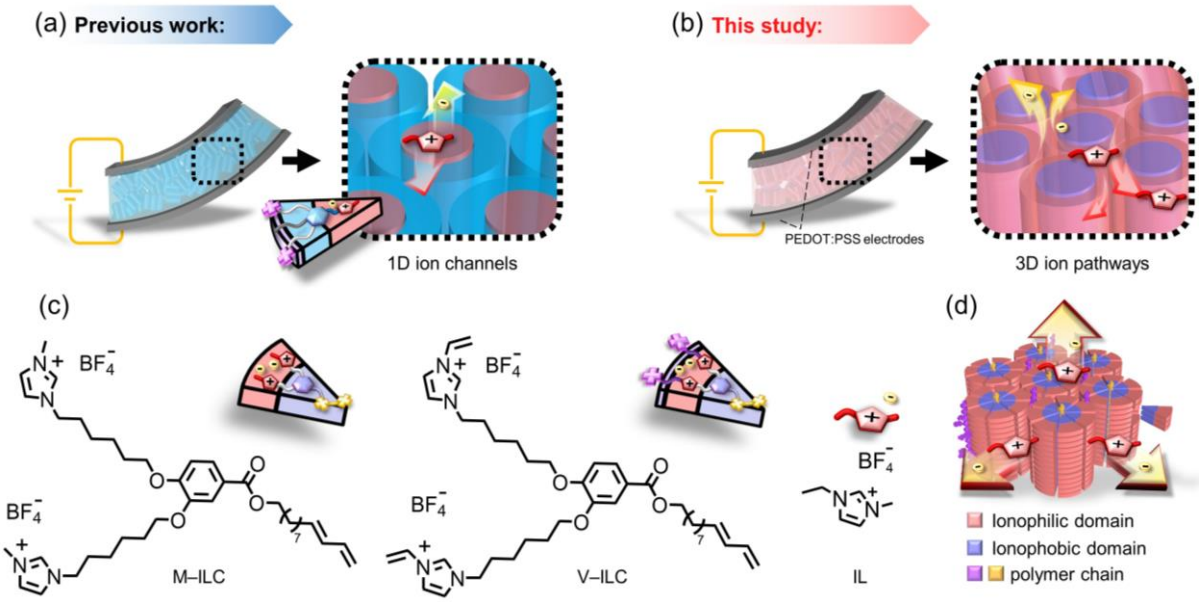

Figure 4.1 Design strategy of the iEAP actuators using Col_h ionic LC polymer membranes with different dimensions of ion channels. (a) 1D ion-conductive polymer membrane electrolyte (***Chapter 2***)[27]. A polymerizable fan-shaped molecule having a single ionic head and lipophilic chains with polymerizable acrylate moieties at the ends was assembled with an ionic liquid to form a nanosegregated columnar LC structure. 1D transport of an ionic liquid confined in the ionic channels (red) shielded by lipophilic chains (blue) leads to a bending actuation under an applied voltage. (b) 3D ion-conductive Col_h LC polymer membrane electrolyte with interconnected ionic paths, which is sandwiched between a pair of **PEDOT:PSS** electrodes to fabricate electromechanical actuators (this work). (c) New polymerizable Col_h ionic LC molecules: the methyl imidazolium salt **M–ILC** and the vinyl imidazolium salt **V–ILC**. Structure of an ionic liquid, 1–ethyl–3–methylimidazolium tetrafluoroborate (**IL**). (d) Schematic illustration of 3D continuous ion transport in a nanosegregated columnar LC structure (red: ionic parts, blue: insulating parts) formed by self-assembly of the wedge-shaped ionic amphiphiles and the ionic liquid.

4.2 Experimental Section.

4.2.1 Materials.

1,9–Nonanediol (>98%), 3,4–dihydro–2*H*–pyran (>97%), anhydrous diethyl allyl phosphonate (>99%), *p*–toluenesulfonic acid monohydrate (TsOH, >98%), ethyl 3,4–dihydroxybenzoate (>98%), carbon tetrabromide (CBr_4, >99%), 4–dimethylaminopyridine (DMAP, >99%), 1–(3–dimethylaminopropyl)–3–ethylcarbodiimide (EDC, >98%), 1–methylimidazole (>99%), 1–vinylimidazole (>98%), 1–ethyl–3–methylimidazolium tetrafluoroborate (**IL**, >99%), and silver tetrafluoroborate ($AgBF_4$, >98%) were purchased from Tokyo Chemical Industry. Triphenylphosphine (PPh_3, 98%), sodium hydroxide (NaOH, 97%), potassium carbonate (K_2CO_3, 99%), sodium iodide (NaI, 99.5%), *n*–butyllithium (*n*–BuLi, 1.57 M hexane), 2,6–*di*–*tert*–butyl–4–methoxyphenol (BHT, 98%), and ethylene glycol were purchased from Kanto Chemical. Pyridinium chlorochromate (PCC, 98%), and hexamethylphosphoric triamide (HMPA, >98%) were purchased from Aldrich. 6–Bromo–1–hexanol (98%) was purchased from Combi–Blocks. Poly(3,4–ethylene dioxythiophene) polystyrene sulfonate **PEDOT:PSS** (Clevios™ PH1000) was purchased from Heraeus. 2,2–dimethoxy–2–phenylacetophenone, which was used as a photo-initiator, was purchased from Sigma-Aldrich. All the chemicals were used as received, without further purification.

4.2.2 Synthesis of M–ILC and V–ILC.

The detailed synthesis route, procedures, and their nuclear magnetic resonance (NMR) spectra were written in ***Appendix 7.3***.

4.2.3 Fabrication of P_V/IL(0) and P_{MV}/IL(x) actuators.

The mixture of **V–ILC** and 0.5 wt% photo-initiator (2,2–dimethoxy–2–phenylacetophenone) were dissolved in a mixed solution of chloroform/methanol (4/1 by volume) and the solvents were removed by rotary evaporator under light-resistant conditions. The residue was dried under vacuum at 30 °C for 1 day to give the liquid-crystalline sample of **V/IL(0)**. The monomeric sample **V/IL(0)** in the columnar phase was placed between an untreated cover glass and a glass substrate covered with a 110-μm-thick polyimide (PI) tape that determined the sample thickness. The sandwiched cell was heated to a temperature at which the sample became the isotropic liquid state and then cooled to room temperature at a rate of 1 °C/min to form a columnar nanostructure. Subsequently, the cell was irradiated with UV light (350 nm, 20 mW/cm^2) for 15 minutes at room temperature. After polymerization, the **P_V/IL(0)**

film was carefully peeled off from the substrate. The polymeric **P_V/IL(0)** film was sandwiched between two **PEDOT:PSS** sheets and pressed. The tri-layered composite was cut into 10 × 3 mm pieces that were used as **P_V/IL(0)** actuator.

The ternary mixture of **M–ILC** and **V–ILC** at the 50:50 ratio with a proper amount of the [EMIM][BF_4] ionic liquid (**IL**; The following table) and 2 wt% of photo-initiator (2,2–dimethoxy–2–phenylacetophenone) were dissolved in a mixed solution of chloroform/methanol (4/1 by volume), and the solvents were removed in a rotary evaporator under light–resistant condition. The residue was dried under vacuum at 30 ºC for 1 day to give a liquid-crystalline sample, which was subsequently photo-polymerized and turned into a **P_{MV}/IL(x)** actuator. (Samples represented as **x** mol% **IL** in the membranes.)

	Mole fraction			Weight fraction	
	M–ILC (mol%)	**V–ILC (mol%)**	**IL (mol%)**	**LC (wt%)**	**IL (wt%)**
MV/IL(0)	50	50	0	100	0
MV/IL(10)	45	45	10	97.4	2.56
MV/IL(20)	40	40	20	94.4	5.60
MV/IL(30)	35	35	30	90.3	9.23

4.2.4 General methods.

DSC measurements were carried out under a continuous argon purge (40 mL/min) using NETZSCH DSC-3500 Sirius connected with a liquid nitrogen cryo-system. The heating and cooling scan rates were 10 ºC/min. Polarized optical microscopy observations were conducted using an Olympus BX51N-31P-O3 microscope equipped with a DP22 digital camera and a temperature control system (LINKAM T95-HS, LTS420E). XRD measurements were carried on a Rigaku Min-iFlex 600 diffractometer using Ni-filtered Cu Kα radiation. A 100 W xenon lamp (Asahi Spectra, HAL-C100) passed through a 345-355 nm bandpass filter was employed as a UV irradiation source. Tensile tests were performed with a Shimadzu EZ-S setup at a stretching speed of 10 mm per minute. TEM observations were carried out with a JEOL 2100 microscope at room temperature and an acceleration voltage of 80 kV.

4.2.5 Fabrication and observation of TEM samples.

A parallel oriented LC columns film: **$P_{MV(//)}$/IL(20)** was trimmed with a razor, embedded into a commercial epoxy resin (Spurr from Polyscience) and cured at 70 ºC overnight. This

composite was then sliced with a diamond knife in a Leica EM UC6 microtome at a speed of 0.8-1.0 mm s^{-1} at room temperature. Slicing was performed perpendicular to the film and yielded 70-nm-thick flakes, which were transferred to standard copper meshes and observed in a JEM 2100 microscope at 80 kV. Observations were performed in the bright-field TEM mode, at sufficiently low beam intensity to avoid beam-induced sample damage. The recorded TEM images were processed with the Digital Micrograph software from Gatan, namely, a fast Fourier transform (FFT) and a default bandpass filter were applied to the raw image.

4.2.6 Cyclic voltammetry measurements.

Cyclic voltammetry measurements were carried out using an electrochemical analyzer (model 611E, CH Instruments) in a potential range of 1 to -1 V at scan rates varying from 5 to 100 mV s^{-1}. The specific capacitance (C_{sc}) was calculated as:

$$C_{sc} = \frac{\int_{V_1}^{V_2} i\, dV}{A(V_2 - V_1)v} \quad \ldots\ldots\ldots\ldots\ldots\ldots\ldots\ldots\ldots\ldots\ldots\ldots\ldots\ldots\ldots (1)$$

where i is the instant current (A), A is the surface area of electrode (cm^2), v is the scan rate (V s^{-1}), V_2 and V_1 are the high and low potential limits (V).

4.2.7 Ionic conductivity measurements.

Alternating current impedance measurements were carried out using a Metrohm AUTOLAB PGSTAT128N impedance analyzer. The frequency range was 10^2-10^7 Hz and the applied voltage was 0.6 V. The sample were sandwiched between a pair of indium tin oxide (ITO)-coated glass substrates using a 55 μm thick polyimide tape spacer with a 3 mm diameter hole. The alignment-dependent ionic conductivity was measured in a gap cell geometry using interdigitated gold electrodes. The temperature was controlled with the Linkam hot stage. The impedance data were recorded every 5 ºC upon heating from 25 to 80 ºC. They were fitted by the equivalent circuit consisting of a constant phase element and a parallel RC element. Ionic conductivity σ (S cm^{-1}) was calculated as $\sigma = L/R_b A$, where R_b is the bulk resistance (Ω), L is the sample thickness (cm), and A is the sample area (cm^2). The R_b value was obtained from the intercept of a semicircle on the real axis of impedance in Nyquist plots. Temperature–dependent ionic conductivities were fitted by the Arrhenius equation: $\sigma = \sigma_0 e^{(\frac{-E_a}{RT})}$, where R = 8.314 J K^{-1} mol^{-1} is the ideal gas constant, E_a is the activation energy (J mol^{-1}), T is the absolute temperature (K), and σ_0 is the pre-exponential factor (S cm^{-1}).

4.2.8 Actuation performance test.

The actuator strip was clamped between two stainless-steel electrodes connected to a potentiostat (Hokuto Denko, HAL3001A). Symmetrical square-wave alternating voltages or direct voltage generated by a function generator (YOKOGAWA FG400 30MHz) was controlled by the potentiostat and applied to the actuator. Bending displacement was measured with a laser meter (Keyence, LK-H050 and LK-HD500). The laser was irradiated perpendicular to the actuator surface at a distance of 8.5 mm from the electrode. The signals of voltage, current, and displacement were recorded in a digital data logger (HIOKI LR8880). The actuation was captured using a USB camera (Sanwa Supply, 400-CAM058). The blocking force was measured by the load sensor connected to a force detection monitor (KYOWA LTS-50GA/KYOWA WGA-680A). The bending strain (%) was calculated as $\varepsilon = 2\delta d \times 100/(\delta^2 + L^2)$, where δ is the peak-to-peak displacement, d is the total thickness of actuator, and L is the free length of the actuator. The actuation tests were performed under ambient atmosphere with an average relative humidity of (40 ± 5)%.

4.2.9 Preparation of artificial electronics devices and their operation.

To fabricate the artificial jellyfish, two pieces of the LC actuators (dimension of actuators: 11 mm × 4.5 mm × 110 μm; weight: 7.5 mg) arranged in parallel were attached to the surface of a silicone elastomer sheet (weight: 11 mg) containing a luminescent dye. Each actuator was clamped by two magnetic conductive plates. A copper wire was attached to one side of the plate. Two pairs of magnet plates were attached while inserting another copper wire so that the inner surfaces were short-circuited. The outer two wires were connected. By applying a DC voltage of ± 2 V, the two actuators can bend in opposite directions, causing the silicone elastomer sheet to flip. The silicone elastomer was prepared by mixing silicone elastomer base, curing agent (SYLGARDTM 184) and pyrene, and then crosslinked in the 80 °C oven for 5 hours. Similarly, a two-finger actuator was used as a miniature forceps to demonstrate the capture and release of an aluminum block (20 mg) under ambient conditions.

4.3 Results and Discussion.

4.3.1 Liquid-crystalline and ion-conductive properties of ionic amphiphiles.

Monomers **M–ILC** and **V–ILC** exhibit a hexagonal columnar (Col_h) LC phase at ambient temperature. Polymerizable compound **M–ILC** (**Figure 4.2 (a)**) forms a Col_h phase between 82 and -35 °C on heating, while the Col_h phase of cross-linkable **V–ILC** shows a narrower stability range from 34 to -30 °C, probably due to the steric hindrance by the bulky vinyl group on the imidazolium ring. Polarized optical microscopy (POM) photographs of **M–ILC** and **V–ILC** (**Figure 4.2 (b)(c)**) show fan textures in the vertically oriented column domains. The room-temperature X-ray diffraction (XRD) pattern of **M–ILC** shows three peaks at 2.04, 3.45, and 4.05 degrees (**Figure 4.2 (d)**: (i), upper panel). The reciprocal *d*-spacing ratio of these peaks is $1 : \sqrt{3} : 2$, which can be indexed to the (100), (110), and (200) reflections of a Col_h phase. Compound **V–ILC** shows a similar columnar structure in the LC phase (**Figure 4.2 (d)**: (ii), lower panel) but a different temperature dependence of ionic conductivity (**Figure 4.2 (e)**). The conductivity of **V–ILC** in the polydomain orientation at room temperature is one order of magnitude lower than that of **M–ILC**. This difference can be explained as follows: the drift of anions can be restricted at lower temperatures by the formation of stronger hydrogen bond between the fluorine atoms in the anion, the *N*–vinylic proton, and the carbonic C(2) proton on the imidazolium cation.[43]

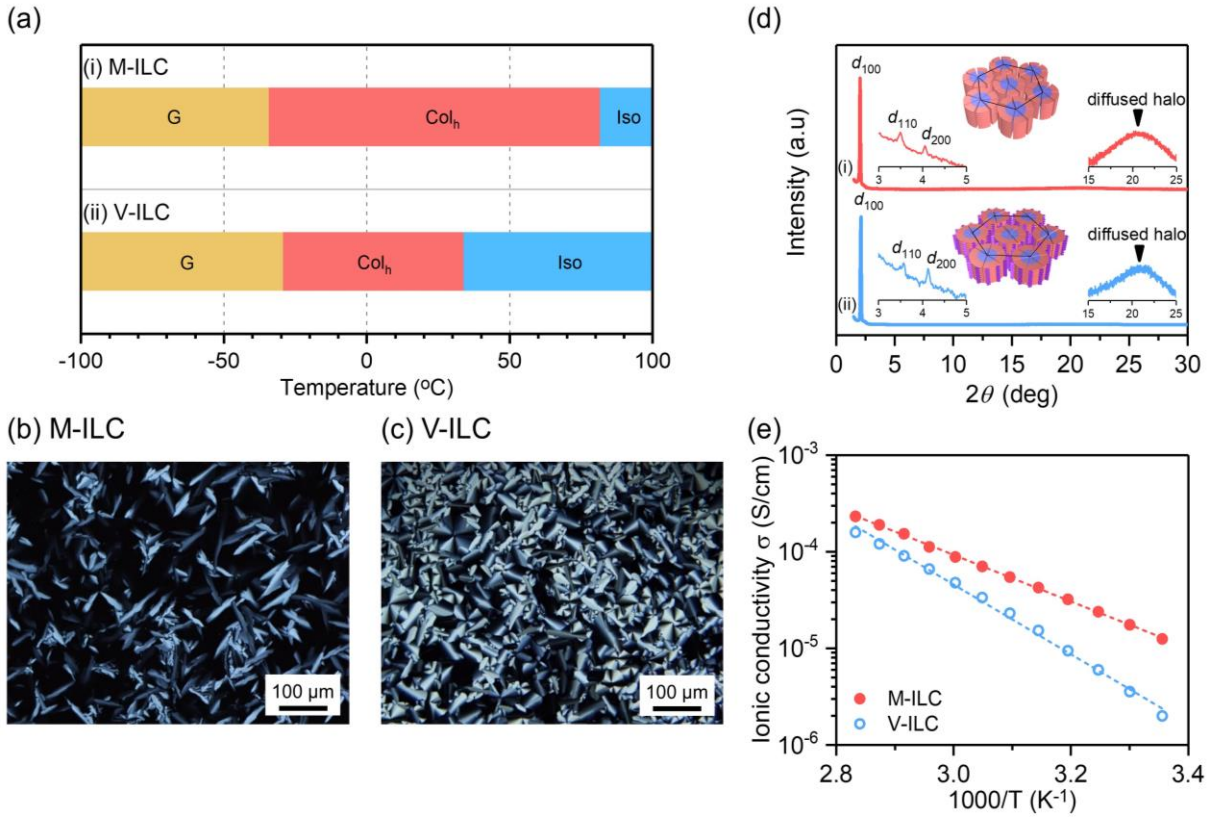

Figure 4.2 Characterization of LC and ion-conductive properties of **M–ILC** and **V–ILC**. (a) Phase transition behavior. G, Col$_h$, and Iso are glassy, columnar hexagonal LC, and isotropic liquid phases, respectively. (b) Polarized optical micrograph (POM) of **M–ILC** in the Col$_h$ phase under crossed Nicol's condition. The vertically oriented domains of columns sandwiched between two glass slides show no birefringence (black image). (c) POM image of the randomly oriented columnar LC phase for **V–ILC**. (b,c) The LC textures were observed at 25 °C after cooling from isotropic melts. (d) XRD patterns of (i) **M–ILC** and (ii) **V–ILC** at room temperature. The insets magnify selected regions of XRD patterns and show schematics of the self-assembled columnar structures. (e) Temperature dependence of the ionic conductivities for **M–ILC** and **V–ILC**.

4.3.2 Liquid-crystalline and ion-conductive properties of ionic liquid-containing mixtures.

1–Ethyl–3–methylimidazolium tetrafluoroborate (**IL**) as a lyotropic solvent is highly compatible with ionic LC monomers **M–ILC** and **V–ILC** due to the similar chemical structure of the ionic moieties. For example, compound **M–ILC** is miscible with **IL** up to 60 mol% **IL** in the mixture (**Figure 4.3**). The binary mixtures based on **M–ILC** containing 30 mol% **IL** form a Col_h phase, and a further addition of **IL** results in a micellar cubic (Cub) phase. This Col_h-Cub conversion may be caused by increase in the hydrophilic volume. With increasing **IL** content, the transition temperature from LC phase to isotropic liquid decreases, but the ionic conductivity increases (**Figure 4.4**). The ionic conductivity at 25 °C for **M–ILC** and the mixture of **M–ILC** and **IL** in a 7:3 molar ratio is 1.3×10^{-5} and 6.1×10^{-5} S cm^{-1}, respectively. The conductivity is enhanced by about 5-fold by the incorporation of **IL**. The results of this phase transition behavior and ionic conductivity for the mixtures suggest that the incorporation of **IL** makes the LC nanostructures more fluid and the ionic domains for the Col_h assemblies cover the outside of the periodic honeycomb cylinders occupied by the alkyl chains of ionic amphiphiles.

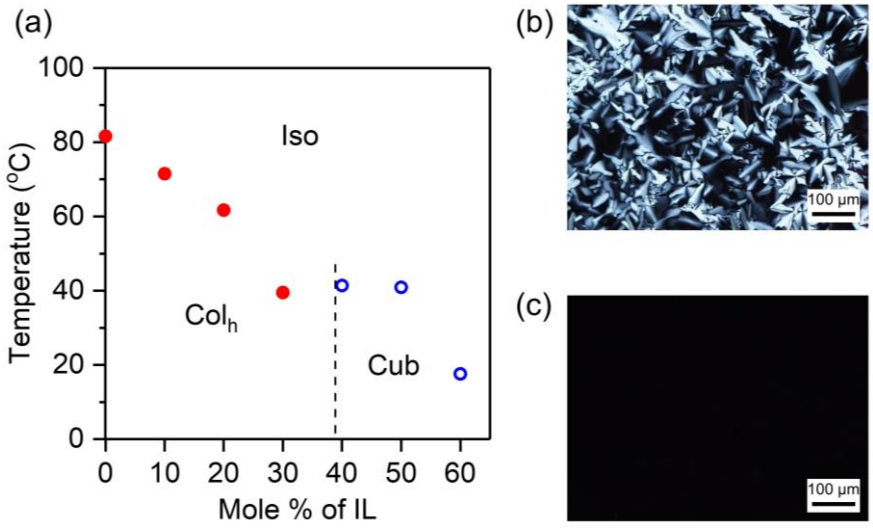

Figure 4.3 (a) Phase transition diagram of **M–ILC** with various molar percentages of **IL**. Iso, Col_h, and Cub are isotropic liquid, hexagonal columnar, and micellar cubic phases, respectively. Polarized optical micrographs of the binary mixtures with (b) 20 mol% **IL** that form the hexagonal columnar phase, and (c) 50 mol% **IL** which shows no birefringence texture, indicating the formation of nanosegregated micellar cubic phase.

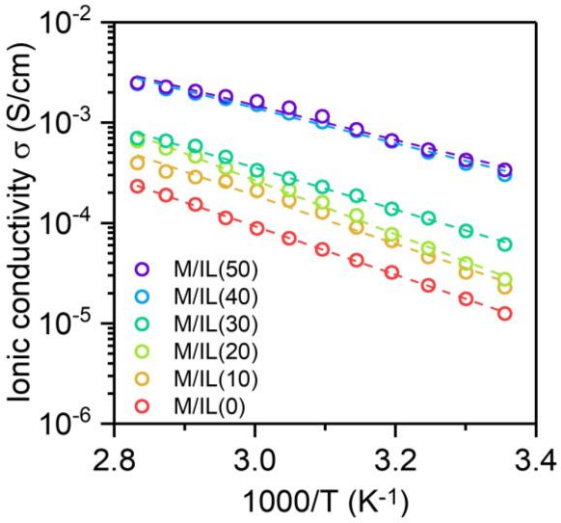

Figure 4.4 Temperature dependence of ionic conductivity for **M–ILC** with various molar percentages of **IL**. Sample name: **M/IL(x)**, **x** = mol% **IL** in the mixtures.

I prepared ternary mixtures of **M–ILC**, **V–ILC**, and **IL** to obtain radially cross-linkable Col_h mixtures at room temperature so that the photopolymerized films could achieve high ionic conductivity and sufficient mechanical stiffness as the electrolytes for iEAP actuators. These ternary mixtures are denoted as **MV/IL(x)**, where **MV** is the equimolar binary mixture of **M–ILC** and **V–ILC** and **x** is the mole% of **IL** in the mixture. **MV/IL(x)** mixtures with 10 and 20 mol% **IL** exhibit a Col_h phase at room temperature, as confirmed by XRD measurements (**Figure 4.5**). For example, the ternary mixture **MV/IL(20)** shows a glass transition at -40 °C and a Col_h-Iso transition at 33 °C on heating, whereas the Col_h-Iso phase transition for the binary mixture **MV/IL(0)** is detected at 47 °C.

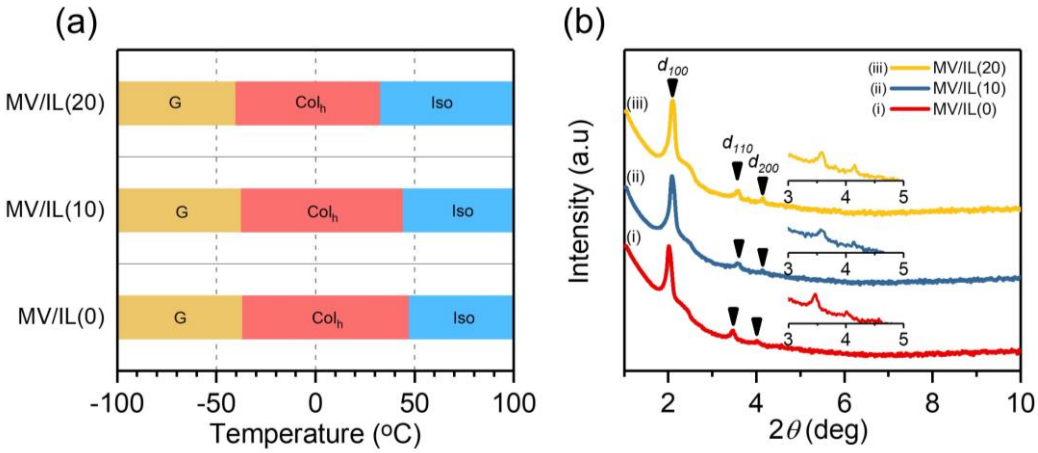

Figure 4.5 (a) Phase transition behavior and (b) XRD patterns of the monomeric binary mixture consisting of **M–ILC** and **V–ILC** (denoted as **MV/IL(0)**) and the ternary mixtures **MV/IL(x)** with 10 and 20 mol% of **IL**.

The self-organized columns of **MV/IL(20)** have been macroscopically aligned by shearing them parallel and perpendicular to the electric field between comb-shaped gold electrodes on a glass substrate for anisotropic ionic conductivity measurements (**Figure 4.6**). The temperature-dependent conductivity measurements of **MV/IL(20)** with a polydomain orientation and separately a uniform planar orientation of the columns clarify the existence of 3D network of nanoscale ionic pathways in the Col$_h$ phases. The ionic conductivity parallel to the columnar axis ($\sigma_{//}$, ○) of **MV/IL(20)** is slightly higher than that perpendicular to the columnar axis ($\sigma_{\perp}$, □). The anisotropy ratio ($\sigma_{//}/\sigma_{\perp}$) is about 1.16, which is much smaller than that of columnar liquid crystals forming 1D ionic channels ($\sigma_{//}/\sigma_{\perp} >$ 10-100).[41,44] In addition, the ionic conductivities of the randomly oriented columns (σ, △) in the polydomain sample are nearly identical to those parallel to the columnar axis ($\sigma_{//}$, ○). The temperature dependences of these conductivities show Arrhenius behavior. The activation energy estimated from the slope of the conductivity plots seems to be almost the same regardless the differences in the alignment of the columns between the polydomain and aligned samples. These results suggest that ions can move continuously in any columnar orientation under an applied bias, which is a significant advantage for use as electrolytes in iEAP actuators. I also confirm that such an isotropic 3D ion transport pathway is formed in the columnar phases for the ternary mixture **MV/IL(10)**, binary mixture **MV/IL(0)**, and individual **M–ILC** and **V–ILC** components.

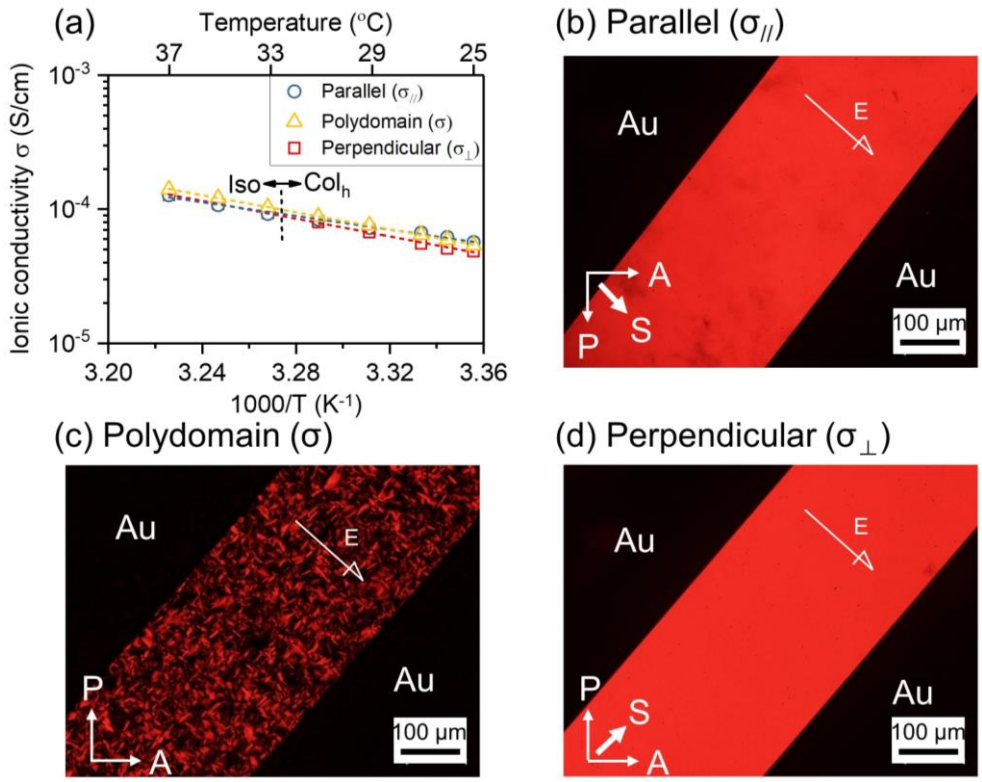

Figure 4.6 Ionic conductivities and columnar LC alignment of the monomeric mixture **MV/IL(20)**. (a) Temperature-dependent conductivities for the oriented columns (◯: parallel and □: perpendicular to the applied electric field) and randomly oriented columns (△). The vertical dashed line indicates the Col_h-Iso phase transition temperature. POM images for different orientations of the columns: (b) the columns are aligned by shearing to the direction of electric field, (c) the columns are randomly oriented between electrodes, and (d) the columns are aligned perpendicular to the electric field by shearing. Arrows indicate the directions of the mechanical shear force (*S*), analyzer (*A*), polarizer (*P*), and electric field (*E*).

4.3.3 Characterization of columnar nanostructured polymer films.

The self-organized columnar LC structures for **MV/IL(x)** with 0-20 mol% **IL** were preserved by radical cross-linking of the monomers into solid polymer membranes by UV irradiation for 15 minutes under ambient conditions. The obtained polymer films are somewhat optically cloudy and mechanically flexible. No significant change in the LC texture for **MV/IL(20)** upon polymerization was detected by POM (**Figure 4.7**).

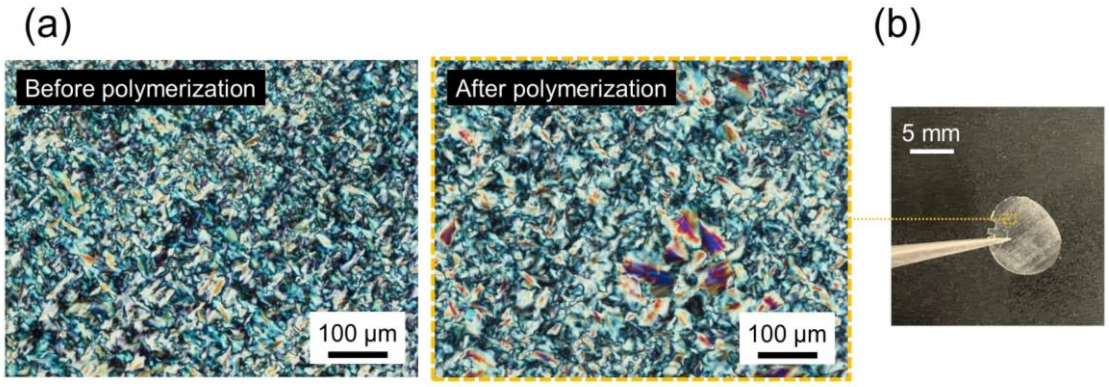

Figure 4.7 (a) Polarized optical micrographs of **MV/IL(20)** before and after photopolymerization. (b) The appearance of **PMV/IL(20)** polymer membrane.

The vinyl moiety on the imidazolium ring of **V–ILC** plays a key role in the production of mechanically tough films. After UV irradiation of **V–ILC**, **MV/IL(0)**, and **MV/IL(20)** in the Col_h phase sandwiched between two glass slides, the polymer films could be easily peeled off from glass. On the other hand, UV irradiation of **M–ILC** in the Col_h phase provided a gelatinous solid (**Figure 4.8 (c),(d)**), and no freestanding film could be formed by the polymerization of diene moieties. This is because inter- and intra-columnar covalent cross-linking is not possible for **M–ILC** at the periphery of each self-organized column. The **M–ILC** only has one chain-addition polymerizable group per molecule and thus only forms linear polymers rather than a cross-linked network as in the case of **V–ILC**, which contains three polymerizable groups per molecule. Polymerization of the diene and vinyl groups was confirmed by Fourier–transform infrared (FTIR) spectroscopy. The FTIR spectrum of monomeric **V–ILC** shows the C=C stretching vibrations of the diene and vinyl groups around 876-1013 cm^{-1} and 1650 cm^{-1}, and the C–H vinyl stretching vibration around 3014 cm^{-1}. After polymerization, these peaks are absent (**Figure 4.8 (a)**).

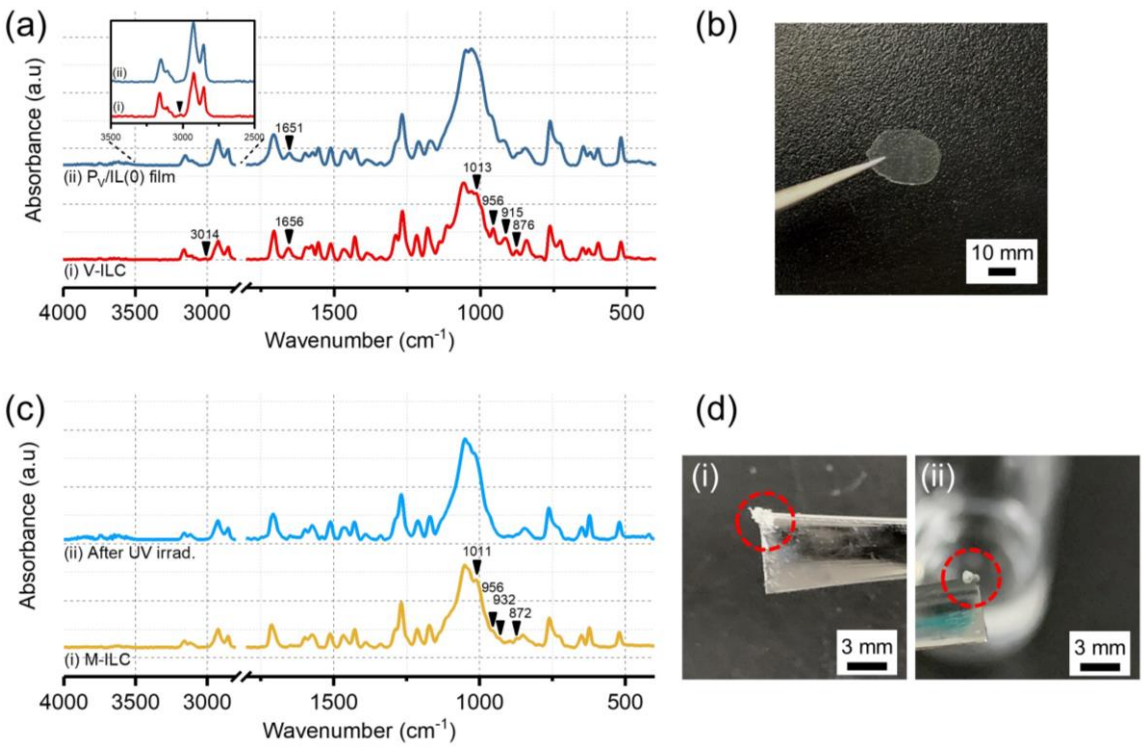

Figure 4.8 (a) FTIR spectra of the (i) monomeric **V–ILC**, and (ii) polymeric **PV/IL(0)** film. (b) The appearance of the free-standing **PV/IL(0)** film formed by photopolymerization. (c) FTIR spectra of the (i) monomeric **M–ILC**, and (ii) polymeric **PM/IL(0)** gel. (d) The appearance of (i) the **PM/IL(0)** gel, (ii) which shows swelling but does not dissolve in methanol.

The formation of columnar structure with 3D continuous ion pathways for **PMV/IL(20)** film is also consistent with TEM observations (**Figure 4.9**). The cross-sectional TEM image of aligned **PMV(//)/IL(20)** polymer film shows a phase-separated nanometer-scale structure with a nearly six-fold short-range symmetry, as evident from its fast Fourier transform (FFT) image. From the FFT image, the average distance between nearest-neighbor molecules was estimated to be 3 nm, which agrees with the inter-columnar distance estimated from XRD data (**Table 4.1**), provided that the corresponding hexagonal lattice contains not one but two inequivalent lattice sites. Two reasons can account for such inequivalence: (1) a structural difference between nearest neighbor molecules (as in binary inorganic compounds like hexagonal boron nitride) or (2) a lateral shift in the vertically aligned hexagonal layers of LC molecules (as in graphite). Note that the presence of inequivalent sites in a hexagonal LC is very difficult to deduce from the XRD data alone, and it could well be overlooked in previous studies.

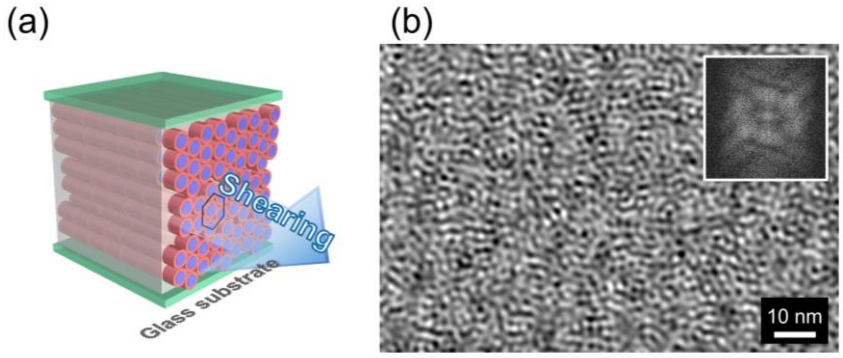

Figure 4.9 (a) Schematic of the shear-aligned **$P_{MV(//)}$/IL(20)** film that was sandwiched between glass slides for photo-polymerization. It was then peeled off and sliced perpendicular to the shearing direction for TEM observations. (b) TEM image of the film after filtering out high-frequency noise. Its fast Fourier transform (FFT) shown in the inset confirms the hexagonal symmetry, albeit with a distortion that might result from a local strain. The distance between the nearest-neighbor sites was estimated as 3 nm from the FFT image.

Table 4.1 Lattice parameters for the polymer film of **P_V/IL(0)**, **P_{MV}/IL(0)**, **P_{MV}/IL(10)** and **P_{MV}/IL(20)** determined from X-ray diffraction patterns for a hexagonal lattice with one or two types of dissimilar sites (n=1 or 2).

	Diffraction	Peak (2θ)	*d*-spacing (Å)	Intercolumnar distance, *a* (Å)
P_V/IL(0)	100	1.98	44.6	51.2 (n=1)
	110	3.44	25.7	29.6 (n=2)
	200	4.01	22.0	
P_{MV}/IL(0)	100	1.98	44.6	51.5 (n=1)
	110	3.41	25.9	29.8 (n=2)
	200	3.98	22.2	
P_{MV}/IL(10)	100	1.98	44.6	51.7 (n=1)
	110	3.40	26.0	29.9 (n=2)
	200	3.94	22.4	
P_{MV}/IL(20)	100	1.98	44.6	52.1 (n=1)
	110	3.41	25.9	30.1 (n=2)
	200	3.85	22.9	

As the content of **IL** increases in the Col_h nanostructured polymer films, the room-temperature ionic conductivity increases and the activation energy decreases (**Figure 4.10 (a)**). Nanostructured polymer electrolytes, **P_{MV}/IL(20)** with randomly aligned columns as a polydomain Col_h sample and **$P_{MV(//)}$/IL(20)** with the columns aligned parallel to the film surface as an aligned Col_h material, exhibit ionic conductivities of 2.7×10^{-5} and 2.1×10^{-5} S cm^{-1} at 25 °C, respectively. In contrast, the corresponding amorphous polymer film, **$P_{MV(Iso)}$/IL(20)** prepared by photopolymerization of **MV/IL(20)** in the isotropic liquid state, shows a room-temperature conductivity of 1.0×10^{-7} S cm^{-1} and an activation energy of 82 kJ mol^{-1} (**Figure 4.10 (b)**). The lower ionic conductivity of **$P_{MV(Iso)}$/IL(20)** may be attributed to the encapsulation of the **IL** in the rigid and entangled polymer matrix. **$P_{MV(Iso)}$/IL(20)** also shows lower conductivity than the Col_h polymer film of **P_{MV}/IL(0)** without **IL** (1.2×10^{-6} S cm^{-1}).

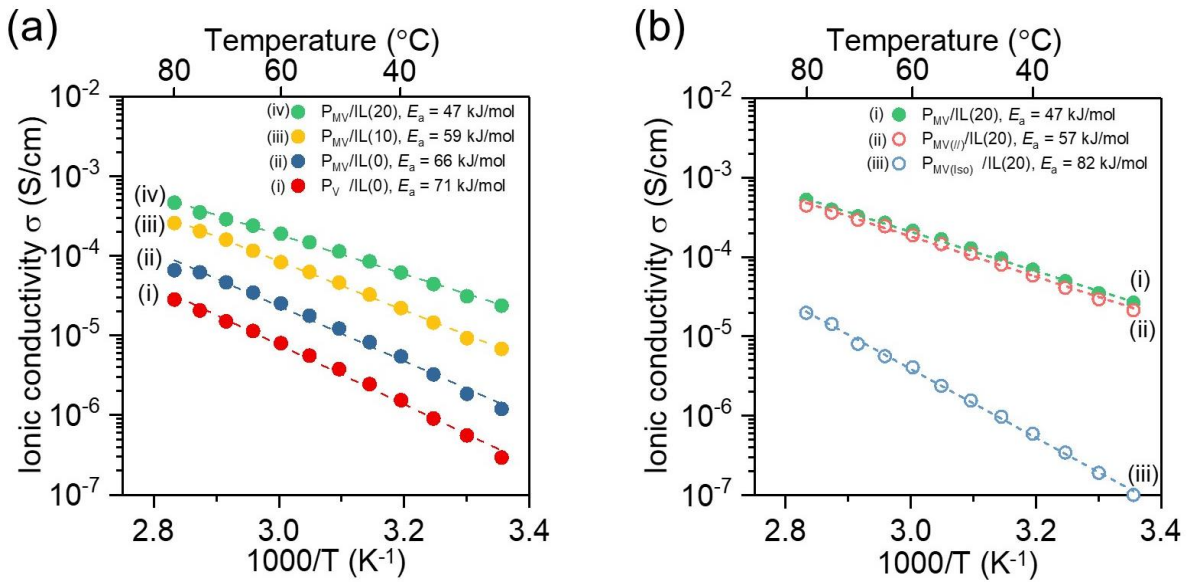

Figure 4.10 (a) Temperature dependence ionic conductivities of the **P_V/IL(0)**, **P_{MV}/IL(0)**, **P_{MV}/IL(10)** and **P_{MV}/IL(20)** films, and (b) **P_{MV}/IL(20)** based films with different nanostructure: (i) random columnar orientation (**P_{MV}/IL(20)**). (ii) columns parallel to the film surface (**$P_{MV(//)}$/IL(20)**). (iii) film with no columns (**$P_{MV(Iso)}$/IL(20)**).

4.3.4 Actuation performance of liquid-crystalline actuators.

Figure 4.11 (a) shows the bending displacement of nanostructured LC polymer actuators based on **P_{MV}/IL(20)** and **$P_{MV(//)}$/IL(20)** and an amorphous polymer actuator of **$P_{MV(Iso)}$/IL(20)** under applying an alternating square voltage of 2 V at 0.01 Hz under ambient conditions. The nanostructured electrolytes can induce a larger displacement due to their higher ionic conductivities compared with that of the corresponding amorphous electrolyte. The current flowing through the **P_{MV}/IL(20)**-based actuator shows a spike due to charging/discharging of the electric double layer formed at the electrolyte-electrode interface. In comparison, the **$P_{MV(//)}$/IL(20)** actuator shows a smaller peak-to-peak displacement than that of **P_{MV}/IL(20)**. The bending strains of **P_{MV}/IL(20)**, **$P_{MV(//)}$/IL(20)**, and **$P_{MV(Iso)}$/IL(20)** are calculated as 0.81 %, 0.64 %, and 0.017 %, respectively at 2 V and 0.01 Hz. Cyclic voltammetry measurements of these actuators at scan rates of 5-100 mV s^{-1} (**Figure 4.11 (c)**) reveal that the difference in capacitance between **P_{MV}/IL(20)** (19.51 mF/cm^2 under a scan rate of 5 mV s^{-1}) and **$P_{MV(//)}$/IL(20)** (17.32 mF/cm^2) is minute, but **P_{MV}/IL(20)** exhibits a higher specific capacitance probably due to the contribution of short ion-conductive paths along partially oriented columns perpendicular to the film surface. Meanwhile, **$P_{MV(Iso)}$/IL(20)** exhibits almost no charge storage capacitance (0.44 mF/cm^2), which suggests that the ionic liquid is trapped in the randomly entangled polymer chains and the ion transfer between electrodes does not occur.

Since the mechanical properties of polymer films and the orientation of nanostructures should affect the bending motion, I investigated the stress-strain behavior of three polymerized electrolytes by tensile strength measurements (**Figure 4.12**). Contrary to expectations, the amorphous **$P_{MV(Iso)}$/IL(20)** film exhibits the highest Young's modulus of about 38 MPa, about 2 times higher than that of **$P_{MV(//)}$/IL(20)**. Polydomain **P_{MV}/IL(20)** shows the lowest Young's modulus of about 12 MPa and the highest elongation-at-break (9%). The soft mechanical properties of **P_{MV}/IL(20)** with randomly oriented columns may be attributed to the formation of elastomeric structures by cross-linking between adjacent domains with different orientations of columns. The highest bendability of the **P_{MV}/IL(20)**-based actuator may originate from the synergistic effects of the highest ion migration through 3D continuous ion-pathways and the lowest Young's modulus of the analogous series of samples tested.

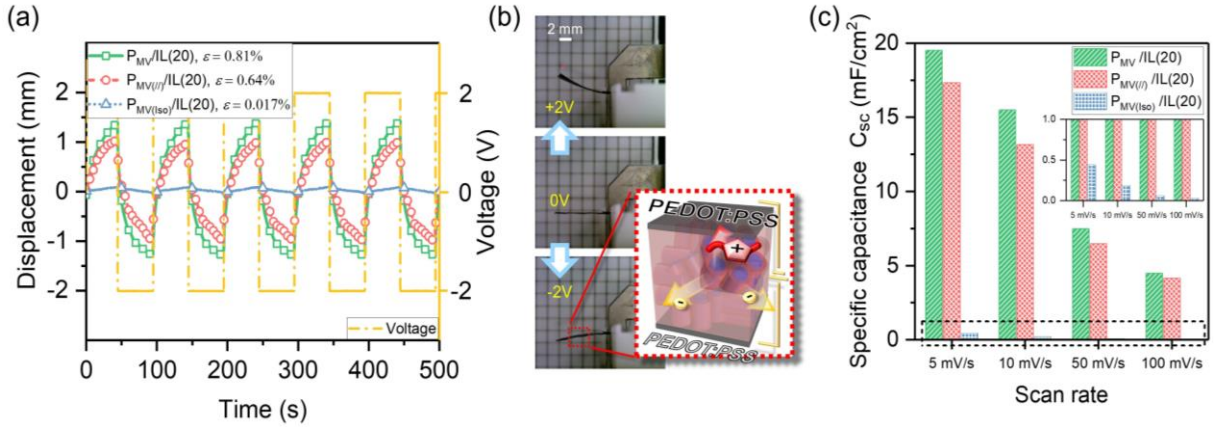

Figure 4.11 (a) Actuation properties of nanostructured polymer films based on **P_{MV}/IL(20)** and **$P_{MV(//)}$/IL(20)** and amorphous polymer film of **$P_{MV(Iso)}$/IL(20)** sandwiched between **PEDOT:PSS** electrodes under an AC voltage of 2 V at a frequency of 0.01 Hz. (b) Photographs of the **P_{MV}/IL(20)**-based actuator bending at ± 2 V and 0.01 Hz. The inset shows a schematic illustration of the ion migration in the 3D columnar pathways and the accumulation at the electrodes. (c) Specific capacitance for **P_{MV}/IL(20)** based actuators at different scan rates. The electric potential window is -1 V to 1 V.

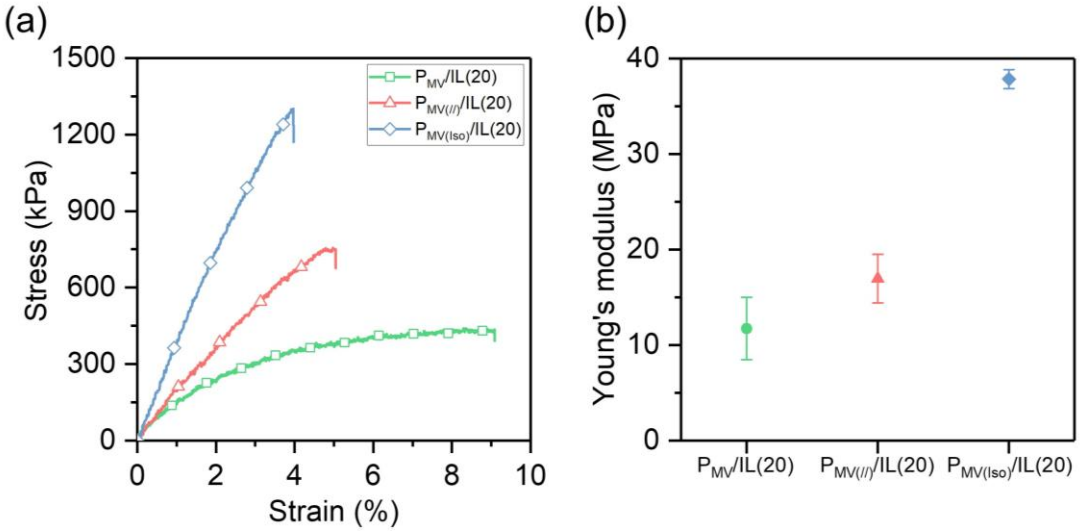

Figure 4.12 Mechanical properties of **P_{MV}/IL(20)**, **$P_{MV(//)}$/IL(20)**, and **$P_{MV(Iso)}$/IL(20)** films. (a) Tensile stress-strain curves. (b) Young's modulus.

Therefore, the **P_{MV}/IL(20)**-based actuator shows a broader frequency response up to 20 Hz and a strain value of 0.1 % at 1 Hz (**Figure 4.13 (a)**), while the response limit of the 1D ion-conductive liquid-crystalline actuator was 1 Hz and the strain was 0.0032 %.[27] Furthermore, the **P_{MV}/IL(20)**-based actuator exhibits good durability with only 5 % strain degradation over 15,000 cycles at 2 V and 1 Hz (**Figure 4.13 (b)**). Such bending actuation is mainly caused by the migration of ions through the 3D pathways.

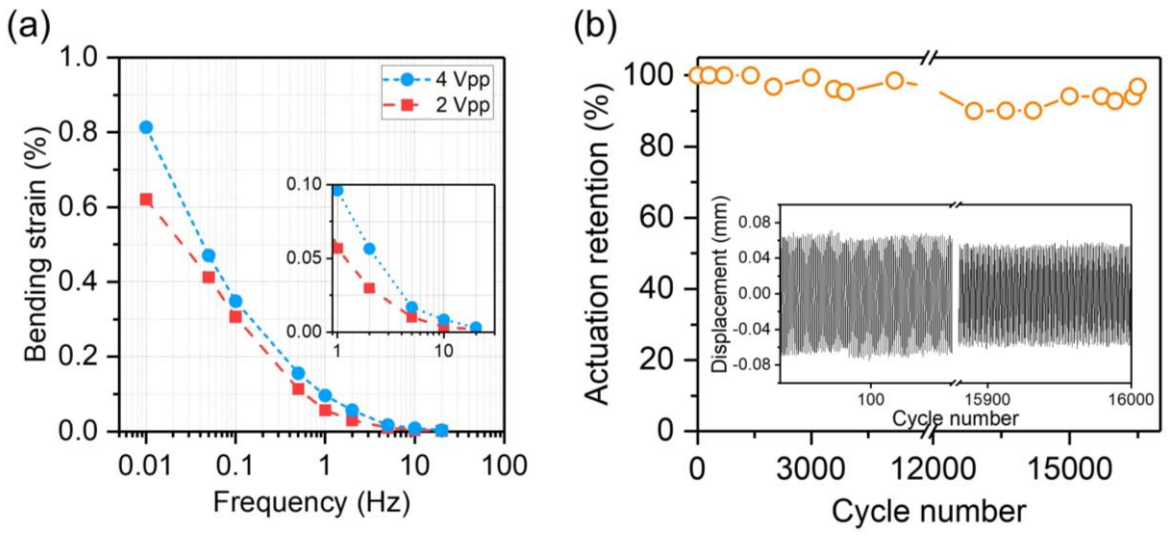

Figure 4.13 (a) Frequency dependence of the bending strain of the **P_{MV}/IL(20)**-based actuator under an AC voltage of 1 V and 2 V. (b) Cycle stability of the bending actuation for the **P_{MV}/IL(20)**-based actuator under 2 V at 1 Hz. The bending strain for each cycle is normalized by the initial strain value.

The blocking force of the **P_{MV}/IL(x)**-based actuators (x = 0-20) was investigated under DC and AC biases. **Figure 4.14 (a)** presents the blocking force of **P_{MV}/IL(20)**-based actuator under different input DC voltages. The actuator generates a force of 0.23 mN under a low input voltage of 0.2 V, which is comparable to that of our previous 1D ion-conductive Col_h actuator under 2 V.[27] The force of the **P_{MV}/IL(20)**-based actuator increases with increasing input voltage. When using a 2 V DC input voltage, the actuator exhibits a maximum force of 1.1 mN. In addition, the maximum force for the **P_{MV}/IL(20)**, **P_{MV}/IL(10)**, and **P_{MV}/IL(0)** based actuators is 0.6 mN, 0.3 mN, and 0.05 mN, respectively at AC 2 V and 0.1 Hz. To the best of our knowledge, such a high bending strain with high generated force has not been reported for iEAP actuators containing a low content of ionic liquids (**Figure 4.14 (b)**). The efficient ion transport,

both in the nanostructured polymer electrolytes and at the electrolyte/electrode interface, is thought to be responsible for the enhanced force generation at low input voltage.

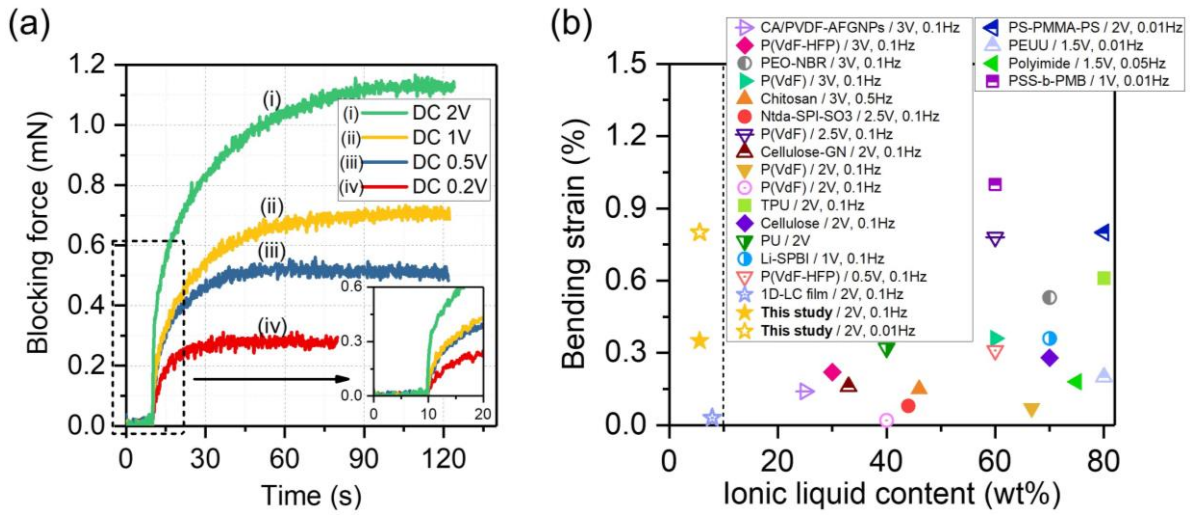

Figure 4.14 (a) Generating force of the **P_{MV}/IL(20)**-based actuator driven by various DC voltages. (b) Peak-to-peak bending strain vs ionic liquid content for an **P_{MV}/IL(20)** actuator and other, previously reported actuators.

4.3.5 Functional applications of liquid-crystalline actuators.

Taking inspiration from the locomotion of various species in nature, the development of consummate biomimetic systems including sensors and actuators is one of the trending topics that can involve our LC actuators. For example, an artificial jellyfish (**Figure 4.15 (a)**), composed of liquid-crystalline actuators attached to a silicone elastomer film containing a fluorescent dye, exhibits a graceful movement by application of a bias voltage. Moreover, **P_{MV}/IL(20)**-based actuators capable of generating an electrically controllable force can act as miniature forceps and softly hold small objects (**Figure 4.15 (b)**). Such actuators can hold an aluminum block weighing 20 mg by bending inward. They exhibit significant deformation, precise voltage response, and stable force output, and thus can be used for the development of tactile sensor arrays, artificial muscles, and soft robots.

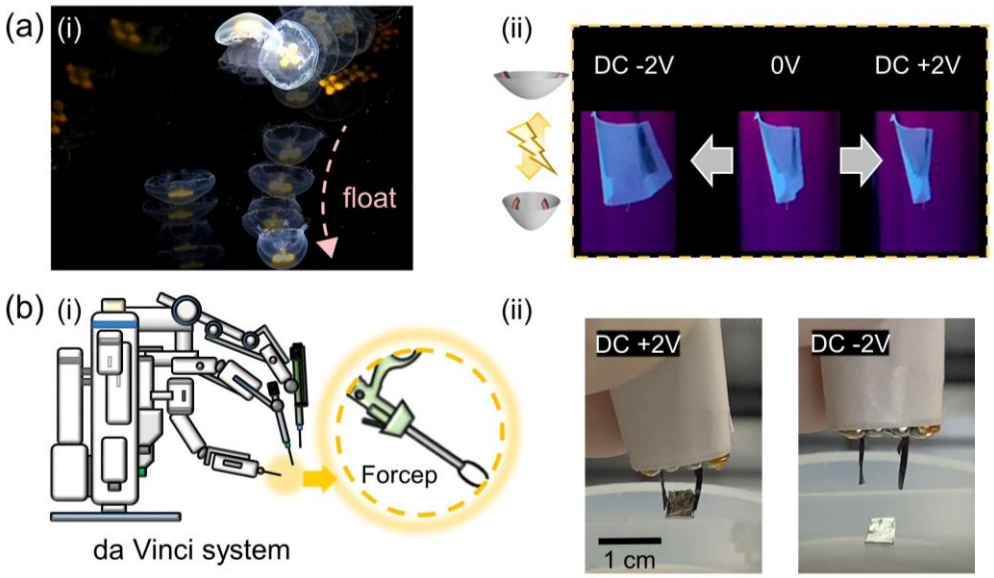

Figure 4.15 (a) Photograph of swimming jellyfish (i) and holding motion of a fluorescent dye-containing silicone elastomer film induced by bending of **P_{MV}/IL(20)**-based actuators (ii). (b) Illustration of electronically controllable miniature forceps (i) and flexible grasping and releasing of an aluminum block by two **P_{MV}/IL(20)**-based actuators (ii).

4.4 Conclusions.

In summary of this chapter, I have developed a new type of nanostructured polymer film electrolyte that contains 3D-interconnected ion transport pathways. The pathways were created through a supramolecular Col_h LC self-assembly of tapered ionic amphiphiles and a low content of ionic liquid, and subsequent photopolymerization. Phase segregation of ionic and nonionic components at the nanometer scale allows for the spontaneous formation of ion-concentrated fluidic pathways surrounding the hydrophobic nanocylinders. The columnar order significantly improves the ionic conductivity as compared to the corresponding amorphous phase, where the ions are diluted in the randomly entangled polymer matrix. Based on the efficient and fast ion migration through the 3D ionic pathways in the solid matrix, Col_h nanostructured polymer actuators with flexible **PEDOT:PSS** electrodes display good actuation performance under input voltages of 2 V in air, including a high bending strain (0.8 % at 0.01 Hz), a force generation (1.1 mN), and a long-term cycling stability. The presence of 3D ion-conductive pathways results in a significant enhancement of actuation as compared to our previous material that was based on 1D ion-conductive Col_h LC polymers, where the same ionic liquid forms cylindrical structures wrapped by insulating photo-crosslinked alkyl chains. Furthermore, I have demonstrated that our actuators can be used in soft robotic devices. The reported here methodology of designing 3D ionic pathways may be useful for developing next-generation low-voltage controllable artificial muscles and 3D-printable robots.

4.5 References.

(1) Xiao, P.; Yi, N.; Zhang, T.; Huang, Y.; Chang, Y.; Yang, Y.; Zhou, Y.; Chen, Y. Construction of a Fish–like Robot Based on High Performance Graphene/PVDF Bimorph Actuation Materials. *Adv. Sci.* **2016**, *3* (6) 1500438.

(2) Ling, Y.; Pang, W.; Li, X.; Goswami, S.; Xu, Z.; Stroman, D.; Liu, Y.; Fei, Q.; Xu, Y.; Zhao, G.; Sun, B.; Xie, J.; Huang, G.; Zhang, Y.; Yan, Z. Laser–Induced Graphene for Electrothermally Controlled, Mechanically Guided, 3D Assembly and Human–Soft Actuators Interaction. *Adv. Mater.* **2020**, *32* (17), 1908475.

(3) Li, W.; Li, F.; Li, H.; Su, M.; Gao, M.; Li, Y.; Su, D.; Zhang, X.; Song, Y. Flexible Circuits and Soft Actuators by Printing Assembly of Graphene. *ACS Appl. Mater. Interfaces* **2016**, *8* (19), 12369–12376.

(4) Must, I.; Kaasik, F.; Põldsalu, I.; Mihkels, L.; Johanson, U.; Punning, A.; Aabloo. A. Ionic and Capacitive Artificial Muscle for Biomimetic Soft Robotics. *Adv. Eng. Mater.* **2015**, *17* (1), 84–94.

(5) Umrao, S.; Tabassian, R.; Kim, J.; Nguyen, V. H.; Zhou, Q.; Nam, S.; Oh, I. K. MXene Artificial Muscles based on Ionically Cross–linked $Ti_3C_2T_x$ Electrode for Kinetic Soft Robotics. *Sci. Robot.* **2019**, *4* (33), eaaw7797.

(6) Fannir, A.; Temmer, R.; Nguyen, G. T. M.; Cadiergues, L.; Laurent, E.; Madden, J. D. W.; Vidal, F.; Plesse, C. Linear Artificial Muscle Based on Ionic Electroactive Polymer: A Rational Design for Open–Air and Vacuum Actuation. *Adv. Mater. Technol.* **2019**, *4* (2), 1800519.

(7) Li, M.; Tang, Y.; Soon, R. H.; Dong, B.; Hu, W.; Sitti, M. Miniature Coiled Artificial Muscle for Wireless Soft Medical Devices. *Sci. Adv.* **2022**, *8* (10), eabm5616.

(8) Kim, S. Y.; Cho, C.; Choi, H,; Park, H. W.; Lee, D.; Heo, E.; Park, S.; Lee, H.; Kim, D. H. Deformable Ionic Polymer Artificial Mechanotransducer with an Interpenetrating Nanofibrillar Network. *ACS Appl. Mater. Interfaces* **2019**, *11* (32), 29350−29359.

(9) Feng, G. H.; Tsai, J. W. Micromachined Optical Fiber Enclosed 4–Electrode IPMC Actuator with Multidirectional Control Ability for Biomedical Application. *Biomedical Microdevices* **2011**, *13* (1), 169–177.

(10) Feng, G. H.; Chen, R. H. Fabrication and Characterization of Arbitrary Shaped μIPMC Transducers for Accurately Controlled Biomedical Applications. *Sens. Actuators A* **2008**, *143* (1), 34−40.

(11) Kongahage, D.; Ruhparwar, A.; Foroughi, J. High Performance Artificial Muscles to Engineer a Ventricular Cardiac Assist Device and Future Perspectives of a Cardiac Sleeve. *Adv. Mater. Technol.* **2001**, *6* (5), 2000894.

(12) Terasawa, N.; Asaka, K. High–Performance Hybrid (Electrostatic Double–Layer and Faradaic Capacitor–Based) Polymer Actuators Incorporating Nickel Oxide and Vapor–Grown Carbon Nanofibers. *Langmuir* **2014**, *30* (47), 14343–14351.

(13) Mukai, K.; Asaka, K.; Hata, K.; Otero, T. F.; Oike, H. High–Speed Carbon Nanotube Actuators Based on an Oxidation/Reduction Reaction. *Chem. Eur. J.* **2011**, *17* (39), 10965−10971.

(14) Shi, Y. X.; Wu,Y.; Wang, S. Q.; Zhao, Y. Y.; Li, T.; Yang, X. Q.; Zhang, T. Soft Electrochemical Actuators with a Two–Dimensional Conductive Metal–Organic Framework Nanowire Array. *J. Am. Chem. Soc.* **2021**, *143* (10), 4017−4023.

(15) Kim, O.; Kim, S. J.; Park, M. J. Low–Voltage–Driven Soft Actuators. *Chem. Commun.* **2018**, *54* (39), 4895−4904.

(16) Kotal, M.; Kim, J.; Tabassian, R.; Roy, S.; Nguyen, V. H.; Koratkar, N.; Oh, I. K. Highly Bendable Ionic Soft Actuator Based on Nitrogen–Enriched 3D Hetero–Nanostructure Electrode. *Adv. Funct. Mater.* **2018**, *28* (34), 1802464.

(17) Liu, L.; Wang, C.; Wu, Z.; Xing, Y. Ultralow–Voltage–Drivable Artificial Muscles Based on a 3D Structure MXene–PEDOT:PSS/AgNWs Electrode. *ACS Appl. Mater. Interfaces* **2022**, *14* (16), 18150−18158.

(18) Imaizumi, S.; Kokubo, H.; Watanabe, M. Polymer Actuators Using Ion–Gel Electrolytes Prepared by Self–Assembly of ABA–Triblock Copolymers. *Macromolecules* **2012**, *45* (1), 401−409.

(19) Tianyu, W.; Wang, D.; Zhang, M.; Heflin, J. R.; Moore, R. B.; Long, T. E. RAFT Synthesis of ABA Triblock Copolymers as Ionic Liquid–Containing Electroactive Membranes. *ACS Appl. Mater. Interfaces* **2012**, *4* (12), 6552–6559.

(20) Kim, O.; Shin, T. J.; Park, M. J. Fast Low–Voltage Electroactive Actuators using Nanostructured Polymer Electrolytes. *Nat. Comm.* **2013**, *4*, 2208.

(21) Rajapaksha, C. P. H.; Feng, C.; Piedrahita, C.; Cao, J.; Kaphle, V.; Lüssem, B.; Kyu, T.; Jákli, A. Poly(ethylene glycol) Diacrylate Based Electro-Active Ionic Elastomer. *Macromol. Rapid Commun.* **2020**, *41* (6), 1900636.

(22) Cao, S.; Aimi, J.; Yoshio, M. Electroactive Soft Actuators Based on Columnar Ionic Liquid Crystal/Polymer Composite Membrane Electrolytes Forming 3D Continuous Ionic Channels. *ACS Appl. Mater. Interfaces* **2022**, *14* (38), 43701–43710.

(23) Yu, F.; Ciou, L. H.; Chen, S.; Poh, W. C.; Chen, J.; Chen, J.; Haruethai, K.; Lv, J.; Gao, D.; Lee, P. S. Ionic Covalent Organic Framework based Electrolyte for Fast–Response Ultra–Low Voltage Electrochemical Actuators. *Nat. Comm.* **2022**, *13*, 390.

(24) Imaizumi, S.; Kato, Y.; Kokubo, H.; Watanabe, M. Driving Mechanisms of Ionic Polymer Actuators Having

Electric Double Layer Capacitor Structures. *J. Phys. Chem. B* **2012**, *116* (16), 5080−5089.
(25) Wu, G.; Hu, Y.; Liu, Y.; Zhao, J.; Chen, W.; Whoehling, V.; Plesse, C.; Nguyen, G. T. M.; Vidal, F.; Chen, W. Graphitic Carbon Nitride Nanosheet Electrode–based High–Performance Ionic Actuator. *Nat. Commun.* **2015**, *6*, 7258.
(26) Kotal, M.; Kim, J.; Kim, K. J.; Oh, I. K. Sulfur and Nitrogen Co–Doped Graphene Electrodes for High–Performance Ionic Artificial Muscles. *Adv. Mater.* **2016**, *28* (8), 1610–1615.
(27) Wu, C. H.; Meng, W.; Yoshio, M. Low–Voltage–Driven Actuators Using Photo–Cross–Linked Ionic Columnar Liquid–Crystalline Polymer Films. *ACS Materials Lett.* **2022**, *4* (1), 153−158.
(28) Kim, O.; Kim, H.; Choi, U. H.; Park, M. J. One–Volt–Driven Superfast Polymer Actuators Based on Single–Ion Conductors. *Nat. Commun.* **2016**, *7*, 13576.
(29) Ichikawa, T.; Kato, T.; Ohno, H. 3D Continuous Water Nanosheet as a Gyroid Minimal Surface Formed by Bicontinuous Cubic Liquid–Crystalline Zwitterions. *J. Am. Chem. Soc.* **2012**, *134* (28), 11354−11357.
(30) Takeuchi, H.; Ichikawa, T.; Yoshio, M.; Kato, T.; Ohno, H. Induction of Bicontinuous Cubic Liquid–Crystalline Assemblies for Polymerizable Amphiphiles via Tailor–Made Design of Ionic Liquids. *Chem. Commun.* **2016**, *52* (96), 13861−13864.
(31) Taguchi, S.; Ichikawa, T.; Kato, T.; Ohno, H. Nano–Biphasic Ionic Liquid Systems Composed of Hydrophobic Phosphonium Salts and a Hydrophilic Ammonium Salt. *Chem. Commun.* **2012**, *48* (43), 5271−5273.
(32) Hudson, S. D.; Jung, H. T.; Percec, V.; Cho, W. D.; Johansson, G.; Ungar, G.; Balagurusamy, V. S. K. Direct Visualization of Individual Cylindrical and Spherical Supramolecular Dendrimers. *Science* **1997**, *278* (5337), 449–452.
(33) Smith, R. C.; Fischer, W. M.; Gin D. L. Ordered Poly(p–phenylenevinylene) Matrix Nanocomposites via Lyotropic Liquid–Crystalline Monomers. *J. Am. Chem. Soc.* **1997**, *119* (17), 4092–4093.
(34) Feng, X.; Tousley, M. E.; Cowan, M. G.; Wiesenauer, B. R.; Nejati, S.; Choo, Y.; Noble, R. D.; Elimelech, M.; Gin, D. L.; Osuji, C. O. Scalable Fabrication of Polymer Membranes with Vertically Aligned 1 nm Pores by Magnetic Field Directed Self–Assembly. *ACS Nano* **2014**, *8* (12), 11977–11986.
(35) Lugger, J. A. M.; Mulder, D. J.; Bhattacharjee, S.; Sijbesma, R. P. Homeotropic Self–Alignment of Discotic Liquid Crystals for Nanoporous Polymer Films. *ACS Nano* **2018**, *12* (7), 6714–6724.
(36) Kerr, R. L.; Miller, S. A.; Shoemaker, R. K.; Elliott, B. J.; Gin, D. L. New Type of Li Ion Conductor with 3D Interconnected Nanopores via Polymerization of a Liquid Organic Electrolyte–Filled Lyotropic Liquid–Crystal Assembly. *J. Am. Chem. Soc.* **2009**, *131* (44), 15972–15973.
(37) Nie, Z. Z.; Zuo, B.; Liu, L.; Wang, M.; Huang, S.; Chen, X. M.; Yang, H. Nanoporous Supramolecular Liquid Crystal Polymeric Material for Specific and Selective Uptake of Melamine. *Macromolecules* **2020**, *53* (11), 4204–4213.
(38) Sakamoto, T.; Ogawa, T.; Nada, H.; Nakatsuji, K.; Mitani, M.; Soberats, B.; Kawata, K.; Yoshio, M.; Tomioka, H.; Sasaki, T.; Kimura, M.; Henmi, M.; Kato, T. Development of Nanostructured Water Treatment Membranes Based on Thermotropic Liquid Crystals: Molecular Design of Sub–Nanoporous Materials. *Adv. Sci.* **2018**, *5* (1), 1700405.
(39) Gupta, M.; Suzuki, Y.; Sakamoto, T.; Yoshio, M.; Torii, S.; Katayama, H.; Kato, T. Polymerizable Photocleavable Columnar Liquid Crystals for Nanoporous Water Treatment Membranes. *ACS Macro Lett.* **2019**, *8* (10), 1303–1308.
(40) Suzuki, Y.; Sakamoto, T.; Yoshio, M.; Kato, T. Development of Functional Nanoporous Membranes based on Photocleavable Columnar Liquid Crystals–Selective Adsorption of Ionic Dyes. *Eur. Polym. J.* **2020**, *134*, 109859.
(41) Yoshio, M.; Mukai, T.; Ohno, H.; Kato, T. One–Dimensional Ion Transport in Self–Organized Columnar Ionic Liquids. *J. Am. Chem. Soc.* **2004**, *126* (4), 994–995.
(42) Ichikawa, T.; Yoshio, M.; Hamasaki, A.; Mukai, T.; Ohno, H.; Kato, T. Self–Organization of Room–Temperature Ionic Liquids Exhibiting Liquid–Crystalline Bicontinuous Cubic Phases: Formation of Nano–Ion Channel Networks. *J. Am. Chem. Soc.* **2007**, *129* (35), 10662–10663.
(43) Luo, S.; Sun, S.; Deorukhkar, A. R.; Lu, J. T.; Bhattacharyya, A.; Lin, I. J. B. Ionic Liquids and Ionic Liquid Crystals of Vinyl Functionalized Imidazolium Salts. *J. Mater. Chem.* **2011**, *21* (6), 1866–1873.
(44) Yoshio, M.; Kagata, T.; Hoshino, K.; Mukai, T.; Ohno, H.; Kato, T. One–Dimensional Ion–Conductive Polymer Films: Alignment and Fixation of Ionic Channels Formed by Self–Organization of Polymerizable Columnar Liquid Crystals. *J. Am. Chem. Soc.* **2006**, *128* (16), 5570–5577.
(45) Mukai, K.; Asaka, K.; Sugino, T.; Kiyohara, K.; Takeuchi, I.; Terasawa, N.; Futaba, D. N.; Hata, K.; Fukushima, T.; Aida, T. Highly Conductive Sheets from Millimeter–Long Single–Walled Carbon Nanotubes and Ionic Liquids: Application to Fast–Moving, Low–Voltage Electromechanical Actuators Operable in Air. *Adv. Mater.* **2009**, *21* (16), 1582−1585.
(46) Xia, Y.; He, Y.; Zhang, F.; Liu, Y.; Leng, J. A Review of Shape Memory Polymers and Composites: Mechanisms, Materials, and Applications. *Adv. Mater.* **2021**, *33* (6), 2000713.

Chapter 5

Mechanically Tough Micellar Cubic Liquid-Crystalline Polymer Electrolytes for Electromechanical Actuators

5.1 Introduction.

Ionic electroactive polymer (iEAP) actuators have attracted considerable attention as a practical tool for energy storage and transduction. iEAP actuators exhibit remarkable advantages in low driving voltage, large deformation, controllable generation force, and lightweight, which can be used to develop soft electronic devices with precise manipulation.[1] At present, most high-performance iEAP actuators exhibit good bending deformation by using functionalized materials comprising a large amount of ionic liquid, but they often ignore the generation force.[2–6] To construct an iEAP actuator that simultaneously perform high deformation and generation force, the nanoscale morphologies within the ionic polymer electrolytes endow a large specific surface area and ordered nanostructure, which furnish the opportunity to control the mechanical property and effectively enhance the ion transport. Despite a rich assortment of nanostructured polymer electrolytes being well-behaved at iEAP actuators,[7,8] the lack of mechanical properties caused by physical-cross-linked polymer electrolytes and unnecessary plasticization from excess ionic liquids has not been fully addressed.

A convincing approach is to construct three-dimensional (3D) periodic cubic structures within polymer electrolytes.[9] Periodic cubic structure is formed by a microphase separation of amphiphilic molecules which divides space into two interwoven and continuous networks. The free ions within the periodic nanostructure can diffuse in 3D open space without being hindered by any boundary layer. Namely, the ion conductive pathways exhibit low tortuosity in 3D cubic structure as compared to inner conductive columnar and layer structures.[10,11] Meanwhile, the cubic lattices render higher viscoelastic behavior that benefits the improvement of modulus.[9,12] Among the various periodic cubic structures, micelles cubic with spherical symmetry (Cub_M) composed by the hydrophobic sphere wearing a hydrophilic shell is the most common case in various lyotropic systems.[13,14] However, strategies to construct these regular Cub_M by self-assembled block copolymers often require cautious investigation of their abstruse thermodynamic behavior and selection of suitable functional monomers.[15–18] In order to overcome the immediate dilemma in structural design for the new iEAP actuator, I found the photocured ionic liquid-crystalline (LC) membrane with nanoscale ion channels was a highly desirable candidate. By leveraging the influence of molecular shape and

interaction on self-assembled ionic liquid crystals, it is possible to effectively control the resulting morphologies, and subsequent polymerization to obtain freestanding LC membranes. I have reported several nanostructured LC membrane-based actuators with hexagonally packed columnar (Col_h), and layered morphology (Sm) exhibit good bendability under low ionic liquid content (< 15 wt%), although they only show 1D or 2D connectivity, respectively. In addition, I have proposed a new design concept for 3D Col_h structure consisting of the ionophobic cylinder surrounded by ionic shells. This concept constructs a substitution scheme that resembles a cubic structure due to the formation of interconnected ionic domains between each LC column. However, the orientation of such LC columns in the membrane still has a tiny impact on their mechanical property and ionic conductivity. The Cub_M structures offer a way to achieve an intuitive alignment-free structure and mechanical toughness that is necessary to overcome the present arguments.

In this study, I advance a new taper-shaped ionic LC monomer (**Vc12**) to construct the well-defined thermotropic Cub_M LC structure. The **Vc12** consists of two vinyl imidazole groups and a single alkyl chain (**Figure 5.1 (a)**), in which the alkyl chain act as a key role in the stability of the LC mesophase. The mixture of **Vc12** and **IL** exhibits a wide temperature range of Col_h and Cub_M phases with interconnected polar domains (**Figure 5.1 (b)**). Subsequent polymerization can obtain a mechanically tough LC electrolyte presented of ordering Cub_M nanostructure. Therefore, the mobile ion was able to pass along the spherical surface with positive interfacial curvature to efficiently migrate inside the membrane. Such flexible LC electrolyte with Cub_M structure exhibits competitive superiority in alignment-free manufacture and high viscoelasticity as compared to the other polymer electrolytes. The Cub_M based electrolyte sandwiched between conductive **PEDOT:PSS** electrodes (**Figure 5.1 (c)**) can simultaneously achieve high bending strain (0.63 %) and high blocking force (2.7 mN) under low input voltage (± 2 V, 0.1 Hz), as well as stable operating ability in the air (> 10,000 cycles). To the best of our knowledge, I have proposed the first example of a mechanically tough thermotropic Cub_M LC membrane electrolyte that successfully applied in energy storage and transduction device.

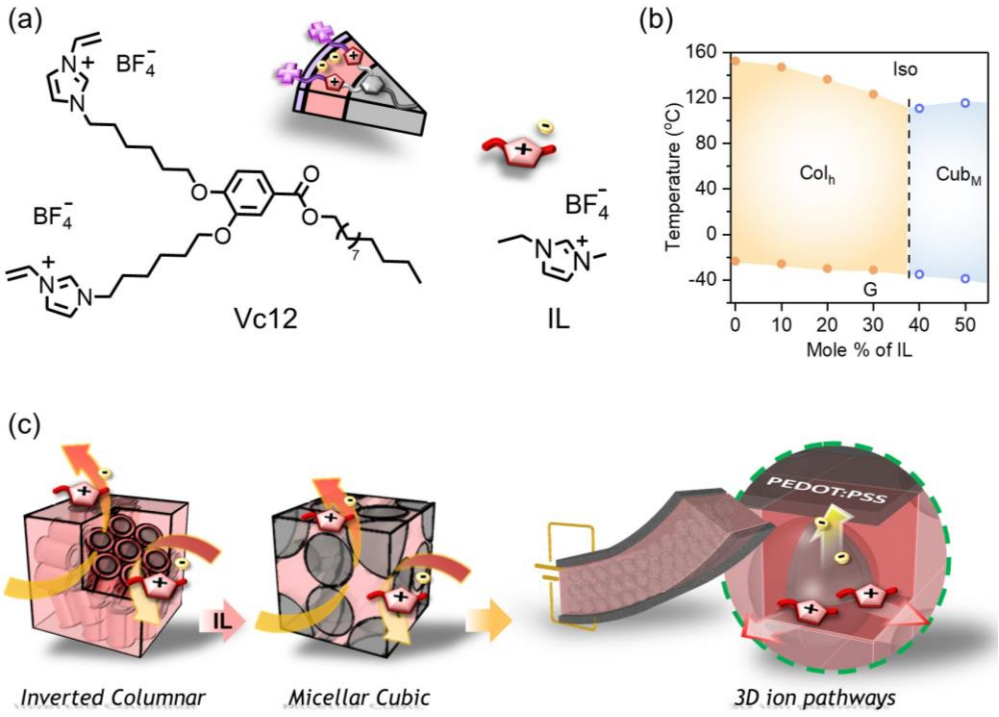

Figure 5.1 (a) Molecular structures of taper-shaped ionic LC monomer **Vc12** and ionic liquid [EMIM][BF_4] (**IL**). (b) Phase-transition temperature of the binary mixture of **Vc12** and **IL** as a function of the mole% of **IL**. G, Col_h, Cub_M and Iso are glassy, hexagonal columnar, micellar cubic, and isotropic liquid phases, respectively (c) The scheme illustrates that the transformation of the Col_h phase to Cub_M phase by further addition of **IL**, followed by applying photo-polymerization can obtain the polymer film. The Cub_M LC membrane-based actuator has unimpededly 3D ionic pathways at the spacing of the alignment-free spherical structure.

5.2 Experimental Section.

5.2.1 Materials.

1–Dodecanol (>99%), 4–Dimethylaminopyridine (DMAP, >99%), 1–(3–Dimethylaminopropyl)–3–ethylcarbodiimide (EDC, >98%), 1–Vinylimidazole (>98%), 1–Ethyl–3–methylimidazolium tetrafluoroborate (**IL**, >99%), Silver tetrafluoroborate ($AgBF_4$, >98%) were purchased from Tokyo chemical industry. 2,6–*di*–*tert*–butyl–4–methoxyphenol (Inhibitor, 98%), Ethylene glycol were purchased from KANTO CHEMICAL. Poly(3,4–ethylene dioxythiophene) polystyrene sulfonate **PEDOT:PSS** (Clevios™ PH1000) was purchased from Heraeus. 2,2–dimethoxy–2–phenylacetophenone as a photo-initiator was purchased from Sigma-Aldrich. All the chemicals were used directly without further purification.

5.2.2 Synthesis of ionic amphiphilic (Vc12).

The detailed synthesis route, procedures, and their nuclear magnetic resonance (NMR) spectra were written in ***Appendix 7.4***.

5.2.3 General methods.

Rheological measurements were performed using an Anton Paar MCR 102 rheometer (Anton Paar, Austria). A parallel plate geometry with an 8 mm diameter plate and a gap spacing of 0.3 mm were used for all the measurements. The measurements were conducted at an angular frequency of 10 rad s^{-1} and a shear strain amplitude of 0.01%-1000%. Small-angle X-ray scattering (SAXS) measurements were performed by using Anton Paar SAXSess mc^2 instruments. Polarized optical microscopy (POM) observations, differential scanning calorimetry (DSC) measurements, cyclic voltammetry (CV) measurements, ionic conductivity measurements, and actuation tests were performed using the same equipment and methods as described in the previous Chapter.

5.2.4 Fabrication of liquid-crystalline actuators.

The mixture of **Vc12** and 0.1 wt% photo-initiator (2,2–dimethoxy–2–phenylacetophenone) with the proper amount of the [EMIM][BF_4] ionic liquid (**IL**) was dissolved in a mixed solution of chloroform/methanol (4/1 in volume). The solvents were removed by rotary evaporator under light-resistant conditions. The residue was dried

under vacuum at 30 ºC for 1 day to give the liquid-crystalline sample of **Vc12/IL(x)** (Samples represented as **x** mol% **IL** in the mixtures). The monomeric sample **Vc12/IL(x)** was placed between the glass and a glass substrate covered with polyimide (PI) tape. The thickness of the sample was fixed using a polyimide (PI) tape spacer. The sandwiched cell was heated to a temperature at which the sample became the isotropic liquid state and then cooled to room temperature to form the liquid-crystalline nanostructure. Subsequently, the cell was irradiated with UV light (365 nm, 5 mW/cm^2) for 5 minutes at room temperature. After polymerization, the **Vc12/IL(x)** membrane was carefully peeled off from the substrate. The polymeric membrane was sandwiched between a pair of **PEDOT:PSS** sheet and heat-press to afford liquid-crystalline actuator. (Samples represented as **P_{Col}/IL(30)** was 30 mol% **IL** confined in columnar nanostructured membranes, and **P_{Cub}/IL(40)** was 40 mol% **IL** confined in micellar cubic nanostructured membranes.)

Table 5.1 The ingredient of the binary mixture composed of the ionic liquid-crystalline monomer (**Vc12**) and ionic liquid (**IL**).

	Mole fraction		**Weight fraction**	
	Vc12 (mol%)	**IL (mol%)**	**Vc12 (wt%)**	**IL (wt%)**
P_{Col}/IL(0)	100	0	100	0
P_{Col}/IL(30)	70	30	90.9	9.1
P_{Cub}/IL(40)	60	40	86.6	13.4

5.3 Results and Discussion.

5.3.1 Liquid-crystalline structure and ion conductive property.

The characteristic of polymerizable LC molecule **Vc12** exhibits stabilized Col_h packed structure from -23.5 ºC to 152.6 ºC (**Figure 5.1 (b)**). The polarizing optical microscope (POM) graph shows the irregular fan texture with some black regions (**Figure 5.2 (a)**, upper panel), which indicates the combined texture of random and vertical orientation of the LC columns. The Small-angle X-ray scattering (SAXS) pattern can observe the three scattering peaks at q = 1.29, 2.24, and 2.59 nm^{-1}, which can be indexed to the (100), (110) and (200) reflection of the Col_h structure (**Figure 5.2 (a)**). The intercolumnar distance was estimated to 5.6 nm. By further addition of the **IL**, the phase transition temperature from Col_h to isotropic liquid (Iso) states was gradually decreased and turned to the Cub_M structure when the **IL** content was up to 40 mol%. The POM texture exhibits no birefringence optical image and high viscosity which can be surmised as the Cub_M phase formed (**Figure 5.2 (b)**, upper panel). The Col_h-Cub_M structure transition was mainly caused by the expanded rearrangement of ionophilic moiety in LC systems. The lattice parameter of Cub_M structure can determine from SAXS pattern (**Figure 5.2 (b)**). Three obvious scattering at q = 1.03, 1.16, and 1.27 nm^{-1}, and tiny peaks at q = 1.65, 1.92, and 2.13 nm^{-1} are observed. The reciprocal spacing ratio of these peaks can be speculated to $\sqrt{4}$:$\sqrt{5}$:$\sqrt{6}$:$\sqrt{10}$:$\sqrt{14}$:$\sqrt{16}$, which can be assigned to (200), (210), (211), (310), (321) and (400) reflections of the Cub_M phase with $Pm\bar{3}n$ symmetry.[19]

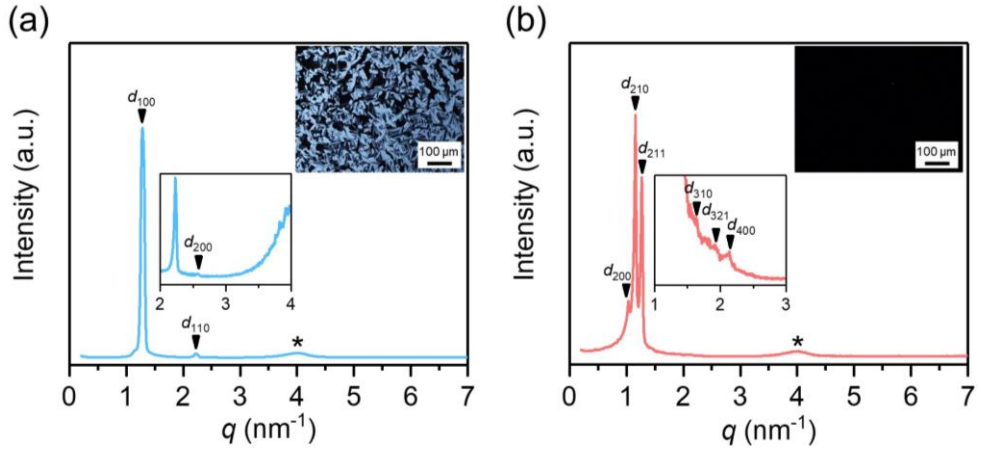

Figure 5.2 SAXS profiles of (a) **Vc12**, and (b) **Vc12/IL(40)**. The insets magnify selected regions, and their corresponding POM graphs were shown in the upper panels. (*) is attributed to the reflection of Kapton.

The morphologies transition of the Col_h and Cub_M phases observed in **Vc12/IL(x)** mixture when the **IL** contents were up to 30 mol% and 40 mol%. The structure transition of Col_h and Cub_M phases can be further investigated by dynamic rheological analysis. **Figure 5.3 (a)** shows the shear viscosity of the **Vc12/IL(30)** mixture as a Col_h sample, and **Vc12/IL(40)** mixture as a Cub_M sample. The **Vc12/IL(40)** shows six times higher viscosity than **Vc12/IL(30)** at a shear rate of 0.01 s^{-1}. A conspicuous drop stage was observed on Cub_M sample at the shear rate above 70 s^{-1}, which might be attributed to the collapse of the Cub_M structure. The relationship between dynamic modulus and shear strain for **Vc12/IL(30)** and **Vc12/IL(40)** was shown in **Figure 5.3 (b)**. Both the Col_h and Cub_M structures exhibit viscoelastic behavior, in which the storage modulus G' (elastic behaviors) prevails over the loss modulus G'' (plastic behavior) at a low shear strain region (shear strain γ < 10%). This result reveals the physical structure of LC phases presents the illiquidity gel character, while the Cub_M phase was provide with five times higher G' than Col_h phase. In addition, the Cub_M phase also shows the postponed intersects point on G' and G'' curves as compared with the Col_h phase, which means that the Cub_M structure has good morphologies stability. This high viscosity micellar cubic structure has the stable physical structure which can be illustrated by an apparent intact plateau in the angular frequency sweep measurement at a fixed shear strain (**Figure 5.4**). The thixotropic measurement for Cub_M structure exhibits good repairability than Col_h structure under alternating applied oscillatory strain of 500% and 1% (**Figure 5.5**). Such presented excellent dynamic modulus of low molecular weight thermotropic Cub_M structure, consisting of only LC monomer **Vc12** and plasticizer **IL**, was comparable to the lyotropic Cub_M material,[20] block copolymer Cub_M gel,[21] and LC copolymer dendrimer with Cub_M structure.[9]

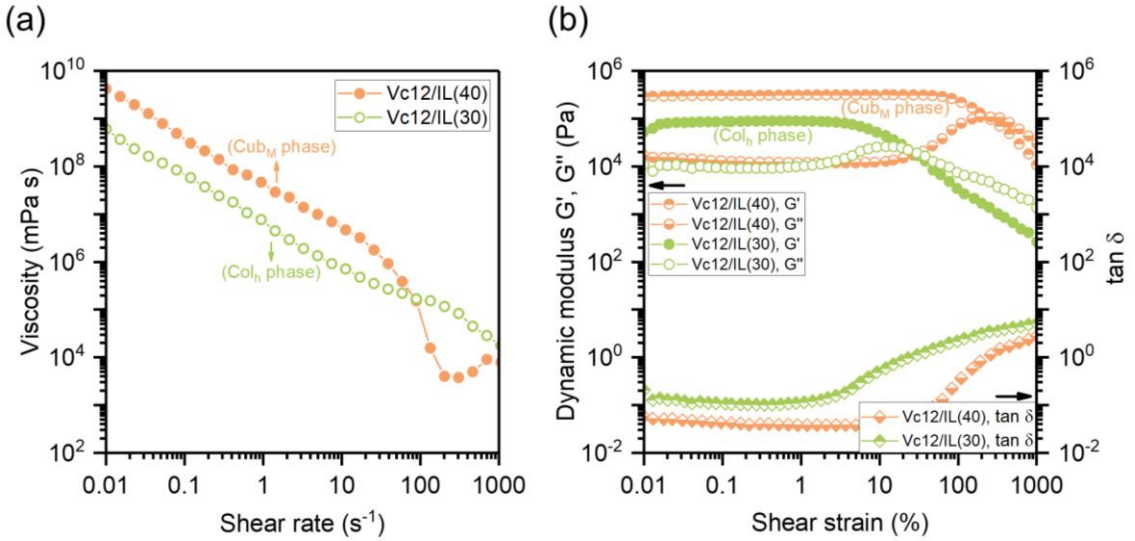

Figure 5.3 (a) Shear viscosity for LC mixture in Col_h and Cub_M phases. (b) dynamic modulus and tan δ of **Vc12/IL(30)** (Col_h sample, green symbols) and **Vc12/IL(40)** (Cub_M sample, orange symbols) mixtures as the function of the oscillatory strain amplitude. The G' = storage modulus (Pa), and G'' = loss modulus (Pa).

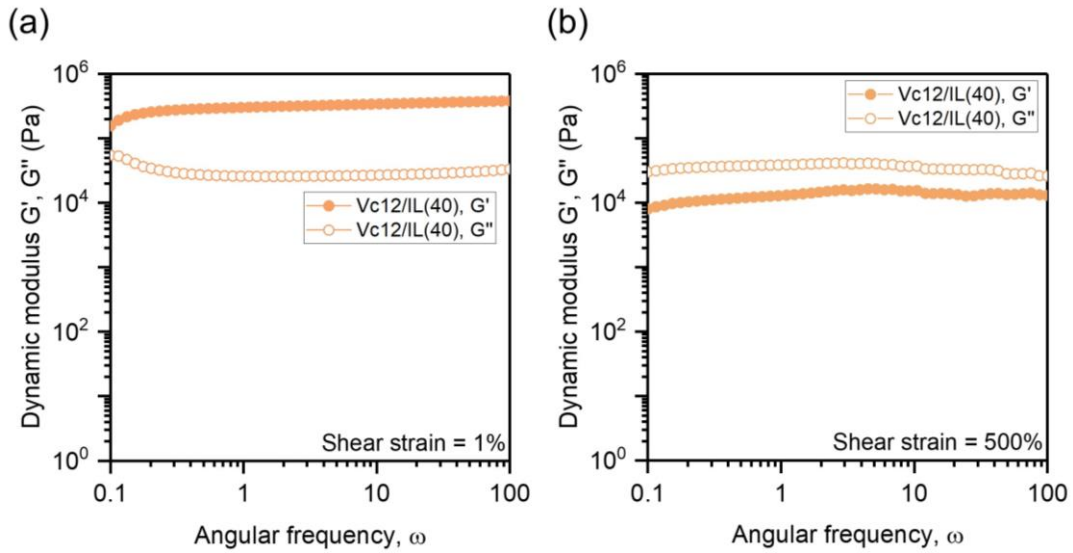

Figure 5.4 Dynamic modulus versus angular frequency for **Vc12/IL(40)** mixture at a fixed shear strain of (a) 1%, and (b) 500%. The G' = storage modulus (full circle, Pa), and G'' = loss modulus (open circle, Pa).

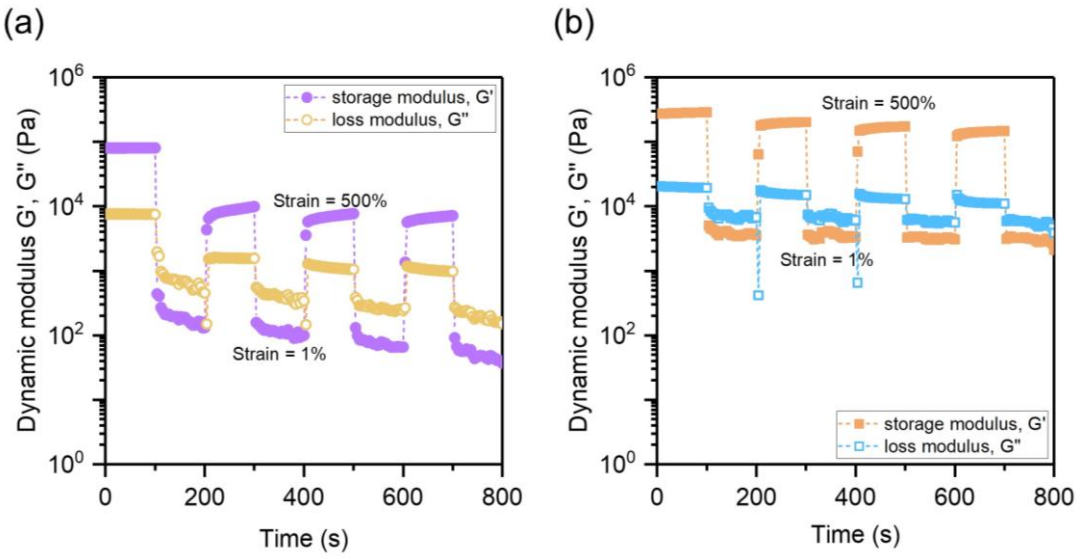

Figure 5.5 Thixotropic measurement of (a) **Vc12/IL(30)** as a Col_h sample, and (b) **Vc12/IL(40)** as a Cub_M sample. The shear strain was changed to 500% and 1% every 100 seconds at a fixed angular frequency of 10 rad/s at 25 °C. The G' = storage modulus (full symbol, Pa), and G" = loss modulus (open symbol, Pa).

The ionic conductivity of **Vc12** shows 1.62×10^{-6} S/cm at 25 ºC. By increasing the temperature, the ionic conductivity gradually increased which can be illustrated by Arrhenius behavior. While the corresponding activation energy from the temperature range of 25 ºC to 100 ºC was estimated to 69 kJ/mol. I have also determined the LC column structure by the molecular alignment in comb-shaped gold electrode (**Figure 5.6**). The orientation of the LC column was controlled by the mechanical shearing between a pair of gold electrodes. As shown in **Figure 5.6 (c)**, the parallel columnar arrangement ($\sigma_{//}$) shows a tiny enhancement in conductivity than random (σ) and perpendicular alignment ($\sigma_{\perp}$). The corresponding anisotropy ratio ($\sigma_{//}/\sigma_{\perp}$) is about 2.2, which was smaller than traditional Col_h LC materials with inner ion channels ($\sigma_{//}/\sigma_{\perp} > 10$-100). This result supported that the ion conductive part was located in the outer layer of the column and connected with each other to form the 3D continuous ionic pathways. This concept also elucidated that the rational design concept on intuitively inverted polar domain within LC columnar structures formed by our new LC monomer. In addition, the Cub_M structure containing 40 mol% **IL** exhibits uniform conductivity under any direction that supported the concept of inverted spherical ionic regions within LC phase (**Figure 5.6 (b)(c)**), meanwhile, a good conductivity of 9.15×10^{-5} S/cm with an activation energy of

38 kJ/mol can be obtained. As the related issues involving LC domain size and alignment can be disregarded, the Cub_M structure possesses potential advantages in alignment-independence ion pathways that provide convenience in material fabrication and application.

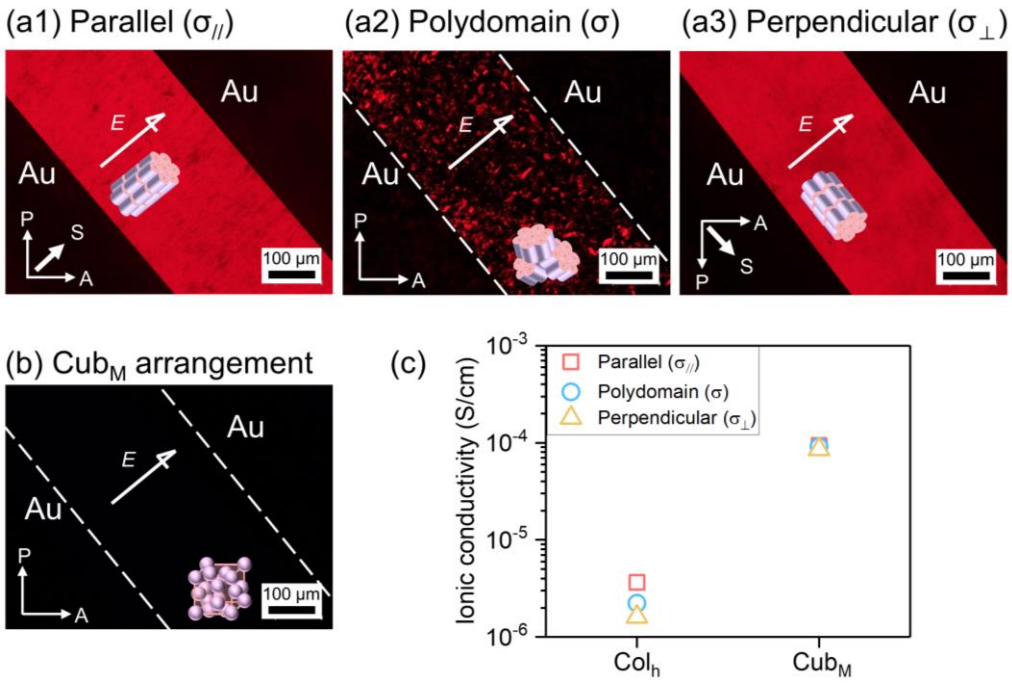

Figure 5.6 Molecular alignment and ionic conductivity of **Vc12** in Col_h phase and **Vc12/IL(40)** in Cub_M phase. Polarized optical micrographs for different molecular orientations: Col_h structure in (a1) columnar axes are parallel to electric field ($\sigma_{//}$), (a2) polydomain region (σ), (a3) columnar axes are perpendicular to electric field ($\sigma_{\perp}$), (b) no birefringence Cub_M phase between gold electrode cells. Arrows indicate the directions of the mechanical shear force (*S*), analyzer (*A*), polarizer (*P*), and electric field (*E*). (c) Alignment-controlled ionic conductivity (parallel direction: $\sigma_{//}$, □; polydomain: σ, ○; perpendicular direction: $\sigma_{\perp}$, △).

5.3.2 Characterization of ion conductive liquid-crystalline polymer films.

The **Vc12/IL** mixture containing 0.1 wt% photo-initiators can be polymerized by exposing UV light (350 nm; 5 mW cm^{-1}). The freestanding LC films remaining Col_h and Cub_M nanostructure can be easily peeled off from the substrates. SAXS profiles of **P_{Col}/IL(30)** film observed the scattering of d_{100}, d_{110} and d_{200} (**Figure 5.7 (a)**). This result supported that the Col_h ordering can maintained in the membrane and the intracolumnar distance of about 5.65 nm. In addition, **P_{Cub}/IL(40)** film shows scattering of d_{200}, d_{210}, and d_{211} planes (**Figure 5.7 (b)**). The lattice constant of cubic film was calculated as 11.7 nm. The optical transparent Cub_M LC film exhibits good ionic conductivity at room temperature (**Figure 5.8 (a)**). For example, **P_{Col}/IL(30)** film shows about one order higher ionic conductivity than **P_{Col}/IL(0)** film. However, **P_{Cub}/IL(40)** film has only a 10 mol% difference in **IL** with **P_{Col}/IL(30)** film, but the ionic conductivity was greatly enhanced from 1.44×10^{-6} to 4.78×10^{-5} S/cm. The activation energies were calculated as 74, 59, and 35 kJ/mol corresponding to **P_{Col}/IL(0)**, **P_{Col}/IL(30)**, and **P_{Cub}/IL(40)** electrolyte films, respectively. Such improvement of ionic conductivity was mainly caused by the ordering micellar arrangement and more **IL** confined in the membrane. DSC thermograms show the glass transition temperature (T_g) from -14 to -31 °C by the increase of **IL** contents. It is worth noting that the **P_{Col}/IL(30)** and **P_{Cub}/IL(40)** films have similar T_g (-29 °C and -31 °C), although the molar contents of **IL** as the plasticizer have 10 mol% difference.

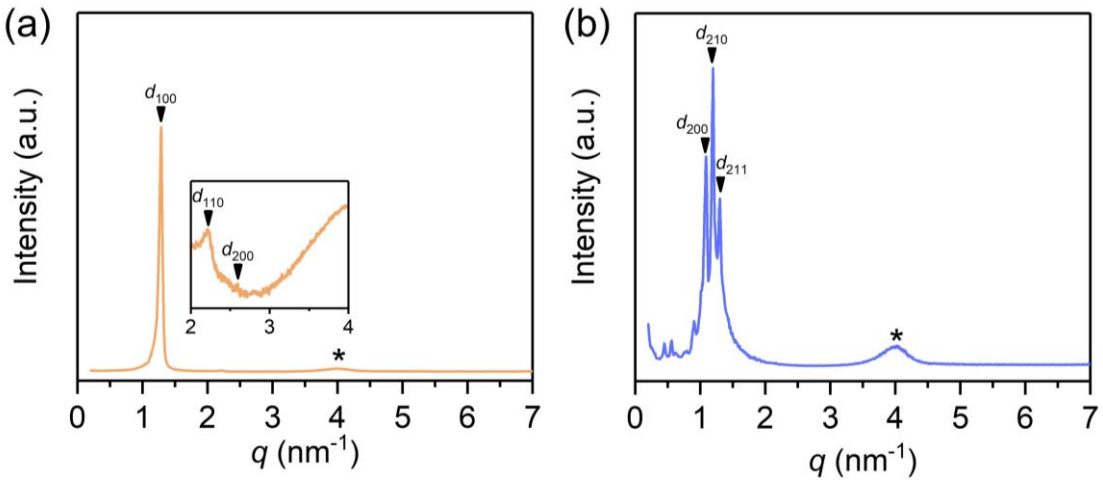

Figure 5.7 SAXS profiles for the polymeric membranes of (a) **P_{Col}/IL(30)**, and (b) **P_{Cub}/IL(40)**. The insets magnify selected regions. (*) is attributed to the reflection of Kapton.

5.3.3 Electroactive actuation for ionic liquid-crystalline actuators.

I herein show the bending actuation of **P_{Cub}/IL(40)**-based actuator, in which the actuator was prepared from the Cub_M LC membrane sandwiched between two sheets of conductive **PEDOT:PSS** electrodes. By applying the voltage, the ions can quickly move along the inverse spherical pathways and aggregate on the electrodes to induce material bending. This is due to the high ionic conductivity and low activation energy arise from the low tortuosity of ion pathways in Cub_M LC structure. The maximum displacement of **P_{Cub}/IL(40)**-based actuator exhibits about 19 mm and 3 mm under the alternating current (AC) of 2 V with 0.1 and 1 Hz, respectively (**Figure 5.8 (b)**). I have investigated the LC actuators with Col_h and Cub_M structures, respectively, while both of them have the similar structures of 3D ionic pathways. The frequency dependence of the bending strain was shown in the **Figure 5.8 (c)**. **P_{Cub}/IL(40)**-based actuator demonstrated a higher bending strain of 0.63 % than **P_{Col}/IL(30)**-based actuator with a 0.35 % value under 2 V, 0.1 Hz.

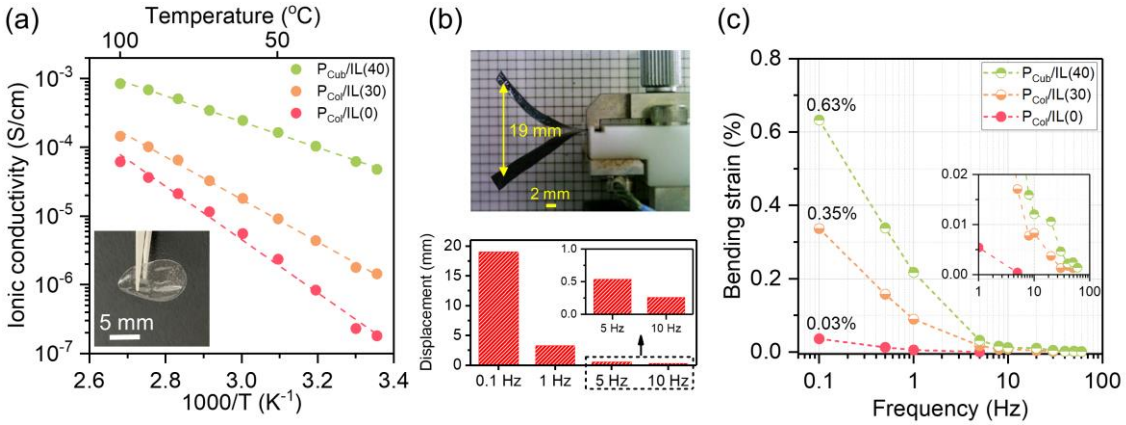

Figure 5.8 (a) Ionic conductivities of **P_{Col}/IL(0)**, **P_{Col}/IL(30)** and **P_{Cub}/IL(40)** films. The insert image shows appearance of **P_{Cub}/IL(40)** film. (b) The upper panel shows bending actuation of **P_{Cub}/IL(40)**-based actuator. The lower panel shows maximum displacement of **P_{Cub}/IL(40)**-based actuator with various frequency. (c) Frequency dependence of the bending strain of the **P_{Col}/IL(0)**, **P_{Col}/IL(30)** and **P_{Cub}/IL(40)**-based actuators under an AC voltage of 2 V.

To explore the outstanding performance from LC actuators, I observed a high-frequency oscillation of 60-70 Hz in **P_{Cub}/IL(40)**-based actuator under an AC 1 V and 2 V. It is great than other actuators made from block copolymer, amorphous polymer

electrolyte materials. It is worth noting that the **P_{Cub}/IL(40)** membrane contains only 13.3 wt% ionic liquid, which is much lower than the other reported high-performance actuators. Apart from this, I found the **P_{Col}/IL(0)**-based actuator without **IL** was able to induce the tiny deflection with 0.03 % strain at 2 V and 0.1 Hz. This is mainly caused by the net anion (BF_4) motion within the polarization of the LC network. The bending behavior induced by only anion illustrated a tiny current generated within the actuator, which was a sharp contrast with **P_{Col}/IL(30)** and **P_{Cub}/IL(40)**-based actuators. The bending actuation behavior through ion accumulation at the electrode interface was further investigated by cyclic voltammetry (CV) measurement. The current flow within **P_{Cub}/IL(40)** and **P_{Col}/IL(30)**-based actuators exhibit electric double layer capacitance behavior at a potential window of -1 V to 1 V (**Figure 5.9 (a)**). **P_{Cub}/IL(40)**-based actuator reveals the specific capacitance of around 17.9 mF/cm^2 at a scan rate of 10 mV/s, and **P_{Col}/IL(30)**-based actuator shows 15.1 mF/cm^2 (**Figure 5.9 (b)**). This slight difference between these two actuators might cause by the ion content in the electrolyte layer, although they are different nanostructures, but both compose the 3D ion transport pathways.

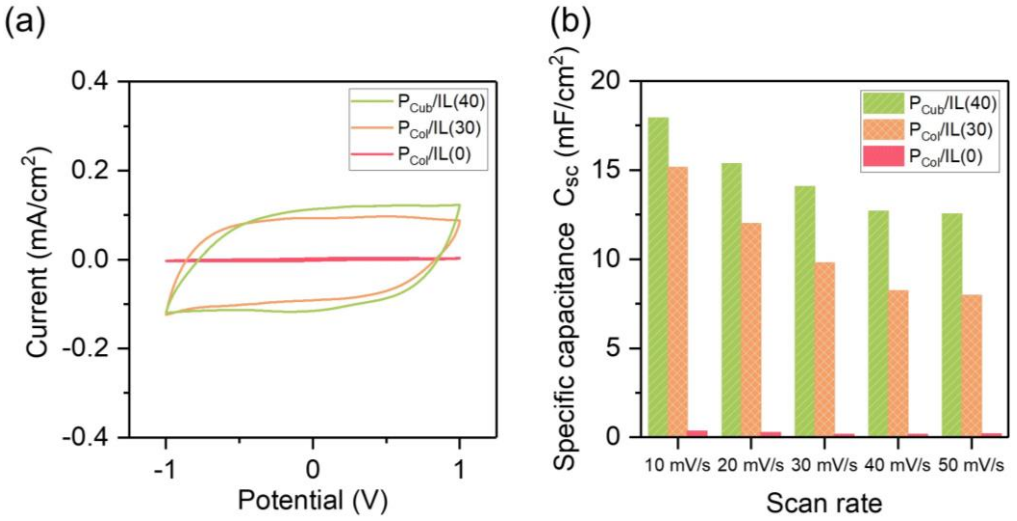

Figure 5.9 (a) The cyclic voltammograms for **P_{Col}/IL(0)**, **P_{Col}/IL(30)** and **P_{Cub}/IL(40)**-based actuators at the scan rate of 10 mV/s. (b) Calculated specific capacitances (C_{sc}) at different scan rates.

5.3.4 Generation force and mechanical characteristics of liquid-crystalline actuators.

To demonstrate the good actuation performance of cubic LC electrolyte-based actuator, I expected the mechanically tough cubic LC electrolyte can act as a key role to provide higher bending force than the columnar LC electrolyte-based actuator. Generation force was evaluated from the bending actuators in the AC voltage of 2 V at 0.1 Hz. **P_{Cub}/IL(40)**-based actuator was able to generate a blocking force of 2.7 mN, where this force was estimated to be about 60 times higher than its own weight. However, **P_{Col}/IL(30)**-based actuator only shows 0.96 mN under the same condition (**Figure 5.10 (a)**). The generation force of **P_{Col}/IL(30)**-based actuator was not comparison to **P_{Cub}/IL(40)**-based actuator that might cause by the moment of inertia produced by the deformed actuators and their own intrinsic elastic modulus. From the point of inertia moment, the **P_{Cub}/IL(40)**-based actuator has a larger inertia moment than **P_{Col}/IL(30)**-based actuator due to the good bending motion. Thus, **P_{Cub}/IL(40)**-based actuator demonstrates the high bending speed that was able to contribute to the enhancement of kinetic energy. On the other hand, Young's modulus (E) of these LC actuators was evaluated by using the dynamic tensile test (**Figure 5.10 (b)**). The tensile strain-stress curves exhibit a similar trend on these assembled actuators composed of **P_{Col}/IL(30)** and **P_{Cub}/IL(40)** electrolytes, respectively, and a pair of **PEDOT:PSS** electrodes. Thus, Young's modulus was obtained from the slope in the initial curve within the 0.5 % strain was estimated to be 409 and 466 MPa for **P_{Col}/IL(30)** and **P_{Cub}/IL(40)**-based actuators, respectively. Although some part of mechanical properties was attributed to the selection of the thickness on **PEDOT:PSS** electrodes, the elasticity of the whole actuator can be dominated through the electrolyte layer under the same thickness condition. **P_{Cub}/IL(40)** electrolyte enabling the improvement in the elasticity might attribute to the tightly stacking of the micellar spherical structure in an unit space, which could also evidence from its storage modulus (G') on the monomeric mixture from the rheological measurement. By contrast, **P_{Col}/IL(30)** electrolytes with randomly LC column orientation might have free space between each LC column, leading to lower mechanical properties than **P_{Cub}/IL(40)** electrolyte.

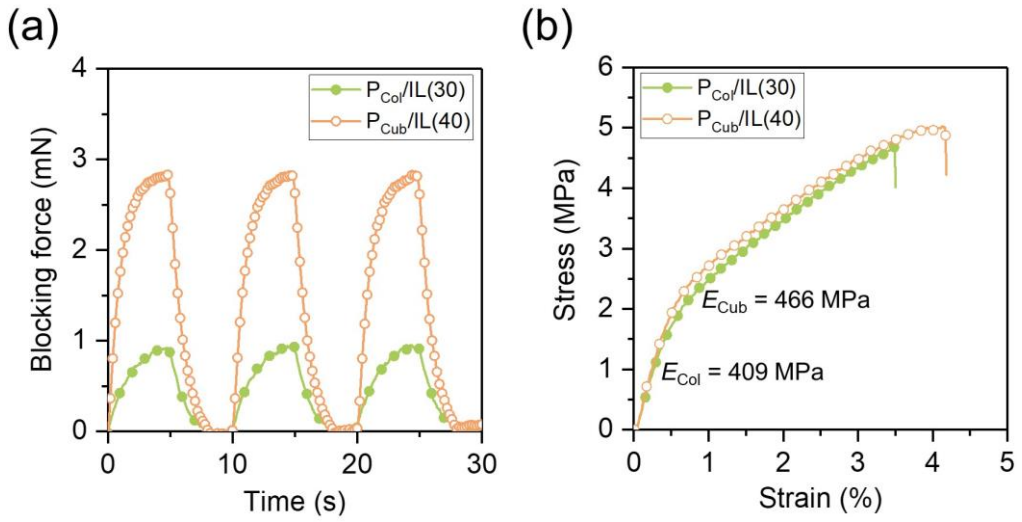

Figure 5.10 (a) Generation force from bending actuators based on **P_{Col}/IL(30)** and **P_{Cub}/IL(40)** electrolytes, respectively, under AC 2 V and 0.1 Hz. (b) Tensile stress-strain curve of **P_{Col}/IL(30)** and **P_{Cub}/IL(40)**-based actuators.

I have investigated the force distribution produced from the bending **P_{Cub}/IL(40)**-based actuator, in which the actuator has a dimension of 20 mm in free length, 8 mm in width, 180 μm in thickness, and the weight is 42 mg (**Figure 5.11 (a)**). Upon supplying a DC voltage of 2 V, the maximum generation force of 4 mN was recorded at the actuator tip. Moreover, in accordance with the classical lever rule, the generated force on the actuator significantly improves as the distance from the fulcrum clip is reduced. As such, the forward position at the middle of the actuator can generate over four times the blocking force compared to the actuator tip. This significant generation force from the flexible **P_{Cub}/IL(40)**-based actuator can hold up a 1.5 g aluminum block in equilibrium under a DC voltage of 2 V (**Figure 5.11 (b)**). Notably, the weight of the block is approximately 40 times over than the actuator. Although excellent generation force can be achieved by stacking multiple layers of electrolytes to fabricate actuator, this approach comes at the cost of sacrificing the intrinsic benefits of flexibility and high bending displacement on the actuator. Additionally, it can lead to increased electric resistance between each electrolyte interface. Thanks to the ingenious design principle of tough cubic LC electrolyte, the salient features of utilization this single-layer membrane electrolyte was able to realize flexibility, mechanically strong, high blocking force, and good bending motion in the actuator. I also demonstrated the effectiveness of an electronic

pincer made from two sheets of **P_{Cub}/IL(40)**-based actuators. The lightweight actuator exhibits a remarkable bending performance to securely grasp a styrofoam block (**Figure 5.11 (c)**). Hence, our newly designed cubic LC electrolytes can simultaneously perform efficient physical elastic deformation and ion transport, resulting in excellent performance for soft actuator applications.

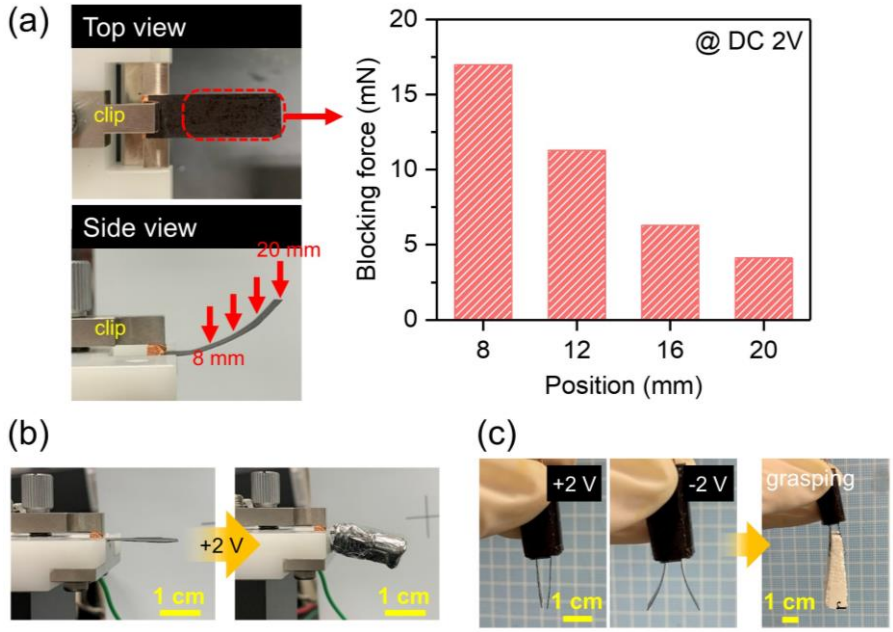

Figure 5.11 (a) The top-view and side-view of the bending **P_{Cub}/IL(40)**-based actuator, and resulting force at different positions on the actuator by supplied a DC voltage of 2 V. (b) A 1.5 g aluminum block could be carried by using **P_{Cub}/IL(40)**-based actuator. (c) An electronic pincer made with a pair of actuator sheets can hold a block of Styrofoam weighing 150 mg by bending inwards.

5.4 Conclusions.

In conclusion of this chapter, I reported a new ionic LC molecule for the construction of well-defined micellar cubic LC electrolyte with continuous ion pathways. This strategy primarily involves the supramolecular assembly of taper-shaped LC molecules surrounded by **IL**, into stable spherical structures that can persist over a broad temperature range. The phase transition of the original Col_h structure to the Cub_M structure is promoted through the addition of **IL**, which not only affects the structure conformation arrangement but also the mechanical modulus. The cubic structure endowed the combine function of the low tortuosity of ion diffusion route and well-packed of the ordering molecular sphere to build up the bifunctional materials. The resulting Cub_M electrolyte membrane preserved the advantage of mechanically tough and interconnected ion pathways that allow fast and efficient ion diffusion. In the evaluation results, the tri-layer actuator composed of the Cub_M electrolyte with a pair of **PEDOT:PSS** electrodes was able to exhibit remarkable actuation performance under a low driven voltage of 2 V and 0.1 Hz, including a high bending strain (0.63 %), a force generation (2.7 mN), which was hold the better performance than my previous reported LC materials. I further investigated the detailed generation force distribution on the bending actuator, and demonstrated the powerful operation with high force output to carry heavy objects. The design concept based on the construction of periodic LC cubic structure was established a potentials milestone to new energy storage and transduction actuators.

5.5 References.

(1) Bai, H.; Li, S.; Shepherd, R. F. Elastomeric Haptic Devices for Virtual and Augmented Reality. *Adv. Funct. Mater.* **2021**, *31*, 2009364.

(2) Lu, L.; Liu, J.; Hu, Y.; Zhang, Y.; Randriamahazaka, H.; Chen, W. Highly Stable Air Working Bimorph Actuator Based on a Graphene Nanosheet/Carbon Nanotube Hybrid Electrode. *Adv. Mater.* **2012**, *24*, 4317–4321.

(3) Raza, U.; Oh, S.; Tabassian, R.; Mahato, M.; Nguyen, H. V.; Oh, I. K. Micro–Structured Porous Electrolytes for Highly Responsive Ionic Soft Actuators. *Sens. Actuators B* **2022**, *352*, 131006.

(4) Lu, L.; Chen, W. Biocompatible Composite Actuator: A Supramolecular Structure Consisting of the Biopolymer Chitosan, Carbon Nanotubes, and an Ionic Liquid. *Adv. Mater.* **2010**, *22*, 3745–3748.

(5) Cheedarala, R. K.; Jeon, J. H.; Kee, C. D.; Oh, I. K. Bio–Inspired All–Organic Soft Actuator Based on a π–π Stacked 3D Ionic Network Membrane and Ultra–Fast Solution Processing. *Adv. Funct. Mater.* **2014**, *24*, 6005–6015.

(6) Correia, D. M.; Fernandes, L. C.; Pereira, N.; Barbosa, J. C.; Serra, J. P.; Pinto, R. S.; Costa, C. M.; Lanceros–Méndez, S. All Printed Soft Actuators based on Ionic Liquid/Polymer Hybrid Materials. *Appl. Mater. Today* **2021**, *22*, 100928.

(7) Imaizumi, S.; Kokubo, H.; Watanabe, M. Polymer Actuators Using Ion−Gel Electrolytes Prepared by Self−Assembly of ABA−Triblock Copolymers. *Macromolecules* **2012**, *45*, 401−409.

(8) Imaizumi, S.; Kato, Y.; Kokubo, H.; Watanabe, M. Driving Mechanisms of Ionic Polymer Actuators Having Electric Double Layer Capacitor Structures. *J. Phys. Chem. B* **2012**, *116*, 5080−5089.

(9) Song, J.; Cho, B. -K. Non-tortuous ionic transport in robust micellar liquid crystalline phases with cubic symmetry. *Chem. Commun.* **2012**, *48*, 6821–6823.

(10) Matsumoto, T.; Ichikawa, T.; Sakuda, J.; Kato, T.; Ohno, H. Design of Amphiphilic Zwitterions Forming Liquid-Crystalline Phases and Effects of Lithium Salt Addition on Their Phase Behavior. *Bull. Chem. Soc. Jpn.* **2014**, *87*, 792796.

(11) Ichikawa, T.; Yoshio, M.; Hamasaki, A.; Kagimoto, J.; Ohno, H.; Kato, T. 3D Interconnected Ionic Nano-Channels Formed in Polymer Films: Self-Organization and Polymerization of Thermotropic Bicontinuous Cubic Liquid Crystals. *J. Am. Chem. Soc.* **2011**, *133*, 2163–2169.

(12) Montalvo, G.; Valiente, M.; Rodenas, E. Rheological Properties of the L Phase and the Hexagonal, Lamellar, and Cubic Liquid Crystals of the CTAB/Benzyl Alcohol/Water System. *Langmuir* **1996**, *12*, 5202–5208.

(13) Emo, M.; Stébé, M. -J.; Blin, J. -L.; Pasc, A. Metastable micelles and true liquid crystal behaviour of newly designed “cataniomeric” surfactants. *Soft Matter* **2013**, *9*, 2760–2768.

(14) Jayaraman, A.; Mahanthappa, M. K. Counterion-Dependent Access to Low-Symmetry Lyotropic Sphere Packings of Ionic Surfactant Micelles. *Langmuir* **2018**, *34*, 2290–2301.

(15) Zhang, L.; Lin, J.; Lin, S. Self-Assembly Behavior of Amphiphilic Block Copolymer/Nanoparticle Mixture in Dilute Solution Studied by Self-Consistent-Field Theory/Density Functional Theory. *Macromolecules* **2007**, *40*, 5582–5592.

(16) Penfold, N. J. W.; Lovett, J. R.; Verstraete, P.; Smets, J.; Armes, S. P. Stimulus-responsive non-ionic diblock copolymers: protonation of a tertiary amine end-group induces vesicle-to-worm or vesicle-to-sphere transitions. *Polym. Chem.* **2017**, *8*, 272–282.

(17) Lv, F.; An, Z.; Wu, P. What Determines the Formation of Block Copolymer Nanotubes? *Macromolecules* **2020**, *53*, 367–373.

(18) Yoshida, K.; Tanaka, S.; Yamamoto, T.; Tajima, K.; Borsali, R.; Isono, T.; Satoh, T. Chain-End Functionalization with a Saccharide for 10 nm Microphase Separation: “Classical” PS-*b*-PMMA versus PS-*b*-PMMA-Saccharide. *Macromolecules* **2018**, *51*, 8870–8877.

(19) Dai, H.; Yang, X.; Tan, X.; Su, F.; Cheng, X.; Liu, F.; Tschierske, C. Liquid crystalline 2-thienyl-4,6-diamino-1,3,5-triazines exhibiting *Im3m* and *Pm3n* micellar cubic phases in an inverted sequence. *Chem. Commun.* **2013**, *49*, 10617.

(20) Rodrı´guez-Abreu, C.; Garcı´a-Roman, M.; Kunieda, H. Rheology and Dynamics of Micellar Cubic Phases and Related Emulsions. *Langmuir* **2004**, *20*, 5235–5240.

(21) Zhao, J.; Majumdar, B.; Schulz, M. F.; Bates, F. S. Phase Behavior of Pure Diblocks and Binary Diblock Blends of Poly(ethylene)-Poly(ethylethylene). *Macromolecules* **1996**, *29*, 1204–1215.

Chapter 6

General Conclusion and Future Prospects

This dissertation primarily focuses on the innovative design of photocured ionic liquid-crystalline (LC) electrolytes and their emerging application in iEAP actuators. This research has successfully opened up new application fields for ionic liquid crystals. From the point of conventional iEAP actuators, despite various approaches employed to achieve high-performance bending motion, the issues involved the risk of liquid electrolyte leakage, and the durability/reliability in the conventional ionogel electrolytes remain a sensitive and inevitable challenge that cannot be addressed by the appropriate answers.

Discussion. In this dissertation, a certain and positive method was established through functionalized LC amphiphiles. This approach enables the creation of the ordered nano-scale ion channels within a solid LC matrix, in which ion-active channels was composed of the pendant ionic groups from LC molecules, and little ionic liquid (IL). Therefore, the IL-occupied ion-rich pathways led to fast migration for dissociated ions, followed by successfully induces significant deformation for the actuator. Beyond that, the nanostructure with different-dimensional ion channels also has an impact on the actuator performance, although the LC molecular structure and shape, ionophilic/ionophobic fraction, and cross-link density might also influence the actuation bending. If we unilaterally focus on the relationship between the ionic conductivity and the local ion concentrations within LC electrolytes (amount of absorbed IL per imidazolium group (λ)), the result supports the notion that 3D ion pathways mainly dominate the faster ion transport than the IL content, even when the low content of IL is confined within the electrolyte membranes (**Figure 6.1 (a)**). This is due to their advantage of ionic LC structure contributing to the more association site for IL, in which the hydrogen bonding can form between the imidazole groups and dissociated BF_4 anions, leading to the efficient transporting for the others net ion.

Summary. Benefiting from the highly ordered arrangement of nanoscale ion channels, the high-efficiency ion transport that occurred in LC electrolytes make it possible to create a new type of next-generation iEAP actuators with low ionic liquid content and excellent bending strain (**Figure 6.1 (b)**). In summary of the results, the overall conclusion for LC iEAP actuators from each chapter are provided below:

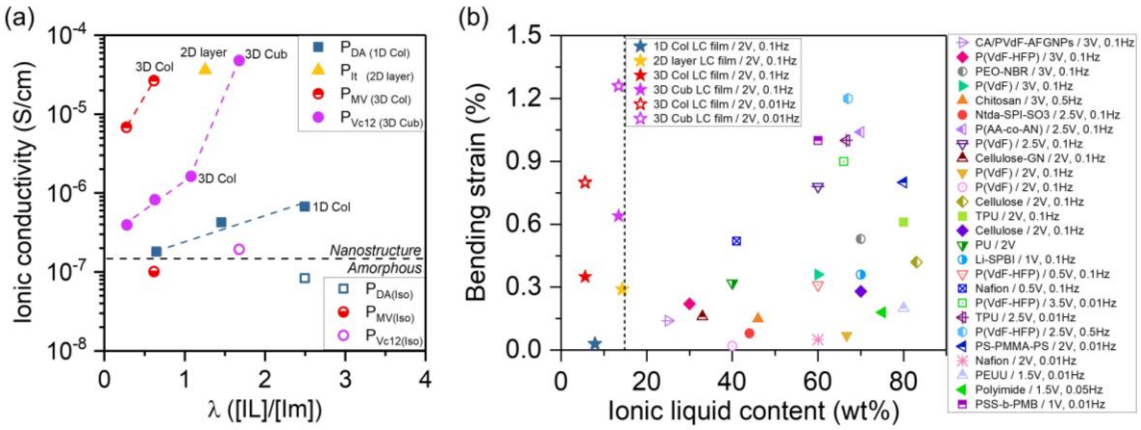

Figure 6.1 (a) Ionic conductivity versus calculated local concentration of ions within nanostructured LC electrolyte membranes. (b) Bending strain versus IL content for the LC actuators and other, previously reported actuators. The dashed line is the mark of 15 wt%.

Firstly, I report for the first time that low-voltage-driven actuators based on photo-crosslinked ionic columnar LC films integrating IL into nanoscale 1D channels. I have unveiled the effect of nanochannels on the actuator performance. The nanostructured actuator exhibits 2 times larger deformation and generated force compared with the corresponding amorphous actuator. This approach has preliminarily established the affirmative concept of using ionic LC electrolytes for iEAP actuators.

Secondly, considering the effective LC structure design for cost-cutting, I have designed a simple itaconate amphiphile through a two-step reaction. This ionic itaconate mixed with IL was able to self-organize into abundant thermotropic LC phases, followed by the ionic layered structure preserved within polymer films by UV irradiation. In the result of this part, I highlighted that the conformation aligned of the layer structure from random to vertical orientation exhibits about 1.75 times enhancement on the bending strain and the blocking force. This study not only paves the way for new possibilities in electromechanical energy conversion, thereby advancing the development of next-generation printable soft robots, but also maintains the biodegradable characteristics of new LC materials. This makes a significant contribution to addressing issues related to new energy, sustainability, and soft electronics in the future.

Thirdly, to further extend the design concept of ion-active pathways, I have reported a new family of taper-shaped ionic LC molecules that were able to form the inverse polar domains of Col_h and micellar cubic (Cub_M) structures through the self-organization with IL. The salient features of the molecular design were especially highlighted in the formation of efficient 3D continuous ion pathways within the LC phases. These newly designed LC electrolyte membranes release several benefits, such as: flexibility, stability, ion transporting, nanostructured, and solvent resistance. Both Col_h and Cub_M LC electrolyte-based actuators exhibit the good actuation under low driven voltage. In addition, Cub_M electrolyte-based actuator possessed better performance prevails over the other LC electrolyte-based actuators. It is due to the high ionic fraction occupying the inverse spherical spaces, promoting the well-pack of spherical cubic filled by IL which simultaneously contributed to the good mechanical modulus and efficient ion transport. The establishment of an inverse ion domain within the electrolytes through the new ionic LC molecule design was successfully employed in iEAP actuators. This innovative molecular design may have so far unmatched development in the combination of functional materials and cutting-edge applications in sensors and actuators.

Future Prospects. Functional ionic LC electrolytes imparted the emerging findings for iEAP actuators through the rational design of ionic LC structures. However, behind these satisfactory results, there still has room for improvement that needs further research. It would touch on the broader molecular design principle and mechanistic elucidation. For example: the systematic study of the IL effect on LC phases, ion migration, and actuation, or deeply understood of the ionic LC electrolyte design based on the cation/anion pendant groups. Based on my current research, I give some comments for the future prospect of "How to further improve the actuation performance and employ to actual application" that people might be interested in. From the actuation results, people might focus on whether fast response ability is possessed in the LC iEAP actuator. To build a fast response actuator based on the current LC electrolytes, it is possible to address by three prospective methods: (1) combined with architected electrodes, (2) creation of intra-molecular hydrogen bonding inside the electrolytes, or (3) enhancing the overall dielectric constant of LC electrolytes. These strategies mainly focus on the weaken molecular interaction between the imidazole groups and ILs and further improving the ions

accumulated on the electrodes. The high performance of LC iEAP actuators with conflicting functions of high-force generation and good deformation holds promise for developing intellectualization electronic haptic sensors in combination with printable, encapsulation technologies as well as the complex neuromuscular electronic system.

Appendix

Synthesis and Identification Methods

7.1 General Procedures.

All ^{1}H–NMR and ^{13}C–NMR spectra were recorded on a JEOL ECZ400S spectrometer at 400 MHz and 100 MHz for solutions in $CDCl_3$, respectively. The chemical shifts (δ) are quoted in ppm using the $CDCl_3$ solvent peak as internal reference (δ = 7.26 for ^{1}H–NMR spectra, and δ = 77.16 for ^{13}C–NMR spectra). Matrix–assisted laser desorption/ionization time–of–flight mass spectrometry (MALDI TOF–MS) measurements were carried out with a Shimadzu AXIMA–CFR Plus. Dithranol was used as a matrix. Fourier–transform infrared spectroscopy (FTIR) spectra were taken with a BRUKER FT–IR ALPHA II spectrometer equipped with a single reflection diamond ATR module. Elemental analysis for C, H and N was carried out by using an ELEMENTAR vario EL cube.

7.2 Synthesis of Ionic Molecule It.

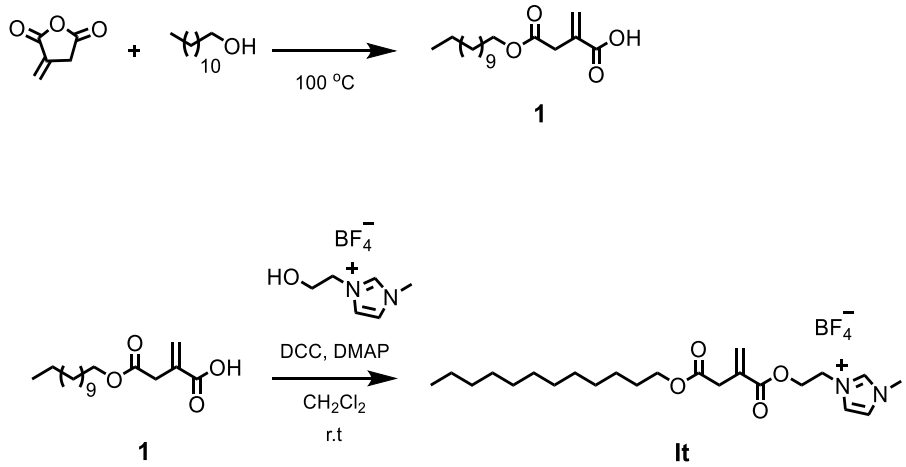

Scheme S1. Synthetic routes of ionic molecule **It**.

Synthesis of 1

Itaconic anhydride (1 g, 8.92 mmol) was mixed with 1–dodecanol (2 mL, 8.92 mmol) in a Schlenk flask with stirring. The mixture solution was kept at 100 °C and traced with a TLC plate. After the reaction completed, the hot hexane was used to wash the reaction mixture and the crude product was precipitated. The crude product was recrystallized from ethanol to give compound **1** as white crystal (Yield: 75%).

^{1}H–NMR (400 MHz, $CDCl_3$, δ = ppm): 0.861–0.895 (m, 3H), 1.25 (m, 18H), 1.58–1.63 (m, 2H), 3.33 (s, 2H), 4.07–4.11 (td, 2H), 5.82 (s, 1H), 6.46 (s, 1H).

Synthesis of It

Compound **1** (1 g, 3.35 mmol), *N*,*N*–dicyclohexylcarbodiimide (DCC; 0.83 g, 4 mmol), 4–dimethylaminopyridine (DMAP; 0.02 g, 0.17 mmol) and 15 mL of DCM were mixed in a Schlenk flask with stirring and purged with argon for 30 minutes in an ice bath. Then, 1–(2–hydroxyethyl)–3–methylimidazolium tetrafluoroborate (0.64 mL, 4 mmol) were added dropwise into the mixture solution by using an addition funnel. The reaction was warmed to room temperature and stirred for 48 hours. The reaction mixture was diluted with DCM and extracted with water three times. The organic phase was collected and dried with $MgSO_4$. After evaporating the solvent, the crude product was purified by column chromatography (eluent: gradient from chloroform : methanol = 100/0 to 90/10 v/v) to give **It** as a white liquid crystal (Yield: 53%).

^{1}H–NMR (400 MHz, $CDCl_3$, δ = ppm): 0.86–0.89 (t, 3H), 1.26 (m, 18H), 1.60–1.65 (m, 2H), 1.85–1.93 (m, 4H), 3.33 (s, 2H), 3.96 (s, 3H), 4.03–4.07 (t, 2H), 4.56 (s, 4H), 5.75 (s, 1H), 6.30 (s, 1H), 7.24 (s, 1H), 7.48 (s, 1H), 8.89 (s, 1H).

^{13}C–NMR (100 MHz, $CDCl_3$, δ = ppm): 14.21, 22.78, 25.97, 28.62, 29.37, 29.45, 29.63, 29.70, 29.74, 29.75, 32.01, 36.42, 37.71, 48.81, 63.07, 65.45, 123.07, 123.72, 129.63, 133.15, 137.11, 165.74, 171.17.

MS (MALDI–TOF): *m/z* calcd. for $C_{23}H_{39}BF_4N_2O_4$, $[M–BF_4]^+$: 407.29; found: 407.03.

Elemental analysis calcd. for $C_{23}H_{39}BF_4N_2O_4$: C, 55.88, H, 7.95, N, 5.67; found: C, 55.99, H, 7.71, N, 5.28.

FT–IR (ATR): ν = 3163, 3118, 2955, 2922, 2853, 1721, 1637, 1576, 1460, 1427, 1370, 1377, 1315, 1388, 1260, 1170, 1142, 1052, 1031, 966, 940, 846, 817, 758, 723, 703, 652, 624, 599, 548, 522, 479 cm^{-1}.

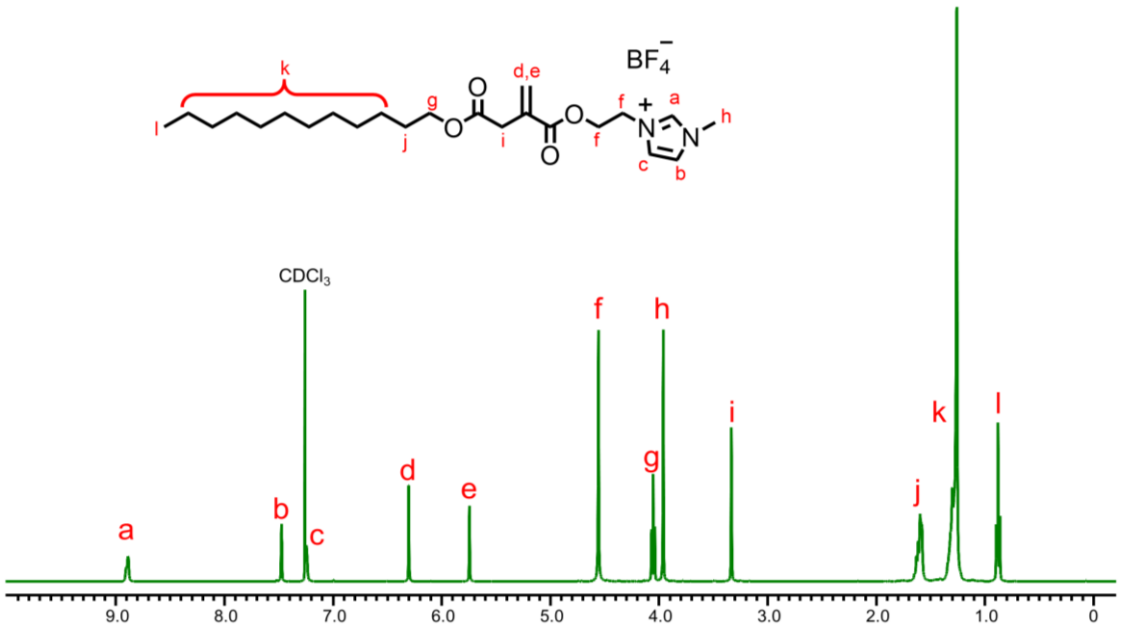

Figure 7.1 ^{1}H–NMR spectra of **It** (400 MHz, $CDCl_3$).

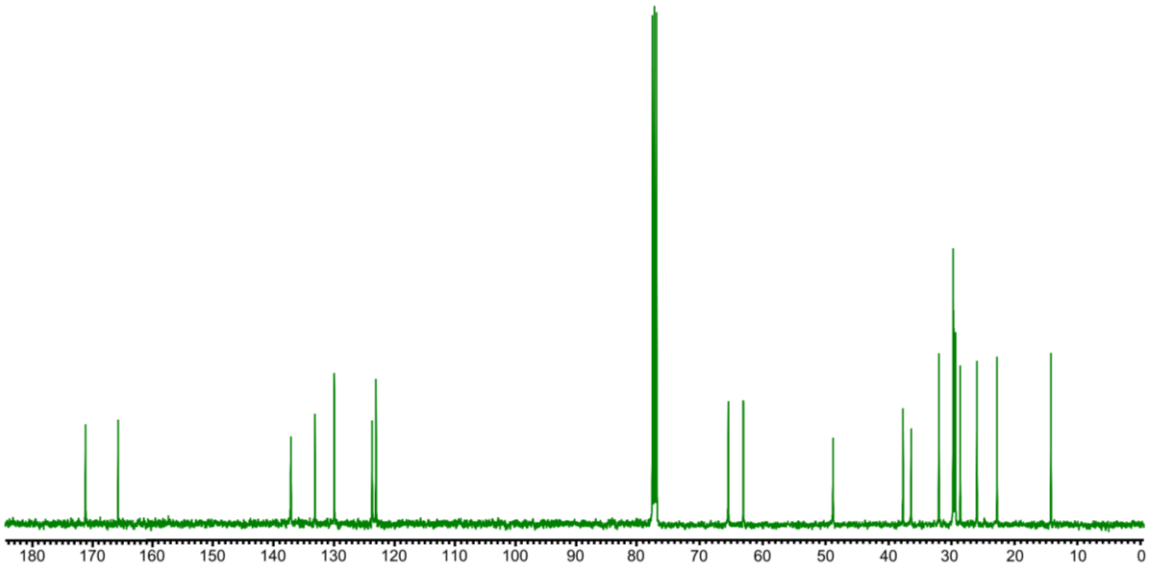

Figure 7.2 ^{13}C–NMR spectra of **It** (100 MHz, $CDCl_3$).

7.3 Synthesis of Ionic Liquid Crystals M–ILC and V–ILC.

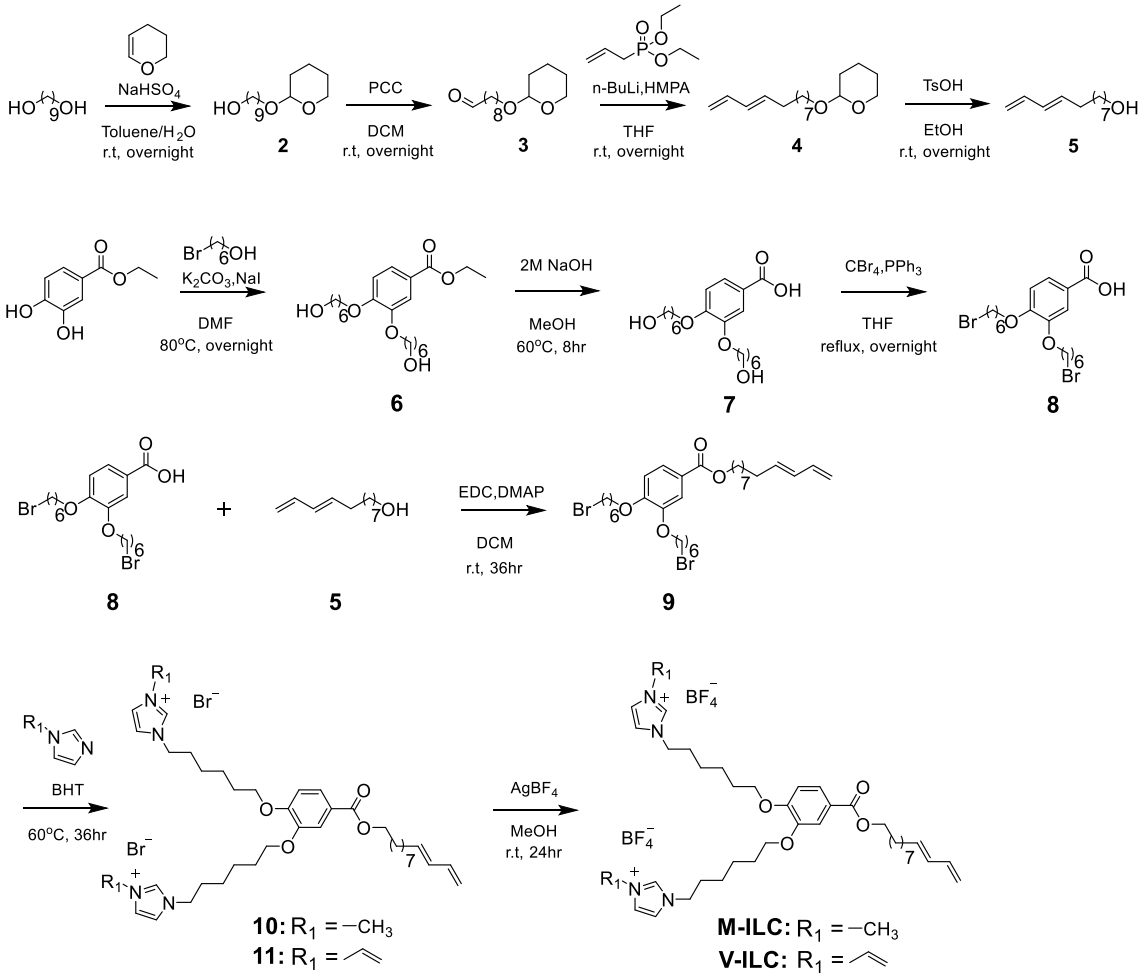

Scheme S2. Synthetic routes of ionic liquid crystal monomers with methyl– and vinyl–imidazole end groups, labeled as **M–ILC** and **V–ILC**.

Synthesis of 2

1,9–Nonanediol (25 g, 156 mmol) and 3,4–dihydro–2*H*–pyran (14 mL, 156 mmol) were dissolved in 380 mL of toluene under vigorous stirring, and a 0.4 M sodium bisulfate aqueous solution was added into the mixture. The reaction was kept at room temperature and traced by a thin–layer chromatography (TLC) plate. After reaction had completed, the mixture solution was separated with a funnel. The organic solution was extracted with a sodium bisulfate solution and water three times. Then, the organic phase was dried with $MgSO_4$ and evaporated under vacuum. The crude product without purification gives transparent liquid that was used for the next step (Yield: 79%).

^{1}H–NMR (400 MHz, $CDCl_3$, δ = ppm): 1.28–1.58 (m, 18H), 1.68 (m, 1H), 1.79 (m, 1H),

3.35 (dt, 1H), 3.47 (m, 1H), 3.59 (t, 2H), 3.70 (dt, 1H), 3.84 (m, 1H), 4.55 (t, 1H).

Synthesis of 3

Compound **2** (30 g, 122 mmol) was dissolved in 200 mL of dichloromethane (DCM) under vigorous stirring, and then pyridinium chlorochromate (26.5 g, 122 mmol) was slowly added into the solution. The black coordination complex was created immediately. The mixture solution was stirred overnight at ambient temperature. After reaction finished, Celite was added and filtered by a thin–layer silica gel to remove black viscous complex. The crude product was purified by column chromatography (eluent: gradient from hexane : ethyl acetate = 90/10 to 70/30 v/v) to afford compound **3** as a transparent liquid (Yield: 55%).

^{1}H–NMR (400 MHz, $CDCl_3$, δ = ppm): 1.24–1.62 (m, 18H), 1.68 (m, 1H), 1.81 (m, 1H), 2.40 (td, 2H), 3.35 (dt, 1H), 3.48 (m, 1H), 3.70 (dt, 1H), 3.84 (m, 1H), 4.55 (t, 1H), 9.74 (s, 1H).

Synthesis of 4 (Horner–Wadsworth–Emmons reaction)

Anhydrous diethyl allyl phosphonate (12.9 mL, 74 mmol) in 100 mL of anhydrous tetrahydrofuran (THF). Then, 1.57 M *n*–BuLi (46.5 mL, 74 mmol) was added dropwise into the mixture at –78ºC cooling acetone bath. After stirring for 30 min, the compound **3** (15 g, 62 mmol) was added dropwise and follow by HMPA solution (19.4 mL, 111 mmol). The reaction was kept at –78 ºC for 2 h and then at room temperature for overnight. Then, the reaction was quenched by saturated ammonium chloride aqueous solution. The organic phase was washed by brine and water three times, and then dried with $MgSO_4$. The crude product was purified by column chromatography (eluent: gradient from hexane : chloroform = 50/50 to 0/100 v/v) to give compound **4** as transparent liquid (Yield: 45%).

^{1}H–NMR (400 MHz, $CDCl_3$, δ = ppm): 1.22–1.61 (m, 16H), 1.70 (m, 1H), 1.81 (m, 1H), 2.05 (m, 2H), 3.37 (dt, 1H), 3.49 (m, 1H), 3.72 (dt, 1H), 3.86 (m, 1H), 4.56 (t, 1H), 4.95 (d, 1H), 5.09 (d, 1H), 5.69 (m, 1H), 6.02 (m, 1H), 6.29 (dt, 1H).

Synthesis of 5

The compound **4** (7.5 g, 74 mmol) and *p*–toluenesulfonic acid monohydrate (TsOH; 1.7 g, 9 mmol) in 60 mL ethanol were stirred overnight at ambient temperature. The reaction was traced with a TLC plate. After reaction completed, the saturated ammonium chloride aqueous was added to quench reaction and washed by ethyl acetate three times. Then, organic phase was dried with $MgSO_4$. The crude product was purified by column chromatography (eluent: gradient from hexane : ethyl acetate = 90/10 to 70/30 v/v) to give compound **5** as a transparent liquid (Yield: 80%).

^{1}H–NMR (400 MHz, $CDCl_3$, δ = ppm): 1.33–1.59 (m, 12H), 2.08 (m, 2H), 3.63 (t, 2H), 4.96 (d, 1H), 5.10 (d, 1H), 5.70 (m, 1H), 6.04 (m, 1H), 6.30 (dt, 1H).

Synthesis of 6

Ethyl 3,4–dihydroxybenzoate (3.80 g, 20 mmol), K_2CO_3 (6.92 g, 50 mmol) and NaI (0.59 g, 4 mmol) were dissolved in 30.7 mL of dimethylformamide (DMF) under argon in a Schlenk flask, and then 6–bromo–1–hexanol (5.46 mL, 41 mmol) was added into the mixture solution under vigorous stirring. The reaction solution was then kept at 80 °C overnight. The reaction was stopped by quenching to room temperature, and the crude material was dissolved in chloroform and extracted with a large amount of water. The organic phase was dried with $MgSO_4$ to remove residual water and crude product was obtained by evaporating chloroform. The crude product was purified by column chromatography (eluent: gradient from hexane : ethyl acetate = 100/0 to 20/80 v/v) to obtain white solid (Yield: 82%).

^{1}H–NMR (400 MHz, $CDCl_3$, δ = ppm): 1.36 (t, 3H), 1.41–1.54 (m, 8H), 1.60 (m, 4H), 1.83 (m, 4H), 3.64 (t, 4H), 4.03 (t, 4H), 4.33 (q, 2H), 6.83 (d, 1H), 7.52 (d, 1H), 7.61 (dd, 1H).

Synthesis of 7

Compound **6** (6.6 g, 17 mmol) was dissolved in 2 M NaOH/MeOH solution in a Schlenk flask. The reaction was kept at 60^{o}C for 8 hours and traced with a TLC plate. After reaction was completed and cooled down to room temperature, MeOH was removed by evaporation. The 1 M HCl solution was added into crude and the product was precipitated. The obtained white solid was collected by vacuum filtration and dried at 70^{o}C under vacuum overnight (Yield: 90%).

^{1}H–NMR (400 MHz, DMSO–*d*, δ = ppm): 1.33–1.49 (m, 12H), 1.70 (m, 4H), 3.31–3.39 (m, 4H), 3.98 (dt, 4H), 7.03 (d, 1H), 7.41 (d, 1H), 7.53 (dd, 1H).

Synthesis of 8 (Appel reaction)

Compound **7** (5.55 g, 15 mmol) and triphenylphosphine (PPh_3; 11.9 g, 45 mmol) were dissolved in 190 mL of THF at 70 ºC, and then carbon tetrabromide (CBr_4; 13.5 g, 40 mmol) was added into the mixture solution under vigorous stirring. The reaction solution was refluxed overnight. The reaction was stopped by quenching to room temperature, and the residue salt was filtrated. Then, THF was removed by evaporation. The crude product was dissolved in chloroform and extracted with water three times. The organic phase was dried with $MgSO_4$ to remove residual water, and the crude product was obtained by evaporating chloroform. The crude product was purified by column chromatography (eluent: gradient from hexane : ethyl acetate = 100/0 to 10/90 v/v) to obtain a white solid (Yield: 68%).

^{1}H–NMR (400 MHz, $CDCl_3$, δ = ppm): 1.53 (m, 8H), 1.89 (m, 8H), 3.42 (t, 4H), 4.07 (q, 4H), 6.90 (d, 1H), 7.58 (d, 1H), 7.73 (dd, 1H).

^{13}C–NMR (100 MHz, $CDCl_3$, δ = ppm): 25.10, 25.14, 27.76, 27.81, 28.76, 28.86, 32.55, 32.61, 33.64, 33.67, 68.62, 68.85, 111.75, 114.37, 121.40, 124.51, 148.29, 153.72, 172.06.

Elemental analysis calculated for $C_{19}H_{28}Br_2O_4$: C, 47.52, H, 5.88; found: C, 47.80, H, 5.59.

Synthesis of 9

The compound **8** (1 g, 2 mmol), 1–(3–dimethylaminopropyl)–3–ethylcarbodiimide hydrochloride (EDC; 1.2 g, 6 mmol), 4–dimethylaminopyridine (DMAP; 0.076 g, 0.6 mmol) and 15 mL of DCM were mixed in a Schlenk flask with stirring and purged with argon for 1 hour in an ice bath. Then, compound **5** (0.38 g, 2 mmol) and DCM were added dropwise into the mixture solution by using an addition funnel. The reaction was stirred for 36 hours. The reaction mixture was diluted with DCM and extracted with water three times. The organic phase was collected and dried with $MgSO_4$. After evaporating the solvent, the crude product was purified by column chromatography (eluent: gradient from hexane : ethyl acetate = 100/0 to 70/30 v/v) to give compound **9** as a white solid (Yield: 58%).

^{1}H–NMR (400 MHz, $CDCl_3$, δ = ppm): 1.31–1.43 (m, 10H), 1.52 (m, 8H), 1.74 (t, 2H),

1.82–1.91 (m, 8H), 2.04–2.09 (q, 2H), 3.42 (t, 4H), 4.04 (td, 4H), 4.27 (t, 2H), 4.93–5.09 (dd, 2H), 5.69 (m, 1H), 6.04 (dd, 1H), 6.30 (dt, 1H), 6.86 (d, 1H), 7.52 (d, 1H), 7.62 (dd, 1H).

^{13}C–NMR (100 MHz, $CDCl_3$, δ = ppm): 25.09, 25.13, 25.90, 27.74, 27.78, 28.65, 28.79, 28.88, 28.98, 29.02, 29.09, 29.24, 32.39, 32.55, 32.59, 33.58, 33.60, 64.77, 68.57, 68.83, 111.80, 114.16, 114.49, 122.80, 123.39, 130.79, 135.34, 137.21, 148.25, 152.84, 166.35.

Elemental analysis calculated for $C_{31}H_{48}Br_2O_4$: C, 57.77, H, 7.51; found: C, 57.85, H, 7.00.

Synthesis of 10

The compound **9** (0.77 g, 1.2 mmol), 2,6–*di*–*tert*–butyl–4–methoxyphenol (BHT; 0.026 g, 0.12 mmol), and 1–methylimidazole (1.5 mL, 19 mmol) were mixed in a Schlenk flask with stirring under argon atmosphere. The mixture solution was kept at 60^{o}C and traced with a TLC plate. After the reaction completed, diethyl ether was added into the reaction mixture to turn it into a viscous pale–orange solid, then washed three times by sonication. The crude product was used for the next step (Yield: 99%).

Synthesis of M–ILC

Compound **10** (0.96 g, 1.2 mmol) was dissolved in 4.8 mL of MeOH in a light–resistant Schlenk flask. Then, silver tetrafluoroborate (0.48 g, 2.49 mmol) dissolved in MeOH was added dropwise into the reaction under vigorous stirring. A green salt was created immediately. After removing the salt by filtration and evaporating the solvent, the crude product was purified by column chromatography (eluent: gradient from chloroform : methanol = 100/0 to 90/10 v/v) and recycling preparative gel permeation chromatography (GPC) to give **M–ILC** as a white liquid crystal (Yield: 70%).

^{1}H–NMR (400 MHz, $CDCl_3$, δ = ppm): 1.31–1.45 (m, 14H), 1.51–1.61 (m, 4H), 1.70–1.84 (m, 6H), 1.85–1.93 (m, 4H), 2.04–2.09 (q, 2H), 3.92 (s, 6H), 4.01 (q, 4H), 4.18 (t, 4H), 4.26 (t, 2H), 4.93–5.10 (dd, 2H), 5.6 (m, 1H), 6.03 (dd, 1H), 6.29 (dt, 1H), 6.86 (d, 1H), 7.28–7.32 (m, 4H), 7.51 (d, 1H), 7.61 (dd, 1H), 8.74 (s, 2H).

^{13}C–NMR (100 MHz, $CDCl_3$, δ = ppm): 25.29, 25.35, 25.67, 25.70, 25.87, 28.64, 28.38, 28.80, 29.00, 29.02, 29.10, 29.24, 29.74, 29.76, 30.40, 35.96, 49.63, 64.86, 68.57, 68.92, 111.99, 114.33, 114.50, 122.18, 122.21, 122.79, 123.60, 130.78, 135.39, 136.03, 137.23, 148.16, 152.91, 166.36.

MS (MALDI–TOF): *m/z* calcd. for $C_{39}H_{60}B_2F_8N_4O_4$, $[M–BF_4]^+$: 735.46; found: 735.16.
Elemental analysis calculated for $C_{39}H_{60}B_2F_8N_4O_4$: C, 56.95, H, 7.35, N, 6.81; found: C, 57.02, H, 7.15, N, 6.63.
FT–IR (ATR): ν = 3161, 3122, 2926, 2857, 1709, 1649, 1598, 1574, 1541, 1511, 1466, 1429, 1388, 1339, 1268, 1211, 1170, 1050, 1017, 895, 870, 844, 762, 697, 648, 624, 520 cm^{-1}.

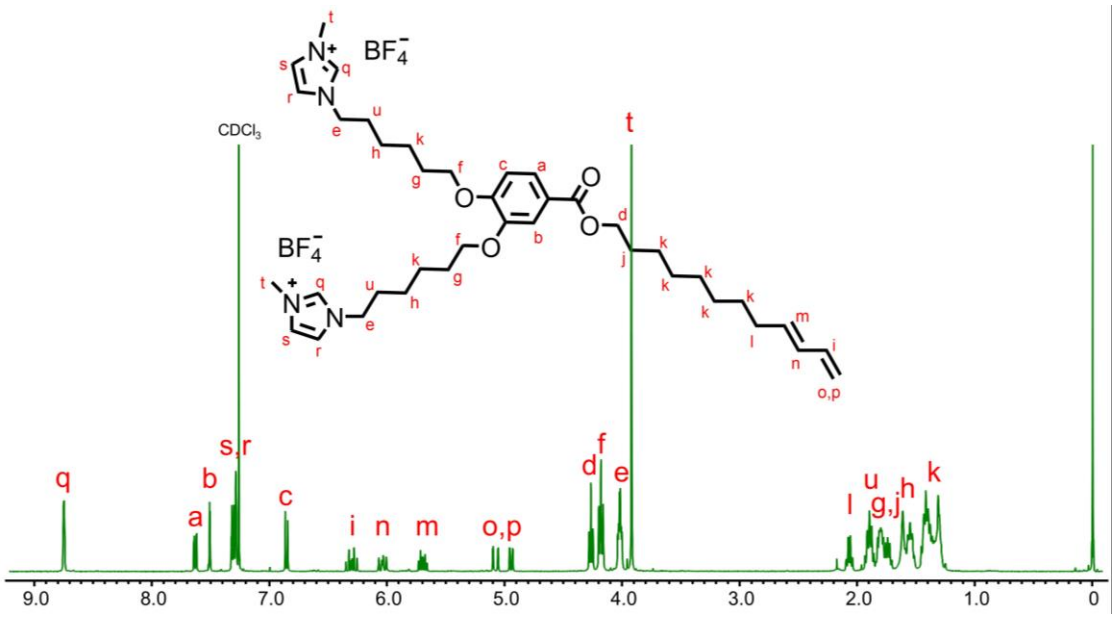

Figure 7.3 ^{1}H–NMR spectra of **M–ILC** (400 MHz, $CDCl_3$).

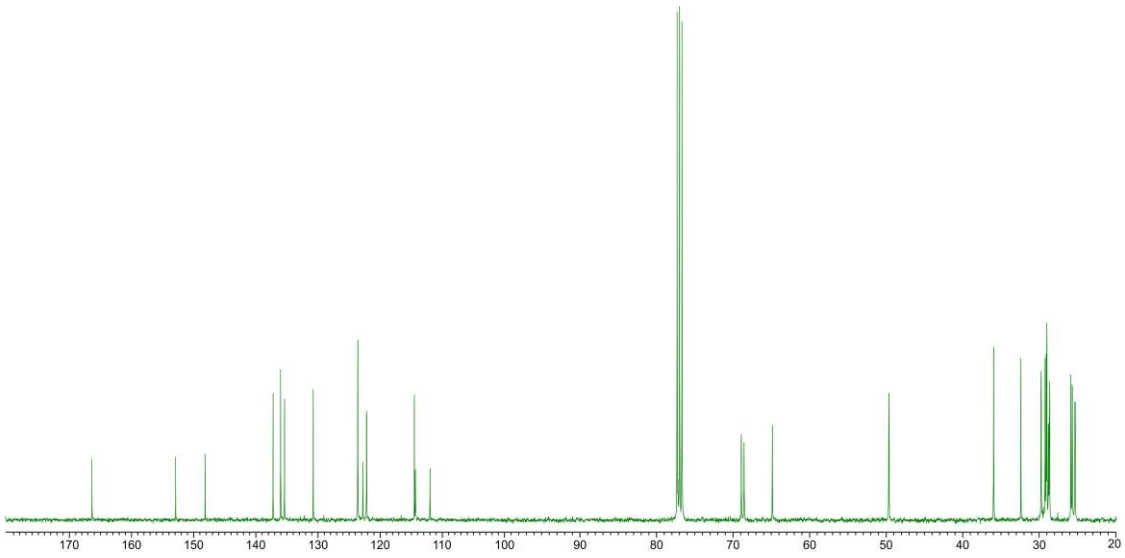

Figure 7.4 ^{13}C–NMR spectra of **M–ILC** (100 MHz, $CDCl_3$).

Synthesis of 11

Compound **9** (0.4 g, 0.6 mmol), 2,6–*di*–*tert*–butyl–4–methoxyphenol (BHT; 0.014 g, 0.06 mmol) and 1–vinylimidazole (1.1 mL, 12 mmol) were mixed in a Schlenk flask with stirring under argon atmosphere. The mixture solution was kept at 60 ^{o}C and trace with a TLC plate. After the reaction completed, diethyl ether was added into the reaction mixture to yield a viscous white solid that was then washed three times by sonication. The crude product was used for the next step (Yield: 97%).

Synthesis of V–ILC

Compound **11** (0.52 g, 0.6 mmol) was dissolved in 12 mL of MeOH in a light–resistant Schlenk flask. Then, silver tetrafluoroborate (0.24 g, 1.24 mmol) dissolved in MeOH was added dropwise into the reaction under vigorous stirring. A green salt was created immediately. After removing the salt by filtration and evaporating the solvent, the crude product was purified by column chromatography (eluent: gradient from chloroform : methanol = 100/0 to 90/10 v/v) and recycling preparative GPC to give **V–ILC** as a white liquid crystal (Yield: 70%).

^{1}H–NMR (400 MHz, $CDCl_3$, δ = ppm): 1.31–1.48 (m, 14H), 1.59 (m, 4H), 1.71–1.85 (m, 6H), 1.90–1.97 (m, 4H), 2.04–2.09 (q, 2H), 4.03 (m, 4H), 4.26 (t, 6H), 4.93–5.10 (dd, 2H), 5.37–5.39 (dt, 2H), 5.66–5.79 (m, 3H), 6.00–6.07 (dd, 1H), 6.25–6.35 (dt, 1H), 6.86 (d, 1H), 7.12 (q, 2H), 7.45 (d, 2H), 7.51 (d, 1H), 7.56 (s, 2H), 7.64 (dd, 1H), 9.10 (s, 2H).

^{13}C–NMR (100 MHz, $CDCl_3$, δ = ppm):25.51, 25.85, 26.05, 28.81, 29.17, 29.41, 29.83, 32.58, 50.25, 65.04, 68.73, 69.09, 109.64, 112.15, 114.50, 114.69, 119.55, 122.95, 123.31, 123.77, 128.28, 130.94, 134.36, 135.58, 137.41, 148.32, 153.07, 166.56.

MS (MALDI–TOF): *m/z* calcd. for $C_{41}H_{60}B_2F_8N_4O_4$, $[M–BF_4]^+$: 759.46; found: 759.04.

Elemental analysis calculated for $C_{41}H_{60}B_2F_8N_4O_4$: C, 58.17, H, 7.14, N, 6.62; found: C, 58.34, H, 7.03, N, 6.59.

FT–IR (ATR): ν = 3161, 3108, 3014, 2924, 2853, 1704, 1655, 1594, 1576, 1554, 1511, 1466, 1429, 1386, 1339, 1288, 1266, 1217, 1180, 1138, 1113, 1058, 1031, 1015, 956, 915, 876, 842, 762, 728, 683, 650, 630, 597, 520 cm^{-1}.

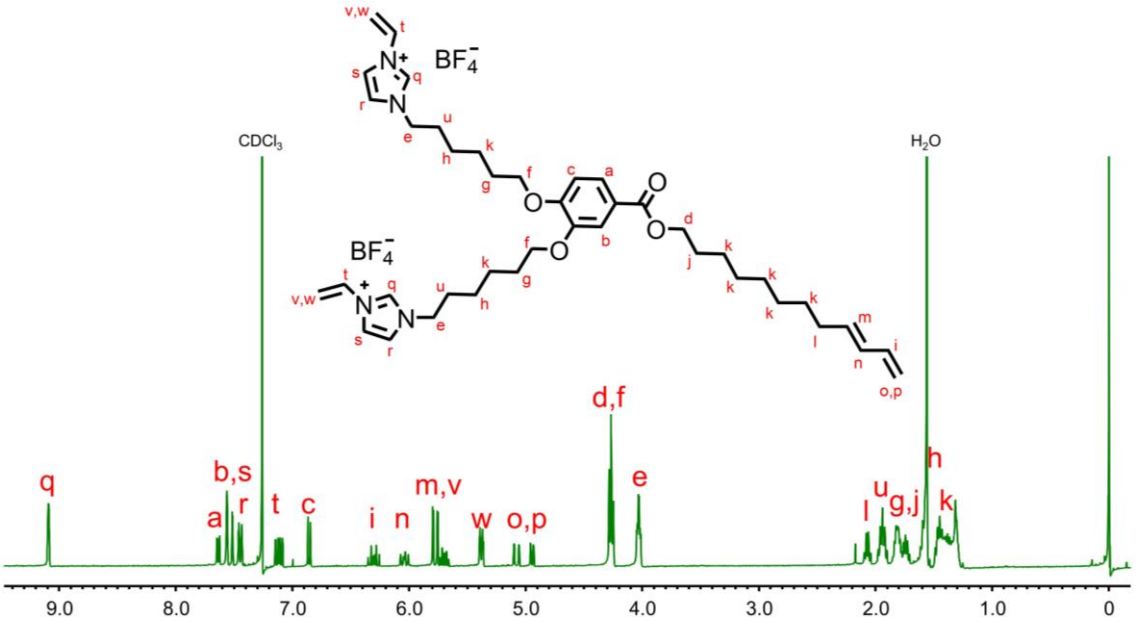

Figure 7.5 ^{1}H–NMR spectra of **V–ILC** (400 MHz, $CDCl_3$).

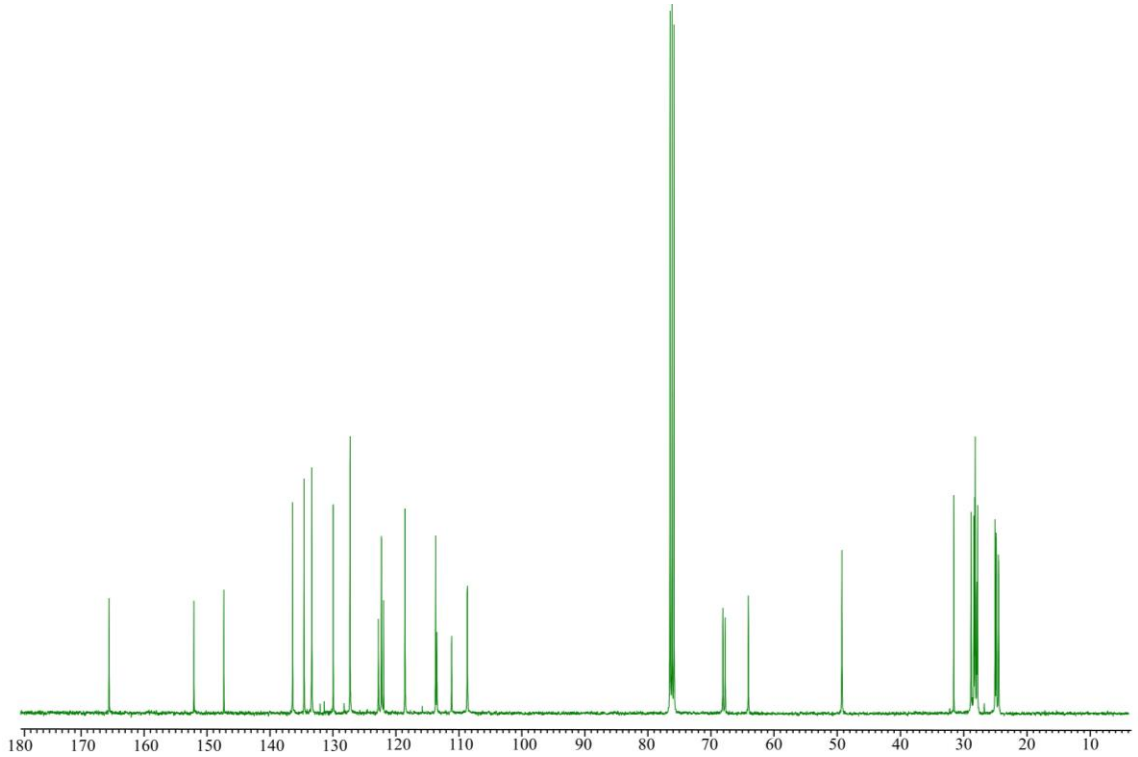

Figure 7.6 ^{13}C–NMR spectra of **V–ILC** (100 MHz, $CDCl_3$).

7.4 Synthesis of Ionic Liquid Crystal Vc12.

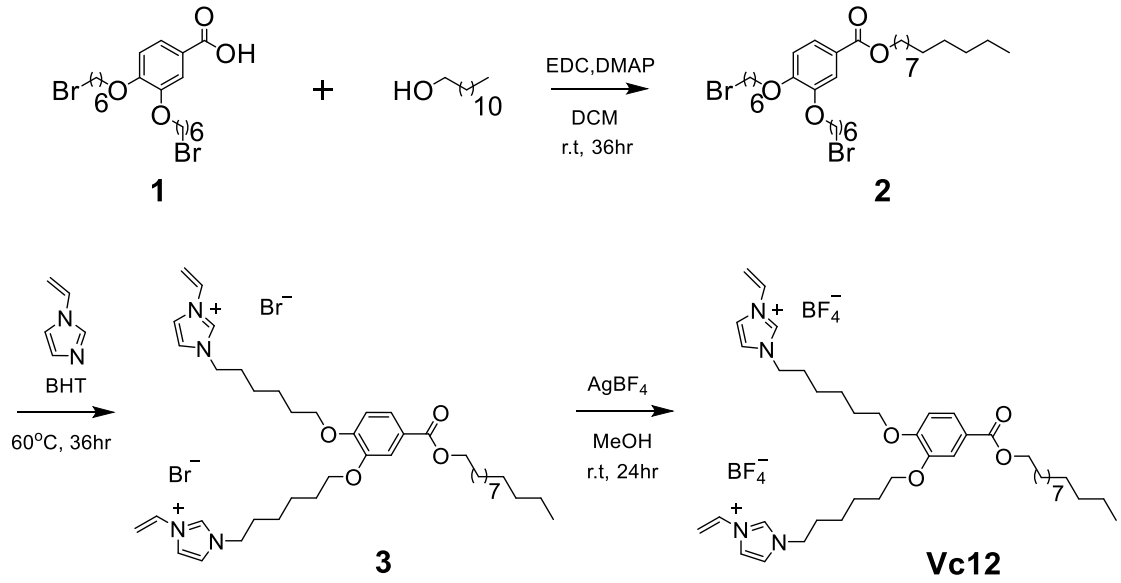

Scheme S3. Synthetic routes of ionic liquid crystal monomer **Vc12**.

Synthesis of 1

The synthesis procedure was same as described in section 7.3.

Synthesis of 2

Compound **1** (0.8 g, 1.7 mmol), 1–(3–dimethylaminopropyl)–3–ethylcarbodiimide (EDC; 1.4 g, 7.3 mmol), 4–dimethylaminopyridine (DMAP; 0.041 g, 0.33 mmol) and 40 mL of DCM were mixed in a Schlenk flask with stirring and purged with argon for an hour in an ice bath. Then, 1–dodecanol (0.31 g, 1.7 mmol) with an amount of DCM was added dropwise into mixture solution by using an addition funnel. The reaction was allowed to warm to room temperature and stirred for 36 hours. The reaction mixture was diluted with DCM and extracted with water three times. The organic phase was collected and dried with $MgSO_4$. The crude product was purified by column chromatography (eluent: gradient from hexane : ethyl acetate = 100/0 to 70/30 v/v) to give compound **2** as white solid (Yield: 52%).

^{1}H-NMR (400 MHz, $CDCl_3$, δ = ppm): 0.87 (t, 3H), 1.25 (m, 16H), 1.42 (t, 2H), 1.52 (m, 8H), 1.74 (m, 2H), 1.84–1.91 (m, 8H), 3.40 (t, 4H), 4.03 (t, 4H), 4.26 (t, 2H), 6.84 (d, 1H), 7.52 (d, 1H), 7.62 (dd, 1H).

^{13}C-NMR (100 MHz, $CDCl_3$, δ = ppm): 14.19, 22.75, 25.28, 25.32, 26.13, 27.93, 27.98,

28.85, 28.98, 29.07, 29.37, 29.42, 29.62, 29.66, 29.71, 31.98, 32.78, 33.75, 65.00, 68.76, 69.02, 111.99, 114.37, 123.03, 123.58, 148.45, 153.02, 166.55.

Synthesis of 3

Compound **2** (0.5 g, 0.8 mmol), 2,6–*di*–*tert*–butyl–4–methoxyphenol (BHT; 0.085 g, 0.4 mmol) and 1–vinylimidazole (1.4 mL, 15.4 mmol) were mixed in a Schlenk flask with stirring under argon condition. The mixture solution was kept at 60oC and traced with a TLC plate. After the reaction completed, diethyl ether was added into the reaction mixture to turn it into a viscous pale–orange solid, then washed three times by sonication. The crude product was used for the next step (Yield: 99%).

Synthesis of Vc12

Compound **3** (0.6 g, 0.7 mmol) was dissolved in 2.5 mL of MeOH in a light–resistant Schlenk flask. Then, silver tetrafluoridoborate (0.28 g, 1.4 mmol) dissolved in MeOH was added dropwise into the reaction under vigorous stirred. A green salt (AgBr) was created immediately. After removing the salt by filtration and evaporating the solvent, the crude product was purified by column chromatography (eluent: gradient from chloroform : methanol = 100/0 to 90/10 v/v) and recycling preparative gel permeation chromatography (GPC) to give **Vc12** as a white liquid crystal (Yield: 77%).

^{1}H–NMR (400 MHz, $CDCl_3$, δ = ppm): 0.87 (t, 3H), 1.25 (m, 16H), 1.44 (m, 6H), 1.54 (m, 4H), 1.74–1.81 (m, 6H), 1.93 (m, 4H), 4.02 (td, 4H), 4.26 (td, 6H), 5.37 (dt, 2H), 5.76 (dd, 2H), 6.84 (d, 1H), 7.1 (m, 1H), 7.45 (dt, 2H), 7.51 (d, 1H), 7.58 (s, 1H), 7.62 (dd, 1H), 9.06 (s, 2H).

^{13}C–NMR (100 MHz, $CDCl_3$, δ = ppm): 13.96, 22.51, 25.25, 25.30, 25.68, 25.84, 28.60, 28.64, 28.75, 29.14, 29.16, 29.38, 29.43, 29.46, 29.48, 29.67, 31.73, 50.09, 64.84, 68.51, 68.86, 109.48, 109.50, 111.91, 114.25, 119.42, 122.71, 123.14, 123.18, 123.53, 128.10, 134.22, 148.08, 152.82, 166.32.

MS (MALDI–TOF): *m/z* calcd. for $C_{41}H_{64}B_2F_8N_4O_4$, $[M–BF_4]^+$: 763.49; found: 763.05.

Elemental analysis calcd. for $C_{41}H_{64}B_2F_8N_4O_4$: C, 57.89, H, 7.58, N, 6.59; found: C, 57.91, H, 7.16, N, 6.41.

FT–IR (ATR): ν = 3154, 3110, 2922, 2853, 1709, 1653, 1598, 1574, 1554, 1511, 1466, 1429, 1386, 1374, 1339, 1268, 1211, 1176, 1052, 1033, 958, 919, 846, 817, 762, 728, 648, 624, 599, 520 cm^{-1}.

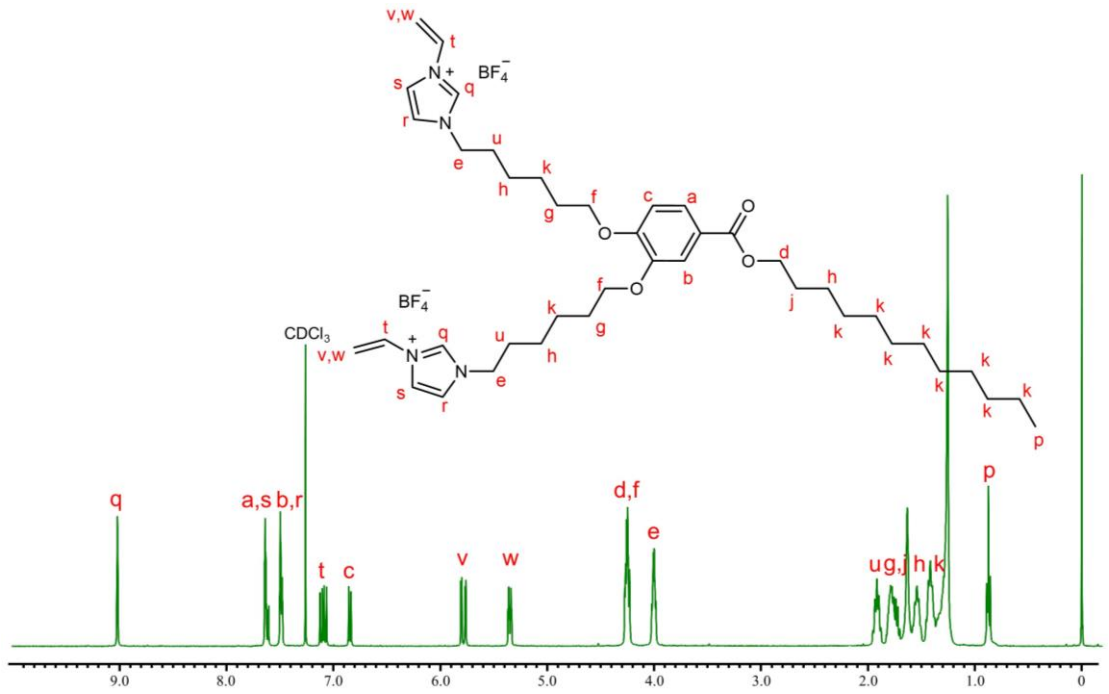

Figure 7.7 ^{1}H–NMR spectra of **Vc12** (400 MHz, $CDCl_3$).

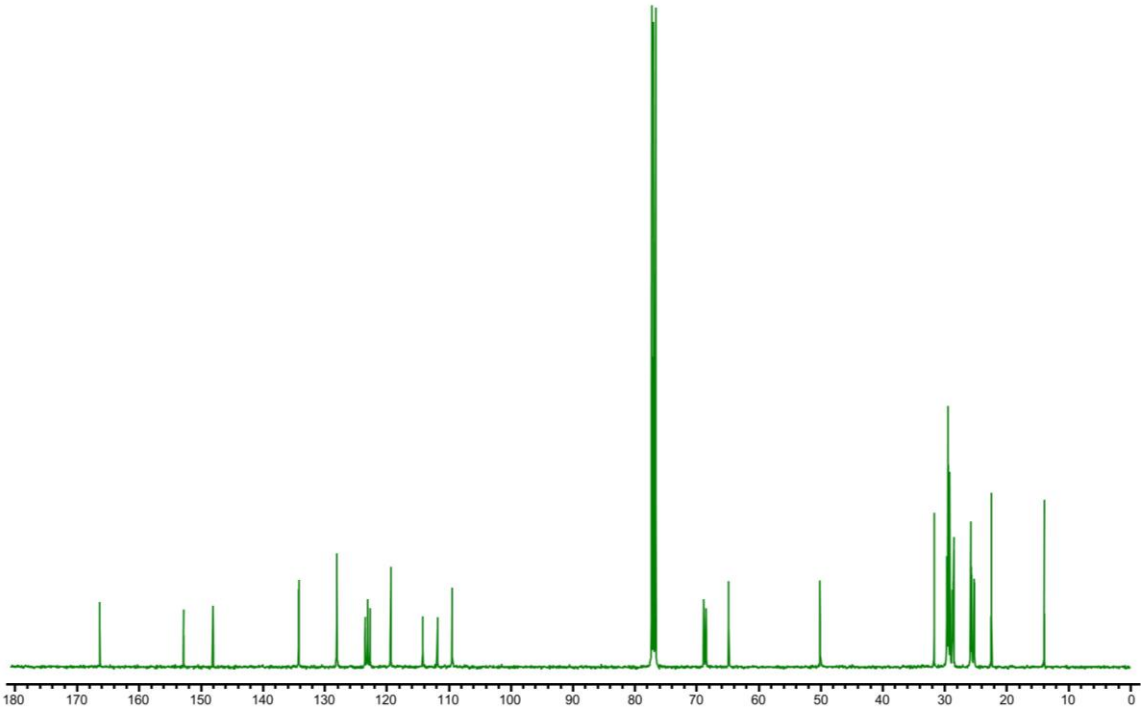

Figure 7.8 ^{13}C–NMR spectra of **Vc12** (100 MHz, $CDCl_3$).

List of Publications

Original Papers:

(1) Che-Hao Wu, Wenjing Meng, and Masafumi Yoshio "Low-Voltage-Driven Actuators Using Photo-Cross-Linked Ionic Columnar Liquid-Crystalline Polymer Films." *ACS Materials Lett.* **2022**, *4*, 153–158. (*Selected as the front cover.*)

(2) Che-Hao Wu, Wenjing Meng, Konstantin Iakoubovskii, and Masafumi Yoshio "Photocured Liquid-Crystalline Polymer Electrolytes with 3D Ion Transport Pathways for Electromechanical Actuators." *ACS Appl. Mater. Interfaces* **2023**, *15*, 4495–4504.

(3) Che-Hao Wu and Masafumi Yoshio " Nanostructured Liquid-Crystalline Polymer Films for Ionic Actuators: Self-Assembly of Photopolymerizable Ionic Itaconate with an Ionic Liquid" *J. Mater. Chem. C* **2023**, *11*, 10154–10162. (*Selected as the front cover.*)

Conferences:

(1) Che-Hao Wu, Masafumi Yoshio "Development of Ionically-Active Columnar Liquid-Crystalline Polymer Film Actuators." 70st Symposium on Macromolecules, Online meeting. (Poster)

(2) Che-Hao Wu, Masafumi Yoshio "Development of Ionically-Active Columnar Liquid-Crystalline Polymer Film Actuators." 2021 NIMS Student Joint Seminar, Tsukuba, Ibaraki.

(3) Che-Hao Wu, Masafumi Yoshio "Development of Ionic Liquid–Crystalline Polymer Membrane Actuators." 71st SPSJ Annual Meeting, Online meeting. (Oral)

(4) Masafumi Yoshio, Che-Hao Wu, Siyo Cao, Chengyang Liu "Electroactive Soft Actuators Based on Nanosegregated Liquid-Crystalline Electrolytes." 71st Symposium on Macromolecules, Sapporo, Hokkaido.

(5) Che-Hao Wu, Masafumi Yoshio "Development of Nanostructured Ionic Liquid–Crystalline Polymer Electrolytes for Electromechanical Actuators." 2022 NIMS Student Joint Seminar, Tsukuba, Ibaraki. (*Excellent Presentation Award.*).

(6) Che-Hao Wu, Masafumi Yoshio "Mechanically Tough Micellar Cubic Liquid-Crystalline Polymer Electrolytes for Electromechanical Actuators." 72nd SPSJ Annual Meeting, Takasaki, Gunma. (Oral)

Acknowledgement

To begin with, I want to convey my heartfelt acknowledgment to the *National Institute for Materials Science (NIMS)* for supporting me as a NIMS Graduate Research Assistantship during my career of doctoral study. I could not be more thankful for the education and support that it has offered both for personal and professional growth.

First and foremost, I would like to express my profound gratitude to my supervisor, *Professor Dr. Masafumi YOSHIO*, for providing me with the opportunity to join this laboratory. Over the past three years, it has been a tremendous honor to be a part of this new group and to grow under his guidance. I am also deeply appreciative of his invaluable advice, unwavering support, and patient assistance throughout every stage of the research project. His extensive knowledge and experience have facilitated my learning in both academic research and daily life. With access to abundant research resources in his laboratory, I have been able to achieve fruitful research results during my Ph.D. Furthermore, I wish to extend my gratitude to the other members of my thesis committee: *Prof. Masaya SAWAMURA*, *Prof. Shin MUKAI*, *Prof. Takuya MASUDA* and *Prof. Naoto SHIRAHATA*, for their insightful comments and suggestions for this dissertation, as well as their support and endorsement of my research results.

My sincere thanks also go to *Dr. Junko AIMI* and my prior professor *Dr. Chih-Feng HUANG* for their kind assistance in not only research activity but also daily life. Especially the great help in my original application for this doctoral program, along with the warm care and support during my research period. I wouldn't have been able to embark on this Ph.D. journey without their support. I would also appreciate *Dr. Wenjing MENG* for her unwavering discussion and help in professional organic chemistry and synthesis. Special thanks to her for sharing her life experiences and perspectives, which enabled me to learn how to maintain an optimistic attitude in the face of setbacks.

I gratefully acknowledge *Dr. Konstantin IAKOUBOVSKII* for his kindly helping on TEM measurement and data analysis. I thank my fellow lab-mates *Dr. Siyu CAO*, *Mr. Chengyang LIU*, and *Mr. Shunichi SUWA* for their discussions and assistance in the experiments. It has been a pleasure to engage in communication about various professional knowledge, experimental techniques, and daily life with you, so that I can

gain invaluable research and life experiences. I would also like to thank the students from TAKEUCHI group, *Dr. Minghan TAN*, *Mr. Xinhao ZHONG*, and *Mr. Zhehui JIN* for their support in daily life. Their kind assistance and solicitude have made my studies and life in Japan an unforgettable experience. Without their tremendous encouragement in the past few years, it would be impossible to complete my study.

Last but not least, I gratefully appreciate my parents and family for their support in letting me go on this great adventure. Despite facing some challenges in life, developing the ability to approach them with a positive mindset is significant growth for me. With everything I have learned from here, I will forge ahead into the next period of life.

Che-Hao WU
writing there in front of my computer, NIMS, June 2023